The Growth by Laser Ablation and Electronic Properties of Thin Cuprate Films: $Bi_2Sr_{2-x}La_xCuO_6$ and $La_{2-x}Sr_xCuO_4$

THÈSE N^O 4120 (2008)

PRÉSENTÉE LE 4 JUILLET 2008
À LA FACULTE SCIENCES DE BASE
LABORATOIRE DE PHYSIQUE DES RAYONS X
PROGRAMME DOCTORAL EN PHYSIQUE

ÉCOLE POLYTECHNIQUE FÉDÉRALE DE LAUSANNE

POUR L'OBTENTION DU GRADE DE DOCTEUR ÈS SCIENCES

PAR

Claudia CANCELLIERI

laurea in fisica della materia, Università degli studi di Milano, Italie
et de nationalité italienne

acceptée sur proposition du jury:

Prof. R. Schaller, président du jury
Prof. D. Pavuna, Dr D. Ariosa Dupont, directeurs de thèse
Prof. C. Bernhard, rapporteur
Prof. A. Gauzzi, rapporteur
Prof. J. Mésot, rapporteur

EPFL

ÉCOLE POLYTECHNIQUE
FÉDÉRALE DE LAUSANNE

Lausanne, EPFL
2008

Contents

III

List of Figures

IV

V

VI

VII

VIII

Abstract

In my thesis work I have concentrated on the growth and the in-depth analysis of high temperature superconducting thin films with the central aim to elucidate their electronic properties, predominantly by in-situ angle resolved photoemission spectroscopy (ARPES). I have used two somewhat complementary approaches and two laser ablation set-ups. The first one, developed previously in Wisconsin, was used mainly for studies of strained $La_{2-x}Sr_xCuO_4$ (LSCO) with a transfer to the Scienta analyzer via an appropriate suitcase. The second one, at the EPFL, where I have built a new pulsed laser deposition (PLD) system, was used to optimize the growth of $Bi_2Sr_{2-x}La_xCuO_4$ (Bi-2201) and study in-situ ARPES.

In-situ ARPES is the most direct tool to probe the electronic structure. We performed it at the Synchrotron Radiation Center (SRC, University of Wisconsin), where we used the aforementioned experimental set-up consisting in a dedicated PLD system coupled with the SCIENTA beamline. The sample transfer procedure assures that the surface quality is preserved on the way to the SCIENTA analyzer. There we studied in detail the effect of strain in LSCO thin films. In a previous work the in-plane compressive strain was studied and the main result was that the Fermi surface (FS) topology changed from hole-like to electron-like. The tensile strained films showed completely different results. ARPES analysis show evidence for a 3-dimensional (3D) electronic dispersion relation in contrast to the strictly 2-dimensional (2D) dispersion observed in all other studied LSCO films. In this thesis this result has been confirmed mapping the FS at different photon energies. We found that the strain related to the thickness of the films, is playing an important

role in inducing a 3D dispersion. Furthermore, the 3D parameters, evolve according to the level of strain. Moreover, we observe a staircase structure for different photon energies, revealing both the 3D nature of the electronic dispersion and the quantization of the electron wave vector along the direction normal to the film surface. Taking advantage of the wavevector quantization we were able to determine directly the band parameters and map the FS without using the nearly-free-electron approximation (NFEA). Moreover, introducing an effective anisotropic photoelectron effective mass, related to the local structure of the excited band, improves the use of the NFEA for single photon energy measurements.

In parallel, I have built an improved PLD system at the EPFL which can be connected to the SCIENTA analyzer, and which enables us to perform in-situ ARPES measurements at any time rather than only during allocated beamtimes at the synchrotron. We also produced our own targets for the laser ablation and all the films were fully characterized at the EPFL performing X-ray diffraction (XRD), resistivity and magnetic measurements. I analyzed in detail the growth mechanism of Bi-2201 and I investigated the presence of random intergrowths. We developed a model to explain the presence of these polytypes and studied their presence as a function of the deposition parameters and the annealing treatment. The model predicts a very particular spatial distribution of defects: a Markovian-like sequence of displacements along the grow direction, as well as a two-component in-plane correlation function, characteristic of self-organized intercalates. We varied the growth conditions in order to study the presence of intergrowths and to produce single-phase samples. Subsequently, we performed in-situ photoemission experiments on thin films of Bi-2201 films free from intergrowths and we analyzed their FS. This method is successful and can be extended to

2

other related oxide films.

Key words: HTSC, thin films, epitaxial strain, PLD, ARPES, XRD.

Résumé

Mon travail de thèse est centré sur l'étude de la croissance et de l'analyse approfondie de couches minces supraconductrices à haute température critique, dans le but essentiel de mettre à jour leurs proprietés électroniques, notamment par photoémission en résolution angulaire (ARPES: Angle Resolved Photoemission Spectroscopy). J'ai utilisé, en quelque sorte, deux approches complémentaires ainsi que deux différents montages de déposition par laser pulsé (PLD: Pulsed Laser Deposition). Dans le premier, précédemment developpé au Wisconsin, dedié a l'étude des contraintes sur $La_{2-x}Sr_xCuO_4$ (LSCO), le transfert se faisait via une "valise". Le deuxième (in-situ), a été construit par moi-même à l'EPFL, avec un transfert direct vers la chambre d'analyse, dédié essentiellment à l'étude du $Bi_2Sr_{2-x}La_xCuO_4$ (Bi-2201)

ARPES représente l'outil le plus direct pour explorer la structure électronique. Jusqu'à présent ces mesures étaient effectuées au Synchrotron Radiation Center (SRC) (Université de Wisconsin) où nous avions développé un montage expérimental consistant en un système PLD couplé à une chambre d'analyze SCIENTA, à la sortie d'un faisceau synchrotron. La procédure de transfert des échantillons garantit que la qualité de surface de nos couches minces reste préservée lors du déplacement de celles-ci vers l'analyseur ARPES. Notre groupe de recherche avait déjà étudié méticuleusement l'effet des contraintes épitaxiales sur les couches minces de LSCO. Des contraintes épitaxiales compressives changent la topologie de la surface de Fermi (FS) de type "trou" à type "électron". Les contraintes épitaxiales extensives ont montré des résultats complètement différents: les mesures ARPES à une énergie de photon, ont fourni la preuve de la nature tridimensionnelle (3D) de la relation de dispersion électronique, contrairement à la dispersion strictement bidimensionnelle (2D) observée dans les couches minces de LSCO examinées aupar-

avant. Dans cette thèse ce résultat a été confirmé par la recontruction de la FS avec des énergies de photon différentes. Nous avons observé que les contraintes varient en fonction de l'épaisseur des couches minces et que ces contraintes sont déterminantes pour la nature 3D de la dispersion électronique. On peut constater que les paramètres 3D de la structure électronique varient en fonction du champ de contraintes. En plus, nous avons observé que la relation de dispersion présente une structure par paliers (staircase structure) pour chaque énergie de photon utilisée, ce qui révèle, en plus de la nature 3D de la relation de dispersion électronique, la quantification du vecteur d'onde le long de la direction normale à la surface des couches minces. En profitant de la quantification du vector d'onde (wavevector quantization), nous avons pu déterminer les paramètres de bande et dresser la FS sans avoir recours à l'approximation de l'électron libre pour le photoélectron dans l'état final (NFEA: Nearly Free Electron Approximation). Par ailleurs, nous constatons que l'introduction d'une anisotropie de masse effective tenant compte de la structure locale de la bande excitée améliore l'applicabilité de la NFEA pour des mesures à une seule énergie de photon.

En parallèle, j'ai construit un système de croissance de couches minces par PLD au sein de l' EPFL. Ce système est d'autant plus sophistiqué qu'il peut être directement connecté à l'analyseur SCIENTA, ce qui nous permet d'effectuer des mesures ARPES in-situ à tout moment de l'année, sans nous soucier des "beamtimes" au synchrotron. En outre, nous produisons nos propres cibles (targets) pour le processus d'ablation laser et toutes les couches minces ainsi fabriquées sont caractérisées à l'EPFL par diffraction de rayons X (XRD), par des mesures de transport et de susceptibilité magnétique. J'ai analysé en détail les mécanismes de croissance des couches minces de Bi-2201 par PLD et j'ai étudié la présence d'intercalats alétoires (random inter-

growth). Nous avons développé un modèle afin de comprendre l'apparition de
ces polytypes et nous avons étudié leur présence en fonction des paramètres
de croissance ainsi qu'en fonction du traitement de recuit (annealing). Notre
modèle prédit une distribution spatiale très particulière de défauts: une
séquence markovienne de déplacements suivant la direction de croissance,
ainsi qu'une fonction de corrélation dans le plan à deux composantes, car-
actéristique de defauts auto-organisés (self-organized defects). Nous avons
agi sur les paramètres de croissance de sorte à étudier l'émergence des in-
tercalats afin de produire des échantillons sans défauts. Nous avons effectué
des expériences de photoémission in-situ avec des couches minces de Bi-2201
exemptes d'intercalats et nous avons analysé leur FS. Cette methode est très
prometeuse et peut être appliquée à d'autres couches minces d'oxydes lamel-
laires.

Mots-clés: HTSC, couches minces, contraintes épitaxiales, PLD, ARPES,
XRD.

Chapter 1

Introduction

A large number of studies have been carried out on thin films of different high temperature superconductors (HTSC), involving different experimental techniques and theoretical models. The effort to study these materials is motivated largely by the potential applications of thin films in a number of cryoelectronic devices and by the possibility of using epitaxial single or multi-layer HTSC films to study new physical properties of these unique materials. Despite the enormous research effort, the underlying mechanisms responsible for the superconducting properties of the cuprates are still open to question. Nevertheless it is possible to draw a clear picture of our present day understanding of the nature of superconductivity, the universal features and properties of HTSC. The phase diagrams of cuprate superconductors, where the superconducting critical temperature T_c is a function of doping and a material-dependent parameter (MDP), have many common features. The cuprate systems drastically change their behavior depending on the electron density in the 2-dimensional (2D) CuO_2 planes. The basic behavior of the CuO_2 planes are common to all the cuprate superconductors. When the plane has half-filled $d_{x^2-y^2}$ orbitals, the system is an antiferromagnetic Mott insu-

lator. Removing electrons from the insulating CuO_2 plane, i.e. doping with holes, the 3-dimensional (3D) low range antiferromagnetic order is rapidly destroyed and then a transition from the insulator to the superconductor takes place. With further hole doping, the critical temperature, T_c, increases up to a value corresponding to the optimal doping, which for the majority of cuprates coincides with the value of 0.15 - 0.16 carriers per Cu atom. For higher hole doping the T_c decreases again and disappears. Overdoped cuprates behave like a relative conventional metal above T_c, while underdoped cuprates in the normal state show behaviors strongly deviating from the standard Fermi-liquid; this region is usually called "non Fermi-liquid". Therefore, it is essential to know the electronic structure of the CuO_2 planes to understand the cuprate systems. Photoemission spectroscopy is a powerful tool to probe directly the electronic band structure of these materials. Angle Resolved Photoemission Spectroscopy (ARPES) is particularly useful for this purpose. In a typical ARPES experiment, the energy and the parallel momentum of photoemitted electrons are conserved providing us with the dispersion of the observed electronic states $E(k)$ in a selected energy-momentum window. The energy and momentum resolution of nowadays allow detailed investigations of the states close to the Fermi surface where we find the signature of electronic interactions and correlations. Together with photoemission spectroscopies we should combine other characterization techniques in order to fully know the samples. X-ray diffraction (XRD) is an important tool to investigate the structural properties of the samples. Complex systems like HTSC can show many types of defects which have to be understood before doing any PES analysis.

In this thesis work, the electronic band structure, the structural properties and the critical temperature will be analyzed for different HTSC thin

films varying the doping, the substrates, the thickness, and the growing parameters. In chapter 2, I introduce the growing technique: Pulsed Laser Deposition (PLD) is discussed and I present how I have built the new system at the EPFL compared with the one at the Synchrotron Radiation Center (SRC), Wisconsin. The deposition parameters optimization and the growing procedure are described in detail. The system is fully compatible with the EPFL SCIENTA system (at the IPN, Institute de Physique de Nanostructures), thus it can be moved and connected directly in order to perform in-situ photoemission experiments. In Chapter 3 the characterization techniques used for this thesis are presented as well as the corresponding equipment, with a special emphasis on the ARPES technique handled at the EPFL. Chapter 4 is dedicated to the first HTSC material investigated in this work: $La_{2-x}Sr_xCuO_{4+\delta}$ (LSCO). In this chapter, the results obtained are presented with a particular attention to ARPES measurements at the SRC. The Bi-2201 investigations, including the analysis of random intercalates and polytypes as well as in-situ ARPES measurements at the EPFL, are presented in chapter 5, before drawing the concluding remarks.

1.1 Superconductivity

The discovery of superconductivity signed a very important step in the research of new technology but introduced a lot of questions and challenges that a lot of scientists all around the world are trying to solve and to win. Superconductivity is a complex phenomenon concerning some materials, pure elements as well as complex compounds. We can summarize the main characteristics as follows: 1) Zero resistivity: below a certain temperature they show 0 resistance; 2) perfect dimagnetism which is equivalent to the assertion

that there can be no magnetic field inside a superconductor in its superconducting state: the magnetic flux is totally expelled from a superconductor (Meissner effect). By mid of this century, evidence of superconductivity was established in many elements and compounds. A phenomenological approach was introduced in 1950 by Ginzburg-Landau. It considers the superconducting states comprised of all the Cooper pairs as one condensate described by a single complex wave function:

$$\Psi = |\Psi|e^{i\varphi}, \tag{1.1}$$

where Ψ is related to the density of superconducting electrons, n, by $\|\Psi\|^2 = n$ and $\varphi = \varphi(r)$ is spatially varying phase. The basic postulate of Ginzburg-Landau is that if Ψ is small and varies slowly in space, the free-energy density f can be expanded in series of the form

$$f = f_{n0} + \alpha|\Psi|^2 + \frac{\beta}{2}|\Psi|^4 + \frac{1}{2m^*}|(\frac{\hbar}{i}\nabla - \frac{e^*}{c}\mathbf{A})\Psi|^2 + \frac{h^2}{8\pi} \tag{1.2}$$

where f is the free energy in the normal phase, α and β are phenomenological parameters, m^* is an effective mass, $\mathbf{A}$ is the electromagnetic vector potential, and $B = rotA$ is the magnetic induction. By minimizing the free energy with respect to fluctuations in the order parameter and the vector potential, one arrives at the Ginzburg-Landau equations:

$$\frac{1}{2m^*}(\frac{\hbar}{i}\nabla - \frac{e^*}{c}\mathbf{A})^2\Psi + \beta|\Psi|^2\Psi = -\alpha(T)\Psi, \tag{1.3}$$

where $\mathbf{A}$ is the vector potential. The corresponding equation for the supercurrent is

$$\mathbf{J_s} = \frac{e^*\hbar}{2m^*i}(\Psi^*\nabla\Psi - \Psi\nabla\Psi^*) - \frac{e^{*2}}{m^*c}|\Psi|^2\mathbf{A}. \tag{1.4}$$

A few years later a successful microscopic theory was published in 1957 by J. Bardeen, L. N. Cooper, and J. R. Schrieffer (BCS) [9]. The BCS Hamiltonian is given by the following expression in second quantization:

$$H = \sum_{k,s} \xi_k c^{\dagger}_{k,s} c_{k,s} + g \sum_{k,s} \xi_k c^{\dagger}_{k\uparrow} c^{\dagger}_{-k\downarrow} c_{-k'\downarrow} c_{k'\uparrow} \qquad (1.5)$$

where $c^{\dagger}_{k,s}$ and $c_{k,s}$ are the fermion creation and annihilation operators respectively. The first term represents the band energy and the second is the term for the pairing interaction. $g = V_{k,k'}$ is the interaction potential between two electrons in a s-wave symmetry.

This theory is built on the notion of electron pairing: interactions between electrons and the underlying lattice results in an attraction between the electrons. More precisely, two electrons of opposite spin can lower their free energy by the exchange of a boson, and form the so-called Cooper pair. Although this attractive interaction is weak, it can still dominate the Coulomb repulsion when the temperature is sufficiently low. BCS does not take into account fluctuation effects, and it is a typical mean-field theory. The formation of Cooper pairs leads to an energy gap, labelled as 2Δ, near the Fermi level where no single particle states are allowed. 2Δ is the binding energy of the pair and the first excitation level corresponds to the breaking of the pair. Unlike ordinary electrons, these pairs cannot be scattered because the energy transfer of the scattering process would be less than 2Δ and because there are no allowed states for such scattered electrons. Consequently, there is no dissipation and no resistivity.

The BCS theory makes definite predictions for a given superconductor:

- on the gap value: $2\Delta(0) = 3.52 k_B T_c$ and near T_c:
  $\Delta(T) = 1.74\Delta(0)\sqrt{1 - T/T_c}$.

- on the coherence length: $\xi = v_F/\Delta$ where v_F is the Fermi velocity.

- on the critical temperature: $k_B T_c = 1.13\hbar\omega_D exp\left(\frac{-1}{U N_F}\right)$, where ω_D is the Debye frequency, U stands for the electron-electron attractive interaction energy, and N_F is the density of states at the Fermi level.

This theory is able to explain microscopically the low T_c superconductor (conventional superconductors). In addition, the Landau-Ginzburg theory can be derived from the BCS theory (suitably generalized to deal with spatially varying situations) [22], valid near T_c, in which Ψ is directly proportional to the gap parameter Δ. More physically, Ψ can be thought of as the wavefunction of the center-of-mass motion of the Cooper pairs.

1.2 High temperature superconductors: HTSC

In 1986, J. C. Bednorz and K. A. Müller reported superconductivity in $La_x Ba_{1-x} CuO_4$ at about 30 K [11]. All the cuprate superconductors have some common features, for instance, perovskite is the typical crystal structure of HTSCs. A model for the perovskite structure is Barium titanate ($BaTiO_3$). The perovskites are characterized by the ideal structure ABX_3 shown in Fig. 1.1: A is the metallic cation (transition metal) with the highest radius, B is the smallest cation (rare earth element)and, X is the non metallic anion (oxygen). There are two kinds of cubic perovskites which differ from one another for the two cation positions: the "type a" has the cation A in the center and the "type b" has the cation B in the center but the relative atomic positions are the same. Cuprates with the ideal perovskite structure do not exist because Cu, occupying the position of the cation B, never assumes the regular octahedral position, since, depending on his valence state, it can have linear, planar square, pyramidal or distorted octahedral coordinations. The

main reason for this crystallographic complexity is due to the fact that the majority of cuprates do not have a fixed oxygen stoichiometry. This implies different spatial coordinations and valences for copper [59]. The main common feature of all the cuprates is the fact that conductive CuO_2 planes are separated by block layers as show in Fig. 1.2. In the case of $La_{2-x}Sr_xCuO_4$ systems, the block layer is the La-O double plane whereas in Bi-2212 or Bi-2201 compounds the block layers are Sr-O and Bi-O planes. The block layers play the role of a charge reservoir: the cation in these planes form an ionic bond with oxygen to which it transfers its valence electrons. These layers are responsible for doping the CuO_2 plane with holes or with electrons. A notable exception is the $YBa_2Cu_3O_{7-\delta}$ family, which also has metallic Cu-O chains. In general, the planar nature of the square CuO_2 layers results in a highly 2D electronic structure (typical resistivity anisotropies, ρ_c/ρ_{ab} are up to the order of 10^4) where the electrons are largely confined within the planes. This layered structure also results in easily exposed cleavage plane which is highly advantageous for ARPES. The Bi-based compounds, such as $Bi_2Sr_2CaCu_2O_{8+\delta}$ are particularly micaceous and can even be tape cleaved.

Through chemical substitution of cations in the block layers or through oxygen intercalation, one can alter the stoichiometry of these materials, thereby introducing mobile carriers into the CuO_2 planes in a manner similar to semiconductor doping. The materials which have undoped CuO_2 planes (i.e. stoichiometric) are commonly referred to as "parent compounds", meaning that there is one unpaired electron per CuO_2 plane. Within the context of band theory, this half filling would imply that these materials should be good metals. However, in the case of the parent cuprates, these compounds are antiferromagnetic insulators with a gap of about 2 eV. This insulating gap arises due to the strong Coulomb repulsion between electrons on the Cu-
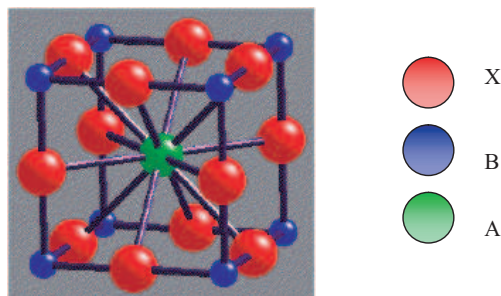
Figure 1.1: Crystallographic structure of the cubic perovskite.

$3d$ and O-$2p$ orbitals, and are commonly known as charge transfer insulators [62], where the Coulomb repulsion energy dominates over the gain in kinetic energy associated with the delocalization. Formally speaking, the cuprates are charge-transfer insulators: the presence of this gap, and the fact that non-interacting band theory predicts a fundamentally incorrect ground state, is a direct and dramatic example of the strong electron-electron correlations in cuprates.

The precise mechanism of HTSC is not yet fully understood and so far, there is not yet a microscopic theory, like BCS for the conventional super-conductor, able to explain it.

1.2.1 Phase diagram

The generic phase diagram of cuprates shows a wide variety of behaviors at different temperatures and levels of doping. Depending on the carrier density in the CuO_2 plane, the physical properties of the cuprates change drastically. As an example, the phase diagram of LSCO [46] is shown in Fig. 1.3. There is a global symmetry of the phase diagram between hole-doped and electron-doped superconductors in that, on doping an antiferromagnetic insulator (AFI) first turns into a superconductor and then eventually into a
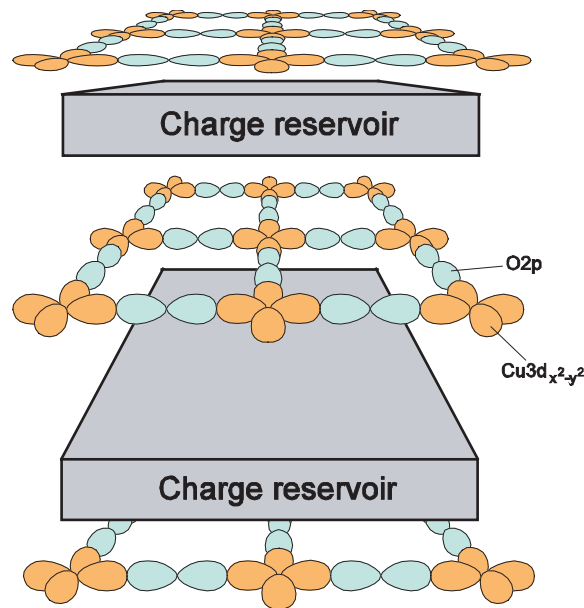
Figure 1.2: 2D CuO_2 planes separated by block layers.
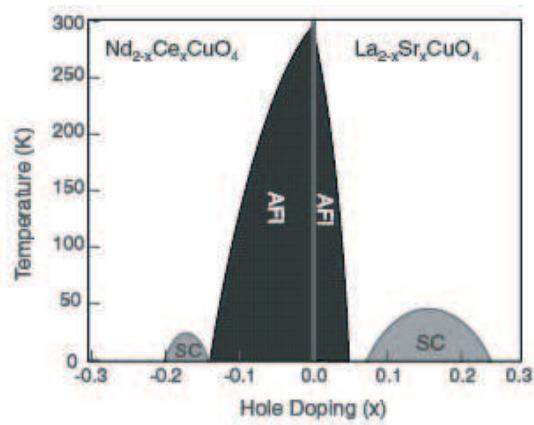
Figure 1.3: Phase diagram of electron doped (on the left) and hole doped (on the right) cuprates.

metal. However, in many aspects electron-doped and hole-doped HTSCs are different. It is evident from the phase diagram in Fig. 1.3, that an antiferromagnetically ordered phase is much robust against doping in electron-doped.

In the parent compound La_2CuO_4 ($x = 0$), due to the valence of La^{3+}

and O^{2-}, the valence of Cu is +2 within the ionic picture. Since Cu^{2+} has nine electrons (or one hole) in the Cu-3d band (d^9 configuration), the band with the highest energy is half-filled. Contrary to the prediction of the band theory, undoped La_2CuO_4 is an antiferromagnetic Mott insulator with a Néel temperature of $T_N \simeq 300$ K because of strong electron interactions. The antiferromagnetic region is the best understood region in the phase diagram. At zero doping the cuprates are all insulators, and below a few hundred Kelvin they are also antiferromagnets (i.e. the electron spins on neighboring copper ions point in opposite directions). Removing electrons from the insulating CuO_2 planes may be regarded as hole doping. When the doping is increased above a critical value, the antiferromagnetic state disappears and we enter the so-called "pseudogap" in the underdoped region. Typically around a hole concentration of $x \sim 0.07$, although this varies between material families, superconductivity arises. The superconducting transition temperature, T_c, continues to increase with hole doping until a maximum transition temperature, which usually occurs around a hole concentration of $x \sim 0.16$, a value known as "optimal doping". This optimal doping value also varies slightly from family to family among the cuprates. Above this optimal doping concentration, T_c declines with further hole doping until superconductivity is lost, usually around $x \sim 0.25$. Samples with hole doping levels below optimal doping are typically referred to as "underdoped", while samples above optimal doping are referred to as "overdoped". The maximum transition temperature (T_c at optimal doping) ranges from approximately 25 K for the lowest T_c families and to up to 160 K (under pressure) for the highest. This is in obvious contrast to nearly all conventional BCS superconductors which typically have T_cs below 10 K, with a few notable exceptions. Another unusual aspect of the HTSCs is the presence of a gap with a $d_{x^2-y^2}$

symmetry (l = 2), which results in ungapped electronic excitations along the Brillouin zone diagonal, even at T = 0 K [57].

In addition to the unusually high transition temperatures and the unconventional symmetry of the superconducting gap, the high T_c compounds also exhibit highly anomalous properties above T_c, i.e. in the normal state. In a conventional superconductor, such as lead, the material exhibits metallic properties at temperatures above T_c. However, the underdoped cuprates do not behave like ordinary metals, or in fact any other known materials, above T_c, but continue to exhibit highly unusual normal-state properties. For instance, a gap in the single-particle electronic channel persists above the critical temperature, even though this gap can no longer be representative of the superconducting order parameter. This normal-state gap is typically referred to as a "pseudogap", whose microscopic origin is still a topic of great debate [53].

1.2.2 How we deal with the HTSC

For our investigations, we chose ARPES as the main measurement technique as it enables one, together with other ex-situ methods used in this thesis, to understand the mechanisms that govern the electronic properties and superconductivity. However, X-ray diffraction (XRD) is fundamental in order to understand the photoemission properties. ARPES is the most direct method to determine the electronic band structure and XRD the most direct method to determine crystal structure and defects. It is a matter of fact that the quality of materials is crucial for investigations of HTSC cuprates, hence a major part of the thesis was dedicated to the optimization of film heteroepitaxy and characterization.

ARPES is performed with radiation in the ultraviolet or soft X-ray range.

We performed our measurements at the SRC and at the IPN, EPFL (M. Grioni). At the EPFL we worked with a He gas discharge tube, where only fixed energies (21.2 eV, 40.8 eV) are available, while at the synchrotron we can tune the photon energy from 10 to 200 eV with a higher light intensity. ARPES technique requires a high sample quality and especially very clean surfaces. It is well known that it is not easy to cleave thin films. Single crystals are difficult to cleave properly, except Bi-based cuprates. This is one of the main reasons why it was important to have a PLD system for in-situ film growing at the synchrotron. I have constructed a PLD system at the EPFL, which can be directly connected to the SCIENTA in the IPN laboratory. In this way we can perform photoemission measurements in any period of the year, not only during beamtimes. Once the experimental obstacles are overcome, the combination of film growth and the in-situ ARPES measurements open new horizons for the exploration of HTSCs and related oxides.

Chapter 2

Pulsed Laser Deposition: construction and optimization

All the films studied in his thesis have been grown by the PLD technique. In this chapter, the main mechanism of PLD is described at first. Then the construction of the PLD system at EPFL is presented in comparison with the system at the SRC. Particular features that make it suitable for in-situ ARPES measurements at the EPFL are evidenced as well.

2.1 The physics of PLD

PLD [24] is a thin film deposition (specifically a physical vapor deposition, PVD) technique [49] where a high power pulsed laser beam is focused inside a vacuum chamber to strike a target of the desired composition. Material is then vaporized from the target and deposited as a thin film on a substrate, such as a silicon wafer facing the target. This process can occur in ultra high vacuum or in the presence of a background gas, such as oxygen which is commonly used when depositing oxides to fully oxygenate the de-
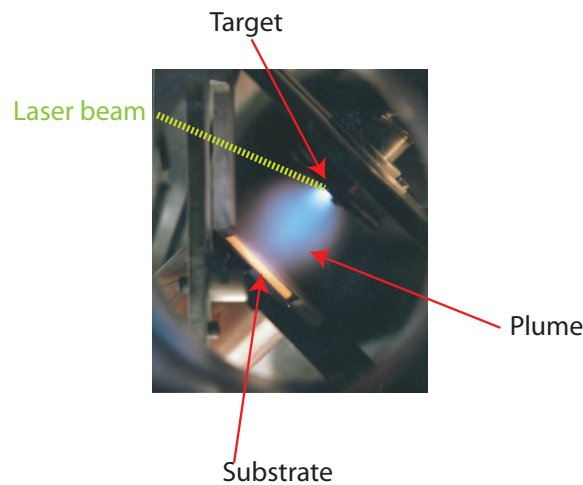
Figure 2.1: PLD scheme.

posited films. Typically, each pulse of the laser has a duration length of a few nanoseconds. The main advantage of PLD derives from the preservation of the target stoichiometry, which is fully transferred to the film. PLD is a photon-material interaction that creates an ejected "plume" from any target. The vapor (plume) is collected on a substrate placed at a short distance away from the target. Though the actual physical processes of material removal are quite complex, one can consider the ejection of material to occur as a rapid explosion of the target surface due to superheating. Unlike thermal evaporation, which produces a vapor composition dependent on the vapor pressures of elements in the target material, the laser-induced expulsion produces a plume of material with stoichiometry similar to the target. It is generally easier to obtain the desired film stoichiometry for multi-element materials using PLD than with other deposition methods. Conceptually the principles of PLD are simple: a laser vaporizes a target surface producing a film with the same composition as the target.

The principle of PLD, in contrast to the simplicity of the system set-up, is

a very complex physical phenomenon. It does not only involve the physical process of the laser-material interaction of high-power pulsed radiation on solid targets, but also the formation of the plasma plume with high energetic species and even the transfer of the ablated material through the plasma plume onto the heated substrate surface. The thin film formation process in PLD generally can be divided into the following four stages:

1. Laser radiation interaction with the target

2. Dynamics of the plasma

3. Deposition of the ablation materials on the substrate

4. Nucleation and growth of the film on the substrate surface

Each of these steps influences the crystallinity, uniformity and stoichiometry of the resulting film. In the first stage, the laser beam is focused onto the surface of the target. The technique of PLD uses high power laser pulses, typically of the order of 10^5 Wcm^{-2}, to melt, evaporate and ionize material from the target surface. At sufficiently high flux densities and short pulse duration, all elements in the target are rapidly heated up to their sublimation temperature. The ablation of the target material upon laser irradiation produces a transient, highly luminous plasma plume that expands rapidly away from the target surface. The removal of atoms from the bulk material is done by vaporization of the bulk in a state of non-equilibrium at the surface region and is followed by an abrupt adiabatic expansion, also called "Coulomb explosion" at the end of the pulse. The incident laser beam penetrates into the target surface within the penetration depth. This dimension is dependent on the laser wavelength and the index of refraction of the target material at the applied laser wavelength and is typically in the region of 10 nm for

most materials. The strong electrical field generated by the laser radiation is sufficiently strong to remove the electrons from the bulk material of the penetrated volume. This process occurs within a time scale of typically 10ps and is caused by non-linear processes such as multiphoton ionization, which are enhanced by microscopic cracks at the surface and voids, increasing the electric field. The surface of the target is heated up and the material is vaporized. The temperature of the generated plasma plume is typically 10^5 K.

It must be emphasized that the physical conditions of PLD are by far less well defined than for Molecular Beam Epitaxy (MBE). PLD is an out-of thermodynamic equilibrium technique [32, 55] due to the short time of the pulse. The particles deposited may be atoms, clusters, or even droplets. They may arrive with energies ranging from 0.1 to 1000 eV. The most common non-equilibrium phenomenon in PLD is the possible overheating. This critical stage does not only depend upon the time profile of the laser pulse but also upon the actual value of fluence: this overheating occurs on one hand because of a kinetic mechanism, i.e. when the heating rate overcomes the bubble nucleation or surface recession rates, on the other hand because of an insufficient energy dissipation mechanism with respect to the incoming pulse fluence. Both situations are however clearly typical for a non-equilibrium thermal sputtering process. The laser-target interaction causes surface evaporation and boiling processes implying a surface temperature gradient $\nabla T|_{z=0} \neq 0$. The afore-going expression implies a net heat transfer towards or from the vapor plume, unlike a thermodynamic equilibrium process whose net heat balance tends to zero. For the plume, actually, we cannot define one, unique equilibrium temperature. The "pulse" feature of the PLD makes the thermalization process impossible: the system, before the next

pulse is generated, does not have enough time to reach the thermodynamic equilibrium.

In spite of many advantages of PLD, there are also some weaknesses going together with this deposition technique. One of the major problem is the deposition of droplets on the film surface. The presence of the droplets results from the splashing effect, which brings the melted droplets or detached fragments of the target to the film surface. The size of the droplets may be up to a few micrometers. Such droplets affect the growth of the following layers as well as the properties of the film. The use of an off-axis geometry, i.e. by orienting the substrate parallel to the beam, is an effective measure to prevent large droplets. Under these conditions, high kinetic energy droplets travel through the background gas avoiding the substrate; only the thermalized vapor close to the substrate surface can condensate.

2.2   The PLD construction

The system I constructed at the EPFL is conceived in a compact way. The main characteristics are similar to the one located at the SRC [1, 19], but some changes have been made in order to make it flexible and more efficient. The scheme in Fig. 2.2, is similar to the scheme of the system in Madison, but the main difference concerns the direction of the laser beam with respect with the UV window. The inclination of the UV window is such that the normal direction is pointing towards the target and not towards the center of the chamber.

The heater is made up of a shielded resistive cable from Thermocoax (Fig. 2.4). The shape of the oven is adapted to the one of the sample holder which is SCIENTA compatible. The geometry configuration of the holder is
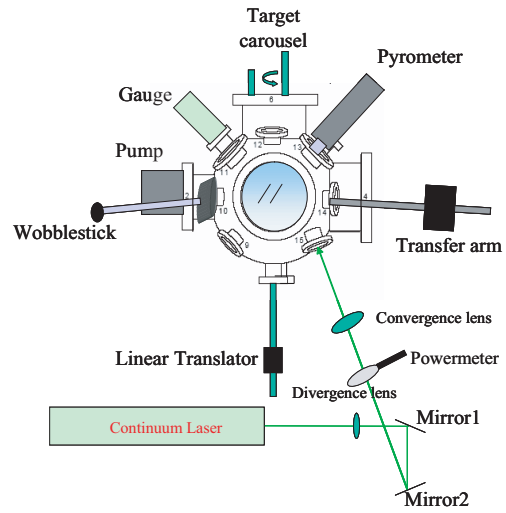
Figure 2.2: PLD scheme.
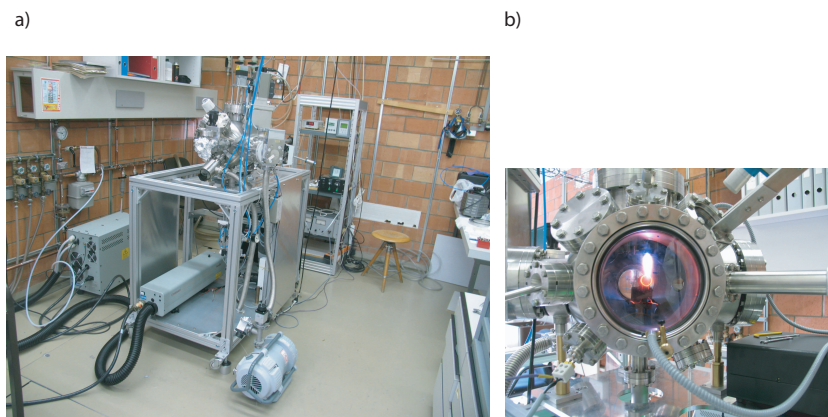
Figure 2.3: a) The PLD system at the EPFL. b) Interior of the PLD chamber during the film deposition.
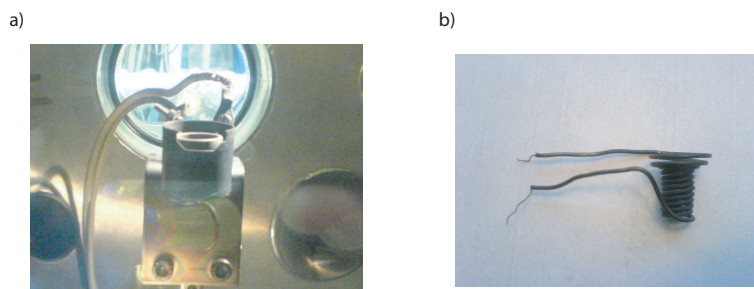
Figure 2.4: a) Picture of the oven inside the deposition chamber and b) shows the heater alone, consisting of the heating wire.

suitable for both on-axis and off-axis deposition. The whole heater can be easily dismounted and mounted in a different geometry. The current passing in the heating cable through a feedthrough is manually controlled by a DC power supply. The temperature is measured by a pyrometer pointed on the substrate and previously calibrated. The distance between the target and the substrate can be opportunely adjusted. The laser is a pulsed YAG laser, with maximum repetition rate of 10 Hz. The highest obtainable wavelength is 1064 nm and using the second and the fourth harmonic generator one can obtain wavelengths of 529 and 266 nm respectively. Nd:YAG (neodymium-doped yttrium aluminium garnet; $Nd:Y_3Al_5O_{12}$) is a crystal that is used as a lasing medium in solid-state lasers. The dopant, triply ionized neodymium, typically replaces the yttrium in the crystal structure of the yttrium aluminium garnet, since they are of similar size. Generally the crystalline host is doped with around 1% neodymium by weight. We deposited all the films using a wavelength $\lambda = 266$ nm and the corresponding energy for this wavelength is 80 mJ per pulse at 10 Hz. We used a deposition rate of 10 Hz for YBCO, whereas for LSCO and for Bi-2201 we used 3 Hz.

The constructed system has one important advantage: it is compatible with the SCIENTA system at the IPN laboratory of Prof. Marco Grioni.

Wheels have been mounted in order to move the whole system to the SCI-ENTA. Moreover, the height of the system can be properly adjusted for a perfect connection, which allows for direct transfer into the photoemission chamber. As shown in Fig. 2.2, the system is equipped with a series of manipulators (wobblestick, linear translator, magnetic transfer arm) used to transfer the sample after deposition.

After deposition, the films are transferred first in the LEED chamber and consequently into the ARPES photoemission chamber. In addition, it is possible to load new samples into the PLD chamber preserving the vacuum.

2.3 The deposition parameters optimization

2.3.1 YBa$_2$Cu$_3$O$_{7-\delta}$

The YBa$_2$Cu$_3$O$_{7-\delta}$ (YBCO) is one of the most studied superconductors, mostly grown using laser ablation techniques [31, 60]. The first superconducting YBCO thin films have been grown by PLD in 1987 [23]. This event marked a breakthrough for PLD and since then, many materials that are normally difficult to deposit by other methods, in particular polycomponent oxides, have been successfully deposited by PLD.

We had chosen this compound for the optimization of the deposition parameters in order to calibrate our system. Its unit cell (UC) structure is shown in Fig. 2.5. It is made up by 3 perovskite-related units [59] stacked in the c-direction. The UC of a superconducting YBCO is orthorombic with lattice parameters verifying $a \approx b \approx c/3$. Two kinds of Cu site are present. The oxidation state of Cu is unusual. If we assume that Y, Ba and O have their usual oxidation (valence) states of +3, +2, and -2 respectively, then for charge balance, Cu must be present at an average of +2.33. This might
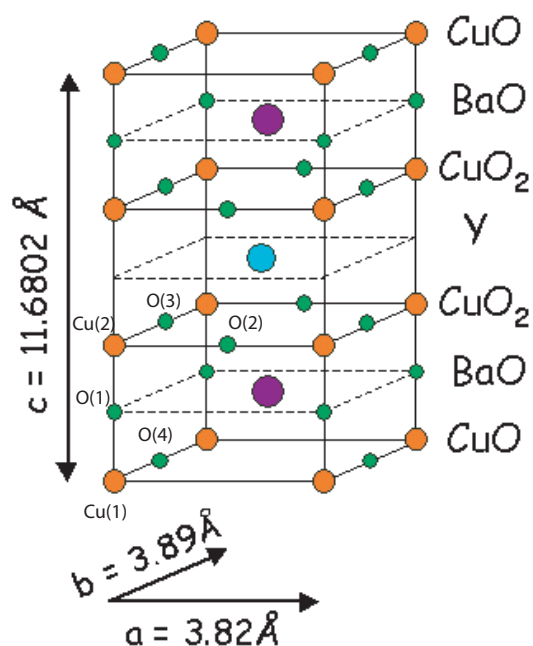
Figure 2.5: Crystal structure of YBa$_2$Cu$_3$O$_7$.

be rationalized in terms of a +2 state for square pyramidal Cu (2), of which there are two in the UC and a +3 state for square planar Cu(1), of which there is one per UC. In perovskites, these sites would be octahedral, but because of the oxygen deficiency, one is five-coordinate (square pyramidal arrangement) and the other is four-coordinate (square planar). The key to the superconducting behaviour in YBa$_2$Cu$_3$O$_7$ certainly appears to be the Cu atoms, their oxidation states and the manner in which they link up to the O to form the complex structure within the UC. Superconductivity may be destroyed by partial reduction of the structure. YBCO does not have a fixed oxygen content since δ can be varied easily over the range $6 < \delta < 7$ simply by heating the material at different temperatures and at different oxygen partial pressures. There are structural consequences of removing oxygen: at $\delta = 6$, all O(4) (chains) oxygen sites are empty and the coordination

of Cu(1) is reduced to 2 (linear). Hence, on removal of oxygen, the Cu(2) remains primarily as Cu^{+2} whereas Cu(1) is reduced. With decreasing δ, the value of T_c decreases and superconductivity is no longer observed for $\delta \leq 6.4$. The oxygen content is determining also the structural properties of YBCO. Depending on temperature and oxygen content, $y = 7 - \delta$, two polymorphous changes are possible: tetragonal for $y \leq 6.5$ and orthorombic for the range $6.5 < y < 7$. The orthorombic phase is superconducting. The orthorombic deformation decreases directly proportional with the oxygen content; for $y \sim$ 6.5 the phase is tetragonal. By heating over 540 °C temperature at 1 atm pressure, is beginning the oxygen loss and at 900 - 950 °C temperature, y = 6. A reversible structural transition arises at 575 °C.

2.3.2   Growing procedure

In order to optimize the growing of YBCO we fixed the oxygen pressure during the deposition and the post-annealing treatment and we changed the growing temperature. We observed an evolution of the structural and superconducting properties with the growing temperature, an effect that has already been observed in YBCO in previous works [27, 28]. The main result is summarized in Fig. 2.6. The physical meaning of the Rocking Curve (RC) is explained in chapter 3 and in the Appendix in chapter 6. The RC is measuring the in-plane crystallinity. The in-plane crystal coherence length is inversely proportional to the full width at half maximum (FWHM) in the RC diffractogram. The optimal conditions are represented in Fig. 2.7: these optimal conditions gave rise to the narrowest RC, shown in Fig. 2.6, indicating an optimized in-plane crystallinity. The deposition time is varied for the purpose of the film thickness one wants to obtain. For YBCO the deposition rate amounted typically to about 3 Å /sec.
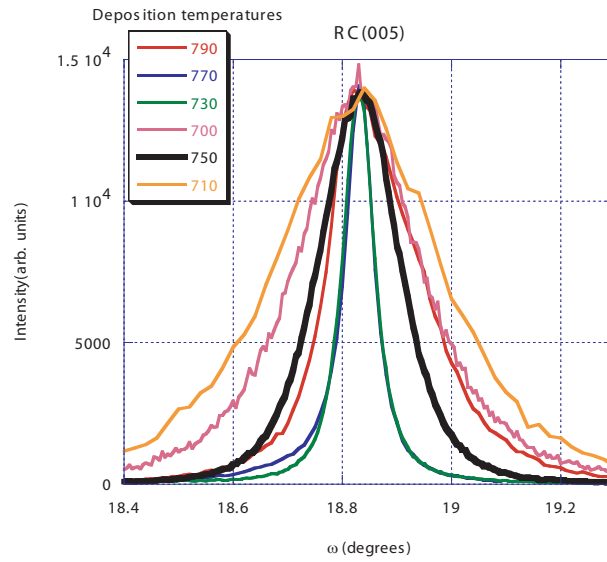
Figure 2.6: RCs around the (005) for films grown at different deposition temperatures.
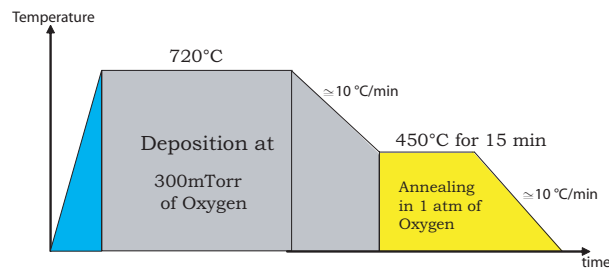
Figure 2.7: Schematic representation of the deposition and post-annealing conditions for YBCO thin films.
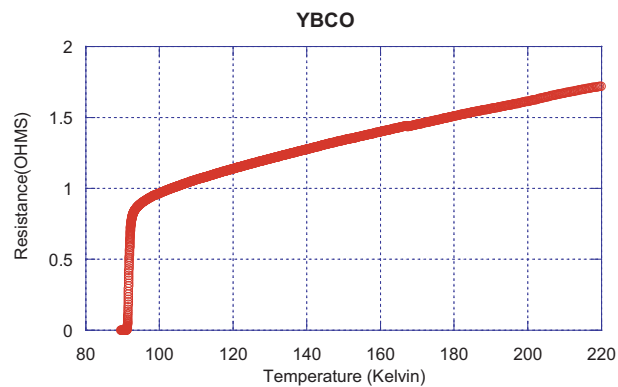
Figure 2.8: Resistance measurement of a YBCO thin film grown at the optimal conditions.
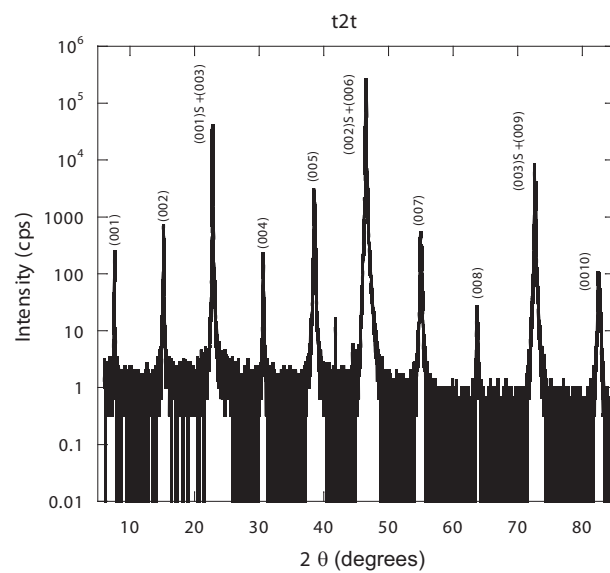
Figure 2.9: $\theta - 2\theta$ diffractogram.
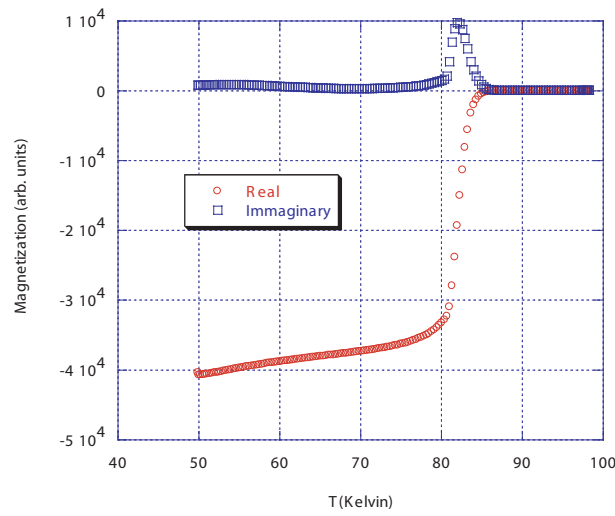
Figure 2.10: AC susceptibility measurement of a YBCO film.

In Fig. 2.8 and in Fig. 2.10 we show the critical temperature and XRD measurements. The better quality films have a T_c of 90 K and the X-ray diffractogram evidences just the presence of one single YBCO phase oriented along the (00l) direction (Fig. 2.9).

Chapter 3

Characterization methods

In order to characterize the grown thin films we perform resistivity, susceptibility and XRD measurements, which, combined with photoemission techniques, give a complete insight into the film properties. ARPES plays a central role especially because this technique is the most appropriate method for the determination of the electronic band structure. All these characterization methods are necessary in order to achieve a comprehensive analysis of the film properties and to understand the band structure results. In this chapter we describe all the characterization methods used for studying the films and we point out the information we can extract from the measurements.

3.1   X-ray diffraction

XRD is a very powerful and at the same time non-destructive tool for the structural and composition determination of the samples. Our diffractometer is a SEIFERT ID3003 in a Bragg-Brentano geometry. We perform $\theta-2\theta$ scans to determine whether unwanted phases or misoriented regions are present in
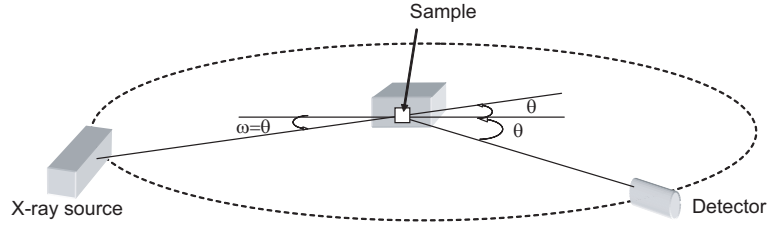
Figure 3.1: X-ray geometry used for the structural characterization of the films.

the films and, through the determination of the peak positions, the lattice parameters as well as the level of strain in the thin films. Together with the $\theta - 2\theta$ analysis we performed RC measurements. The RC is done by fixing the 2θ position corresponding to a Bragg angle and moving the ω around this position (in specular geometry: $\omega = \theta$). This method provides us with information about the in-plane quality of the film: a narrow RC indicates a high in-plane coherence and hence a low density of dislocations (see Appendix in chapter 6). The c-axis of the film was calculated for each peak with Bragg's law:

$$2c\sin(\theta) = n\lambda, \tag{3.1}$$

where c represents the value of the c-axis, n the order of the observed peak and λ the wavelength of the X-ray radiation. The c-axis values evaluated on all the film peaks are systematically plotted versus $cos^2(\theta)/sin(\theta)$ in order to minimize the errors arising from sample misalignment. The intersection of the extrapolated c-axis with the ordinate gives the nominal c-axis value of the corresponding film. This can be easily seen by considering Bragg's law. Eq. 3.1 permits us to write:

$$\frac{\Delta c}{c} = -\frac{\mathrm{d}\theta}{\tan\theta}. \tag{3.2}$$
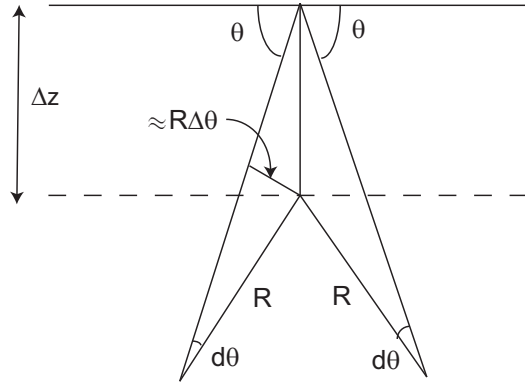
Figure 3.2: Error along z-axis when mounting the sample

We can express the measured value of the c-axis, c, by

$$c = c_0 \pm \left| \frac{\Delta c}{c} \right| c_0, \qquad (3.3)$$

where c_0 represents the actual c-axis and Δc the uncertainty in its measurements. Replacing the relative error in Eq. 3.2 we obtain

$$c = c_0 \left(1 - \frac{\mathrm{d}\theta}{\tan\theta} \right). \qquad (3.4)$$

The dominant uncertainty in θ is related to the uncertainty along the z-axis when mounting the sample. It is shown in Fig. 3.2 how these two uncertainties are related. We can thus write

$$\Delta z = R \frac{\Delta\theta}{\cos\theta}. \qquad (3.5)$$

Replacing $\mathrm{d}\theta \approx \Delta\theta$ in Eq. 3.4 by the use of Eq. 3.5 we get

$$c = c_0 - c_0 \frac{\Delta z}{R} \left(\frac{\cos^2\theta}{\sin\theta} \right). \qquad (3.6)$$

From the last equation it is clear that plotting the c-axis in function of $\cos^2\theta/\sin\theta$, the intersection with the ordinate yields the actual c-axis value.
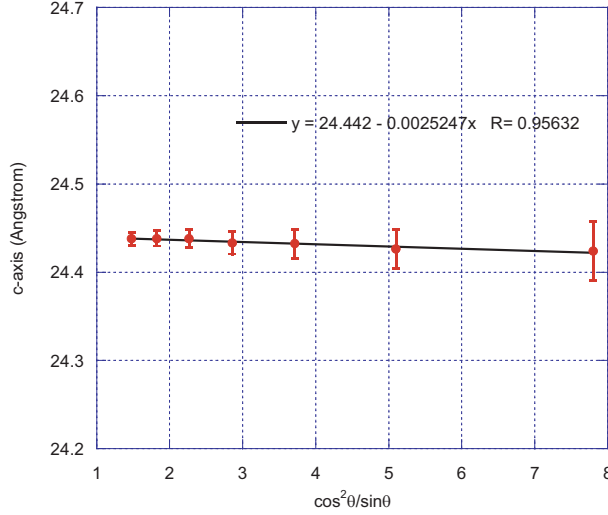
Figure 3.3: Plot of c-axis as a function of $\cos^2\theta/\sin\theta$. The equation of the linear fit is indicated and the real c-axis value (24.442 Å) is the intercept point with the ordinate.

The determination of the film thickness is not always trivial. When the film is thin or very thin, it is possible to observe the emergence of finite size oscillations, that are an indication for high surface quality. The estimation of the film thickness is possible in this case by fitting them using the following formula:

$$
m_1 \left[\left(\frac{\sin\left(\frac{2\pi m_2 * c_{axis}}{\lambda_1}\sin\left(\frac{\pi}{180}\frac{2\theta}{2}\right)\right)}{\sin\left(\frac{2\pi * c_{axis}}{\lambda_1}\sin\left(\frac{\pi}{180}\frac{2\theta}{2}\right)\right)} \right)^2 + 0.5 \left(\frac{\sin\left(\frac{2\pi m_2 * c_{axis}}{\lambda_2}\sin\left(\frac{\pi}{180}\frac{2\theta}{2}\right)\right)}{\sin\left(\frac{2\pi * c_{axis}}{\lambda_2}\sin\left(\frac{\pi}{180}\frac{2\theta}{2}\right)\right)} \right)^2 \right],
$$
(3.7)

where the parameters m_1, m_2 are respectively the intensity of the central lobe and the number of UCs (thickness). Eq. 3.7 is the so-called "Fraunhofer formula" for the interference, as it is explained in the Appendix in chapter

6. When the finite size oscillations do not appear because of the roughness of the surface or if the film is too thick, the evaluation of the film thickness is done by using the "Scherrer formula":

$$t = \frac{0.9\lambda}{\cos(\theta)\Delta\theta},$$

(3.8)

where θ is the Bragg angle, $\Delta\theta$ is the difference in radians [rad] of the instrumental angular resolution (evaluated from the FWHM of the substrate peak) and the observed FWHM of the film peak.

3.2 Electrical resistivity

The four-point electrical probe is a very versatile device, that is used widely in physics for the investigation of electrical phenomena. The effects of contact resistance can be eliminated with the use of a four point probe. Furthermore the thermoelectric voltage, arising from thermoelectric offsets, can be cancelled using the voltage measurements made at a positive test current and a negative test current. This is called a *delta reading* or *delta mode*. The delta technique eliminates the error due to changing thermoelectric voltages. I have constructed such a resistivity system using a precise current source and a nanovoltmeter to measure the voltage drop between the contacts. The temperature is measured with a silicon diode mounted under the sample and opportunely calibrated. The four-contacts on the sample are made using four thin golden wires, that are attached with conductive silver paint. The sample is consequently immersed slowly in liquid helium. The data of the resistivity measurements as a function of the temperature are collected and directly displayed in real time by a Labview program.

3.3 AC susceptibility

The magnetic AC susceptibility [21] as a function of the temperature with different amplitudes and frequencies of the applied field is used to characterize the magnetic properties of HTSC [18]. The general form of the magnetization of a material in an AC magnetic field is sinusoidal at the frequency of the applied field, but it can be shifted in phase relative to the applied field. The general form for the magnetization can be expressed as:

$$M = H_0(\chi\prime \cos(\omega t) + \chi\prime\prime \sin(\omega t)). \tag{3.9}$$

A material's susceptibility can then be specified as a complex constant:

$$\chi = \chi\prime + i\chi\prime\prime, \tag{3.10}$$

and the magnetization phasor can be expressed as

$$M = \chi H_a, \tag{3.11}$$

where H_a denotes the applied (external) magnetic field. The physical meaning of $\chi\prime$ and $\chi\prime\prime$ is the following [29]: the energy converted into heat during one cycle of the AC field is

$$W_q = -2\pi\chi\prime\prime \frac{B_a^2}{2\mu_0}. \tag{3.12}$$

This expression explains why the lock-in can be used to determine AC losses. Because W_q is always negative, $\chi\prime\prime$ in a correctly designed experiment must be positive. The time average of the magnetic energy stored in the volume

occupied by the sample is

$$W_m = \chi\prime \frac{B_a^2}{2\mu_0},\tag{3.13}$$

where the normal-state value was taken as the reference level, i.e. $W_m(T > T_c) = 0$. Diamagnetic behavior leads to the reduction of the magnetic field compared with the normal paramagnetic state, reflected in a negative value of W_m. Thus we expect in the case of a superconductor that $\chi\prime < 0$. The real component (in-phase) of the susceptibility measures the slope of the $M(H)$-curve. The imaginary part (out-of-phase) indicates dissipative processes in the sample. The measuring method consists of applying an alternating magnetic field to the sample by means of a primary coil and detecting with a system of two secondary coils oppositely wound and connected in series, the variation of flux due to the sample located in one of unbalanced secondary coils (Fig. 3.4). The signal delivered by the system of the secondary coils is analyzed by a lock-in amplifier which gives a signal proportional to the complex susceptibility of the sample which can be separated into a real part ($\chi\prime$) and an imaginary part ($\chi\prime\prime$) under appropriate conditions. If $\chi\prime\prime = 0$, the magnetization will be perfectly in phase with H_a for a paramagnetic material ($\chi\prime > 0$) and will be 180° out of phase for a diamagnetic material ($\chi\prime < 0$). With non-zero values of $\chi\prime\prime$, the magnetization, given by Eq. 3.9, will be neither perfectly in-phase nor out-of-phase with the applied field. It turns out that only positive values of $\chi\prime\prime$ are physically possible (and thus that the magnetization can only lag the applied field). That only $\chi\prime\prime > 0$ is physically possible can be seen from the relationship between the sign of $\chi\prime\prime$ and the direction of energy flow between the sample and the applied field. The power density p (power per unit volume) absorbed in the sample is simply $p = -M\frac{dB_a}{dt}$. One can easily show that the power density averaged over a complete cycle, p_{av}, is given by $p_{av} = \frac{1}{2}\mu_0\omega H_0^2\chi\prime\prime$. Only $p_{av} > 0$, this
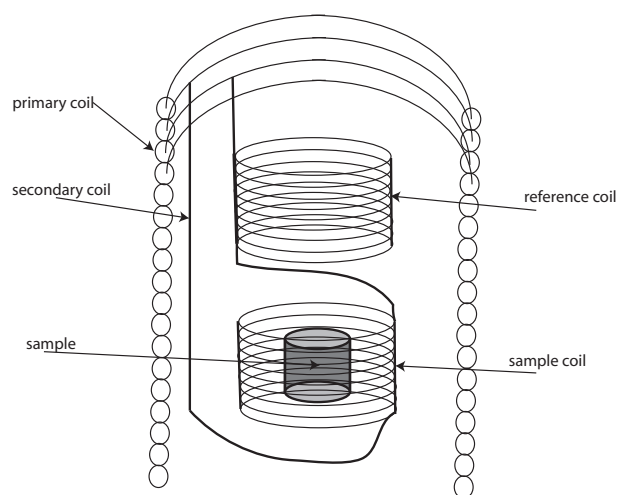
Figure 3.4: Scheme of the AC susceptibility set up.

means χ'', is energetically possible. In this case, the sample absorbs energy from the applied field, which goes into heating the sample. Were $p_{av} < 0$ (i.e. $\chi'' < 0$), rather than absorbing energy, the sample would be continually radiating energy: this would be inconsistent with the second law of thermodynamics.

The magnetic field inside the material must vanish in the case of a superconductor and the effective magnetization must obey $M = H_a$, i.e. $\chi' = -1$ and $\chi'' = 0$. Typically, the onset of a significant nonzero χ' is taken as the superconducting transition temperature. The out-of-phase component of the susceptibility is non-zero for the temperature slightly below the transition temperature, where magnetic irreversibility occurs in the sample. A typical AC susceptibility measurement is shown in Fig. 2.10 in chapter 2.

3.4 Photoemission spectroscopy (PES)

Photoemission is a photon-in/electron-out experiment. A monochromatic photon beam in the UV or X-ray range impinges on the sample inducing the emission of photoelectrons, that are subsequently collected and analyzed.

A PES measurement is intrinsically very sensitive to surface conditions. Photoelectrons can travel only very short distance (about 5 - 20 Å in the 5 - 2000 eV energy range) inside a solid without suffering inelastic collisions with other electrons, phonons, and so on. For most materials the energy dependence of the electron mean free path follows the universal U-shaped curve of Fig. 3.5. The scattered electrons rapidly "lose memory" of their initial states, and their contribution is a shapeless background rising away from the Fermi level and peaking near the low-energy limit of the spectrum. The "real" spectrum originates from the very first atomic layers of the sample,
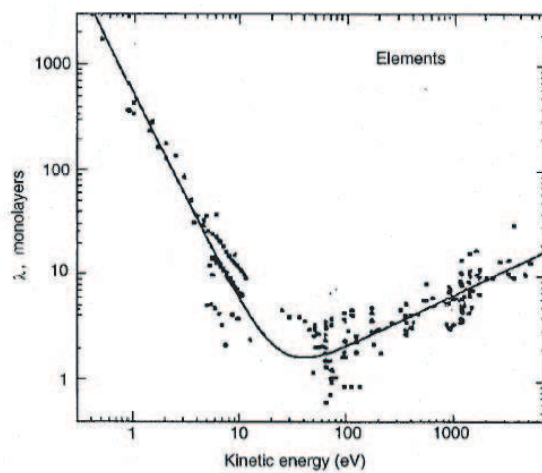
Figure 3.5: Dependence of attenuation length, λ, on kinetic energy.

and it is therefore extremely important to limit the contamination of a freshly prepared surface by keeping the pressure in the experimental apparatus at the lowest possible value. This is why the PES measurements of solids are performed in an ultra-high (10^{-9} - 10^{-11} Torr) vacuum environment. As we have mentioned previously, photoemission is the phenomenon that a material irradiated by light emits electrons. Knowing the kinetic energy E_{kin}^{ν} of the emitted electron in the vacuum, one can deduce how strong the electron was bound to the material. Owing to the energy conservation law, we can write

$$E_{kin}^{\nu} = h\nu + E_B - \Phi, \qquad (3.14)$$

where $h\nu$ is the energy of the incident photons, E_B is the negative binding energy relative to the Fermi level E_F (chemical potential μ) and Φ is the work function of the material under study. The physical meaning of Φ is the energy required for the electron to escape from the solid through the surface and to reach the vacuum level E_{vac}, that is $\Phi = E_{vac} - E_F$. In practical PES experiments, since both the sample and the electron energy as well as the electron energy analyzer are grounded, the measure of the kinetic energy is referred to E_F:

$$E_{kin}^{\nu}(E_F) = h\nu - \Phi_a. \qquad (3.15)$$

where Φ_a is the work function of the analyzer. The energy distribution of the electrons inside the material can be directly mapped by the distribution of the kinetic energies of the emitted photoelectrons after the bombardment of the sample with monochromatic photons. In the band-model interpretation, PES (IPES) measures transitions between states in occupied and empty bands. These transitions are vertical in a reduced zone scheme (energy and wavevector conservation) and therefore occur without the participation of

other excitations. They are called vertical or direct transitions. Via direct transitions it is possible, in principle, to determine the band structure of the occupied and unoccupied bands.

The most commonly used model for the interpretation of photoemission spectra in solids is the so-called three-step model (Fig. 3.6), developed by Berglund and Spicer [12]. It is a purely phenomenological approach, which has nonetheless proved to be very successful. It breaks up the complicated PE process into three steps: the excitation of the photoelectron, its passage through the solid to the surface and its penetration through the surface into the vacuum, where it is detected. After the electron is excited by the incoming photon, the photoelectron migrates towards the surface. The dominant scattering mechanism that reduces the number of photoexcited electron reaching the surface with the final energy E_f is the electron-electron interaction. The electrons which can escape into vacuum are those for which the component of the kinetic energy normal to the surface is sufficient to overcome the surface potential barrier. The other electrons are totally reflected back into the bulk. Inside the crystal the electron travels in a potential of depth E_v - E_0. In order to escape into the vacuum the electrons must satisfy the condition

$$(\hbar^2/2m)K_\perp^2 \geq E_v - E_0, \tag{3.16}$$

where E_0 (< 0) is the energy of the bottom of the valence band and $K_\perp$ is the component of the wavevector of the excited electron, $\mathbf{K}$, normal to the surface. The transmission of the electron through the surface leaves the parallel component of the wave vector conserved since the surface is an equipotential (there is no in-plane electric field component):

$$\vec{k}_{//}^{\,vac} = \vec{k}_{//}^{\,fin} = \vec{k}_{//}^{\,ini} + \vec{G}_{//}, \tag{3.17}$$

where $\vec{G}_{//}$ is a vector of the reciprocal lattice, parallel to the surface. For the perpendicular component of **K** there is no conservation. The special shape of the potential barrier the electron has to overcome to escape out of the solid to the vacuum is not known. That is the reason why $\vec{k}_{\perp}^{fin}$ cannot be easily determined. The wavevector of the photoelectron outside the crystal is $\mathbf{p}/\hbar$. We can then write

$$|\vec{k}^{vac}|^2 = \frac{2m}{\hbar^2} E_{kin}, \tag{3.18}$$

and in addition

$$k_{//}^{in} = k_{//}^{vac} = \sqrt{\frac{2m}{\hbar^2} E_k} \sin\theta. \tag{3.19}$$

The kinetic energy is measured by the analyzer with respect to the vacuum, i.e.

$$E_k = h\nu - \phi + E_B \implies E_B = E_k - h\nu + \phi. \tag{3.20}$$
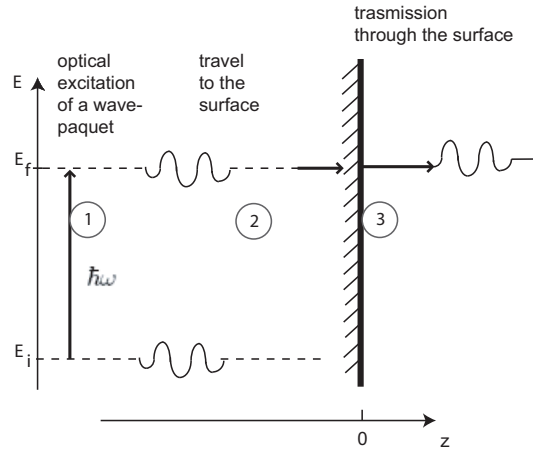
Figure 3.6: Illustration of the three steps model.

3.4.1 Angle resolved photoemission spectroscopy (ARPES)
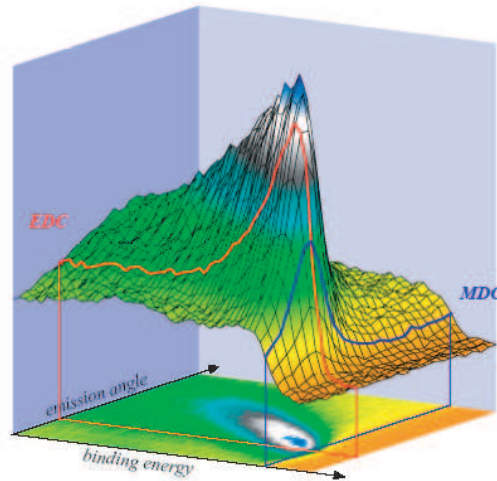
Figure 3.7: Illustration of a typical ARPES experiment and its outcome. Photoelectrons are emitted from the surface and collected with an analyzer as a function of the emission angle and kinetic energy. The obtained information is usually summed up in intensity maps as shown here. The spectra can be analyzed in two equivalent representations: as energy distribution curves (EDCs) shown here in red, or as momentum distribution curves (MDCs) represented by the blue line.

In ARPES experiments [34, 33] not only the energies but also the momenta of the electrons in the materials are probed (otherwise, we call it angle-integrated PES). A typical outcome of an ARPES experiment and a schematized setup are shown in Fig. 3.7. Photoelectrons ejected by the monochromatic light are collected by the analyzer that gathers them as a function of energy and angle. Single channel analyzers usually collect the intensity as a function of kinetic energy, the so-called energy distribution curves (EDCs), repeatedly for successive angles of emission. EDCs are affected by the Fermi cut-off, thus it is not easy to determine the position of the maxima for the band dispersion for low lying energy bands. The momentum distribution curves (MDC) on the contrary are not affected by the

Fermi cut-off and they represent a more appropriate tool for the derivation of the band dispersion for bands cutting the Fermi level (E_F).

First, upon the photoexcitation process, the crystal momentum should be conserved. The momentum of the incident photon can be neglected since it is very small compared with the one of the electron. In ARPES experiments, the kinetic energy E_{kin} and the angular directions of the momentum (θ and ϕ) of photoelectrons are measured using a directional electron energy analyzer. Therefore, we obtain the momentum of the emitted electron $\mathbf{p}_{//} = (p_x, p_y)$ as

$$
\begin{aligned}
p_x &= \sqrt{2m_e E_{kin}^v} \cos\phi \sin\theta, \\
p_y &= \sqrt{2m_e E_{kin}^v} \sin\phi \sin\theta
\end{aligned}
\tag{3.21}
$$

for the geometry shown in Fig. 3.8. The Fermi energy E_F corresponding to
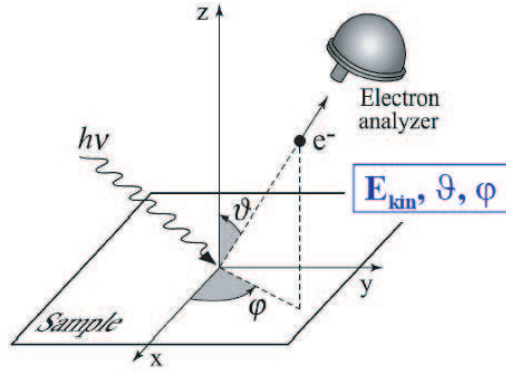
Figure 3.8: Experimental ARPES setup.

$E_B = 0$ is determined by the work function of the analyzer. We calibrated the instrument by measuring the Fermi edge on a gold sample. Since the sample and the analyzer are in electrical contact (grounded) the Fermi level is sample-independent. Fig. 3.9 schematically illustrates the procedure for the band mapping. If the material under investigation is a 2D system such as

high-T_c cuprates, the knowledge of E_{kin} and $\mathbf{k}_{//}$ contains enough information for mapping the energy-momentum dispersion of the band structure. The situation is more complicated when the material shows a 3D dispersion. In this case, we have to introduce k_z (or $k_\perp$) to which we have no access. $k_\perp$ is indeed not conserved and there is no way to derive this quantity because we have no knowledge of the potential profile across the surface. Moreover, there is no direct relation between the measured quantities $\mathbf{p}_{//}$ and $\mathbf{p}_\perp$ and the quantity $\hbar K_\perp$ which one needs in order to obtain the band structure without any further assumptions.

To overcome this problem one can make the assumption about the final state using the so called "free-electron model" where a free-electron final state is assumed. Since the optical excitation takes place in the presence of a crystal potential, the free electron final state can be regarded as an approximation. A photon is incident at an angle ϕ with respect to the surface normal and via the photoemission process electrons are liberated from the sample and are detected in a solid angle $d\Omega(\theta, \phi)$.

3.4.2 A typical ARPES experiment within our current set-ups

The basic parts of the instrumentation are the light source, the UHV chamber and the detector. The source of light for ARPES is a UV lamp or a synchrotron beam in the UV to soft X-ray range. In the IPN laboratory of Prof. Grioni, there is a Scienta ESCA-300 spectrometer equipped with a high-brilliance monochromatized He lamp. The Fermi energy location and the total energy resolution $\Delta E = 10$ meV are separately determined from the metallic edge of a polycrystalline Ag film. The analyzer is hemispherical energy analyzer PHOIBOS 150 with an angular resolution more accurate
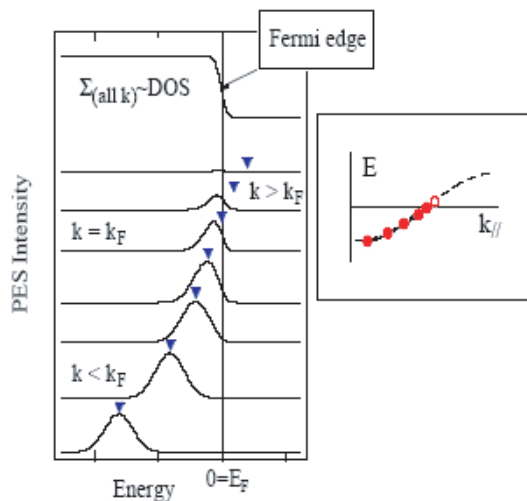
Figure 3.9: Schematic diagram showing the principle of ARPES. The band dispersion relation (showed in the inset on the right) of the material is directly mapped by the ARPES spectra (EDC on the left).

than 1°. The measurements performed at the SRC, were realized on the 6m planar grating monochromator (PGM) beamline by means of a SCIENTA SES-2002 analyzer with an energy resolution of 10 meV and a momentum resolution of about 0.04 Å^{-1}. Synchrotron radiation, is the most versatile source of photons for photoemission, due to its tunability, polarization and intensity.

All the samples discussed in this thesis were prepared in-situ or quasi in-situ. Unfortunately, it is not possible to cleave thin films and we know very well that the quality of the surface plays a crucial role in the photoemission experiment. Degradation of the surface is faster in the presence of a He lamp due to higher pressure in the measuring chamber, whereas in a synchrotron the vacuum is higher because the pressure typically amounts to about 10^{-11} - 10^{-12} mbar, which allows us to perform measurements over a longer period. Samples analyzed at EPFL were directly transferred to the SCIENTA cham-

ber, straightaway connected with the deposition chamber. Samples produced in our set-up in Madison cannot be directly transferred in the analysis chamber. After the deposition, the samples are loaded in a suitcase in 1 atm of pure oxygen and consequently transferred in the ARPES chamber.

Chapter 4

Structural and electronic properties of $La_{2-x}Sr_xCuO_4$ thin films

In this chapter the electronic properties of $La_{2-x}Sr_xCuO_4$ (LSCO) films under tensile strain will be investigated. The electronic band structure turns out to be strongly related to the strain applied on the film. We try in this chapter to extract a strain profile on the basis of a structural investigation of films of different thickness and in parallel we relate it to the electronic properties measured by ARPES. All the LSCO films were grown at the SRC, Wisconsin, where were also performed all the ARPES measurements (Fig. 4.2).

4.1   The main properties

The crystal structure of LSCO is shown in Fig. 4.1. The UC is body centered and it consists of two identical blocks, one above the other and shifted by half a lattice constant in the x- and y-directions. For LSCO the block layer

is the La-O double plane. The block layers play the role of charge reservoirs. Replacing a fraction of La^{+3} ions by Sr^{+2} ions, electrons are withdrawn from the CuO_2 planes, which increases the T_c. On the other hand, the oxygen deficiency or excess is much less controlled during the crystal growth procedure and it is difficult to determine. The simplicity of the crystal structure of LSCO is an advantage for studying the electronic structure of the CuO_2 plane itself. LSCO has single CuO_2 planes, while Bi2212 and YBCO systems have double CuO_2 planes. The influence of strain for LSCO seems to be more pronounced than in other materials [38, 39]. Epitaxial strain can be induced in LSCO thin films by using a mismatched substrate. Since we grow thin films by PLD, we can explore the effect of epitaxial strain on the structural and electronic properties. Our group has previously studied in detail the effect of compressive strain on the electronic band structure [1]. The first evident effect of the compressive strain was the doubling of the critical temperature T_c [50]. A strong effect was also observed on the electronic structure: the band dispersion resulted in the striking disappearance of the saddle point at $(\pi,0)$, closing the FS in "electron-like" [2].

We study the effect of tensile strain induced by STO substrate in samples with different thicknesses.

Establishing a strain profile on the basis of the examination of the lattice and electronic structures of LSCO is a fundamental stride towards the understanding of the results. Compressive and tensile strain appeared to have completely different effects on the structure and consequently also on the electronic properties. Indeed, the strain is strongly affecting the band structure as it is shown by the ARPES results obtained on LSCO [2, 20]. In our specific case, we focus on the tensile strain and we expect an in-plane tensile strain induced by the substrate. According to the theory of elasticity,
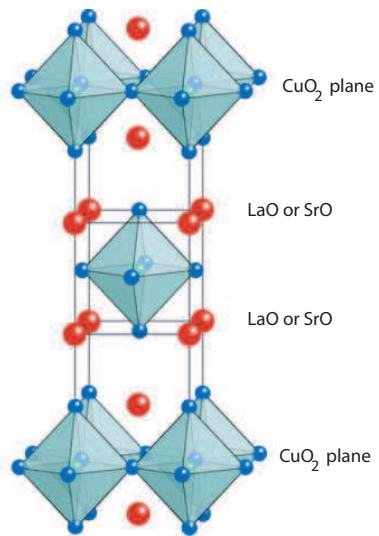
Figure 4.1: Crystal structure of $La_{2-x}Sr_xCuO_4$.
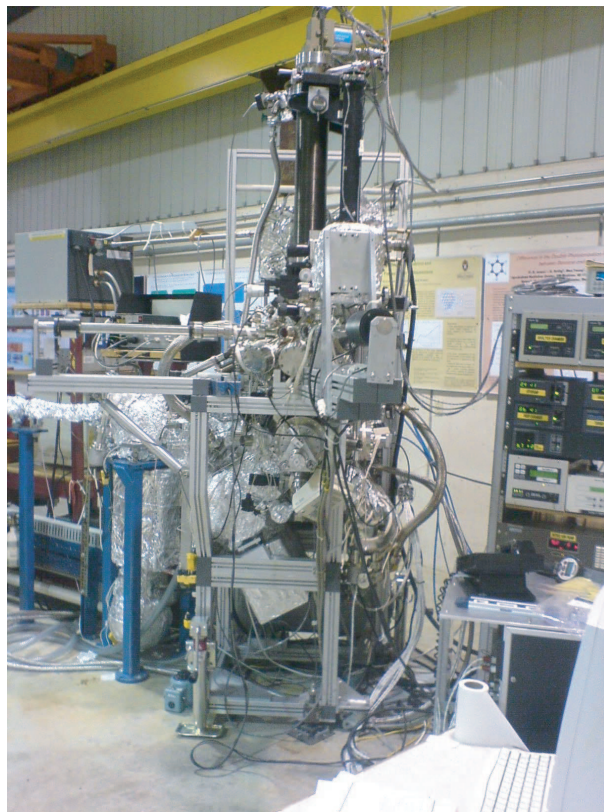
Figure 4.2: ARPES system at the SRC in Wisconsin.

by reason of the Poisson's modulus, an in-plane tensile strain implies a diminished value of the c-axis. In the work by D. Cloetta [20], the presence of strain was evidenced exactly by the c-axis reduction. However, it is possible, in some cases, that the effect of a diminished c-axis in thin films under tensile strain can be masked by the presence of interstitial oxygen. Moreover, this c-axis-based method gives a very rough and, sometimes even an unreliable estimation of the strain present in a film. We introduce an approach which comprehends the picture of a gradually varying in-plane tensile strain as a function of film thickness. In our assumption every crystal layer reveals a different strain state. We have grown a series of films of different thicknesses ranging from 10 to 50 UCs. Independently from the O_2 trapping, we expect that these films have different levels of strain and we try to extract the corresponding strain profile. This step is very important in relation to the ARPES measurements: the different levels of strain (different thicknesses) imply different effects on the electronic band structure.

4.2 Experimental results

4.2.1 X-ray analysis

The powerful and simultaneously non-invasive technique of XRD affords us deep insight into the structural texture of the investigated thin films. The X-ray analysis of a first series of films reveals that the value of the c-axis is not reduced as one would expect from the elastic distortion due to the in-plane tensile strain. The most plausible explanation invokes an excess of interstitial oxygen. It is highly probable that non-stoichiometric oxygen infiltrates the crystal structure of the film during its growing process. Within the crystal structure, excess oxygen has the tendency to enhance the value of

c-axis comparison

y = 13.223 + 0.0083799x R= 0.94175

y = 13.18 + 0.01192x R= 0.70058

c-axis [Å]

$\cos^2\theta/\sin\theta$

before annealing
after annealing
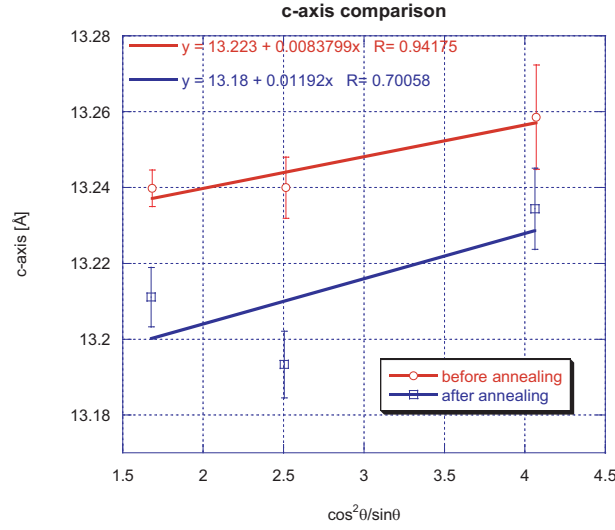
Figure 4.3: Comparison of the c-axis of a film of LSCO before and after vacuum annealing.

the c-axis, masking the effect of in-plane tensile strain. In order to confirm this scenario we performed an annealing of the films in vacuum (10^{-7} mbar). This annealing has been carried out at a temperature of 300 °C during 30 minutes. In Fig. 4.3 the values of the c-axis of a film before and after vacuum annealing are compared. The film after the annealing reveals a smaller c-axis confirming the hypothesis of the afore supplementary entrapped interstitial oxygen. Indeed, this c-axis based method turns out not to be a reliable strain indicator. The inspection of the RC on the contrary, can enlighten some important information about the in-plane texture. The analysis on the strain profile was carried out together with David Oezer in his Master thesis work. The fundamental information to obtain the strain profile were extracted from the RC data. In Fig. 4.4 we plot the RCs for different samples of different thicknesses. For very thin films ($N = 12$ UCs, Fig. 4.4 a)) we observe one sharp line in the RC diffractogram. The profile is fitted by one Lorentzian

function of the form $\frac{A}{1+\left(\frac{2(\omega-\omega_0)}{\Delta\Omega}\right)^2}$, centered around the relative position $\omega_0 = 13.15°$ with a FWHM of the order of instrumental broadening $\Delta\Omega = 0.03°$. In the Fig. 4.4 b) we observe one sharp Lorentzian line shape of the order of instrumental broadening and a broad contribution of a FWHM of 1.18°. The number of UCs, N, is given by 18. In a thicker film (Fig. 4.4 c)) we distinguish a third arising component in the spectrogram of the order of instrumental broadening. At the same time, the larger contribution reveals a slightly diminished value of its FWHM value, amounting to 1.08°. In Fig. 4.4 d), the manifestation of a second coherent film peak becomes more evident with increasing film thickness. Furthermore the larger line shape in the diffractogram continues in diminishing, its FWHM just amounts to 0.77°. Increasing further the thickness (Fig. 4.4 e)) the trend observed in the preceding two spectrograms seems to be confirmed: the second sharp intensity peak grows in intensity while the broad contribution loses in importance, its FWHM just amounts to 0.64°. This film counts 43 UCs. In general we can state the following elementary occurrences in the RC spectrograms:

- For very thin films ($N < 18$ UCs) we observe one single Lorentzian contribution of instrumental broadening. We are thus concerned with a quasi perfectly coherent in-plane crystalline structure.

- As the film thickness increases we discern, in addition to the sharp coherent peak, a broad Lorentzian contribution appearing with an increasing FWHM.

- At a critical film thickness, referred to as Z^*, the FWHM of the broad contribution seems to have reached its maximum value because the broadening of the FWHM is decreasing with the film thickness. In addition, we observe the appearance of a second peak of instrumental

broadening; this contribution grows in intensity as the film thickness increases.

Fig. 4.5 visualizes the evolution of the FWHM of the broad contribution obtained from a Lorentzian fit as a function of the number of the UCs, N.
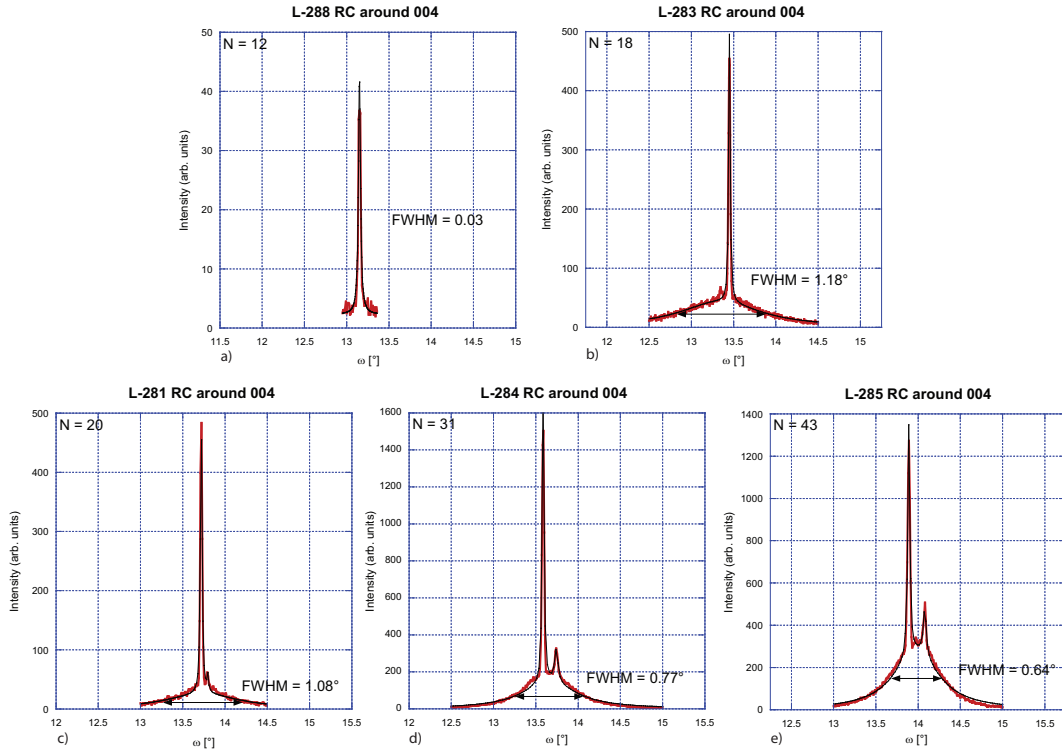
Figure 4.4: a), b), c), d) RC of LSCO films around the 004. The thickness is indicated in each diffractogram.

To explain these results, we propose a static simple growth model [47] based on the following assumptions:

- PLD is an out-of-equilibrium technique and we consider it as a layer-by-layer growing process: each layer deposited it is immediately "frozen" and the following will adapt on it.
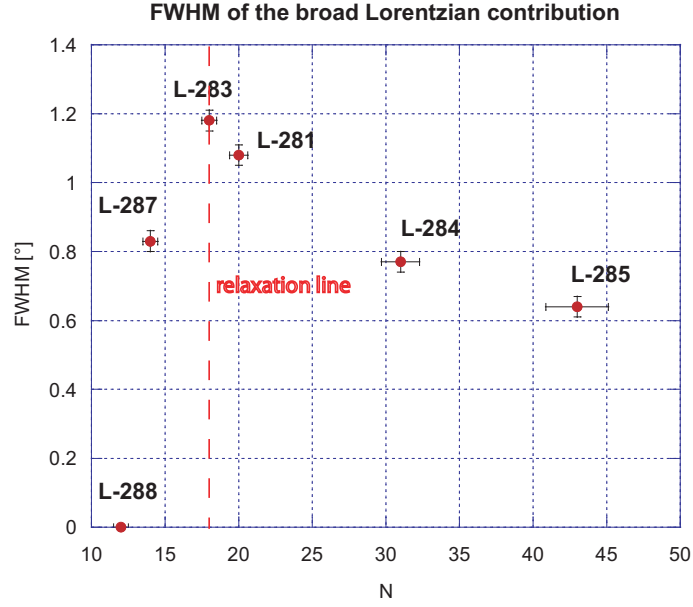
Figure 4.5: FWHM [°] of the broad Lorentzian contribution as a function of the number of UCs N. At the value $N^* = 18$ one observes an inversion point.

- The incoming layer is forming on the last one without having any memory of the history of the previous layers.

- The growth mechanism depends on the local equilibrium. Every step of crystalline growth occurs in such a way that the increment of internal energy from one layer to the next is minimized.

From the graph in Fig. 4.5 we notice the presence of an inversion point at around $N^* = 18$ UCs. In the model we proposed [47], we obtain the expression of the critical thickness Z^*. The mathematical formalism of the model, used in our RC analysis, is explained in section 6.3 of chapter 6. At first glance, one could discern three distinguishable regimes during the epitaxial growth process with reference to the experimental data presented so far: a

complete coherent epitaxial film growth under tensile strain induced by the substrate, subsequently a regime where the strain is gradually relaxed by the introduction of misfit dislocations, and thenceforward a further film growth of a complete relaxed bulk material once the critical film height Z^* has been transcended. The emergence of a RC spectrogram is due to a superposition of the contributions of *every* film layer, modulated by the density of misfit dislocations, $\frac{1}{\xi}$, given in the following equation derived in the Appendix:

$$\frac{1}{\xi}(Z) = -\frac{c}{a_0}\varepsilon' = \frac{c\tilde{\varepsilon}^2}{a_0\lambda}\frac{1}{\cosh^2\left(\frac{\tilde{\varepsilon}}{\lambda}(Z^* - Z)\right)}. \tag{4.1}$$

The main result of this model is the following expression of the strain profile

$$\varepsilon(Z) = \tilde{\varepsilon}\tanh\left(\frac{\tilde{\varepsilon}}{\lambda}(Z^* - Z)\right), \tag{4.2}$$

where Z^* is given by

$$Z^* = \frac{\lambda}{\tilde{\varepsilon}}\text{arctanh}\left(\frac{\varepsilon(0)}{\tilde{\varepsilon}}\right) \tag{4.3}$$

and represents the critical thickness for which the strain becomes zero, i.e. for which total relaxation is attained. In terms of our model of epitaxial film growth, we recognize the strain-relaxation regime in the films revealing a total thickness up to 18 UCs. As the film thickness is very small ($N \leq 12$ UCs), a quasi perfectly in-plane coherence is present. The strain is supposed to be very important and the density of misfit dislocations is kept to a minimum. For increasing film heights, the strain is more and more reduced by introduction of misfit dislocations. This relaxation seems to be completed at the film thickness corresponding to $N^* = 18$, the critical number of UCs. In the post-strain regime, there is no need for a further inserting of misfit dislocation lines and apparently a coherent epitaxial film growth is possible again.

4.3   ARPES measurements on LSCO thin films with interstitial oxygen

We performed ARPES measurements on a series of overdoped ($x = 0.2$) LSCO thin films under tensile strain with different thicknesses. The height of the films was varied between 10 and 59 UCs. The very thin films showed a band dispersion changing with the photon energy, characteristic of a 3D dispersion. We show in Fig. 4.6 an example where the crossing point along $\Gamma - X$ is changing with the photon energy. We would expect for these layered materials a 2D band dispersion, usually observed in films completely relaxed or under compressive strain [2]. However, due to the effect of the tensile strain, perceivable only in very thin films, we observe a 3D electronic band dispersion.

We analyzed two different series of films: films which show interstitial oxygen masking the effect of the strain on the c-axis and films without O_2 trapped and with shorter c-axis. A common feature in both kinds of films was the observation of k_z vector quantization. It is important to underline
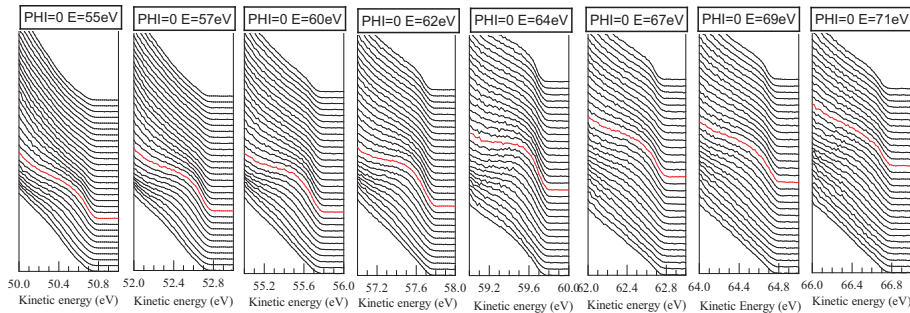
Figure 4.6: Band dispersion at different photon energies for a film of $N = 20$ UCs.

the fact that photoemission measurements could only be possible on samples of very smooth surface. In the same samples we could observe finite size

oscillations in the XRD analysis. Indeed, these finite size oscillations are an indicator of high surface quality.

4.3.1 k_z vector quantization

The study of LSCO films under tensile strain started already with the PhD thesis of Dominique Cloetta. Unfortunately, he investigated the band structure of the films using only one photon energy. We tried to confirm his results and to complete his work using a wide range of photon energies and more samples of different thicknesses.

The first samples we analyzed evidenced the presence of interstitial oxygen and their band dispersion data collected show very interesting features. We observe a staircase structure in the band dispersion as shown in Fig. 4.7 and a dependence on the photon energy. Due to the non-conservation of the normal component of the wavevector across the sample surface, the extraction of the 3D band parameters from ARPES data usually relies on the nearly-free-electron-approximation (NFEA). We have already explained in chapter 3 that in presence of a 3D dispersion one must use an ad-hoc approximation since we have no access to the $k_\perp$. In the past, we already used a 3D tight binding (3DTB) in order to fit the data on films under tensile strain [19].

We observe that the data collected at different photon energies show all a step-like feature. When we try to fit single photon energy data within the 3DTB using the usual NFEA it was impossible to retrieve the experimental probing path in the reciprocal space. A better approach for this kind of results is taking into account the electron wavevector quantization (WVQ)[6]. Thus, the observed staircase evidenced in Fig. 4.7 structure can be easily interpreted in terms of wavevector quantization for 3D band dispersion [43]:
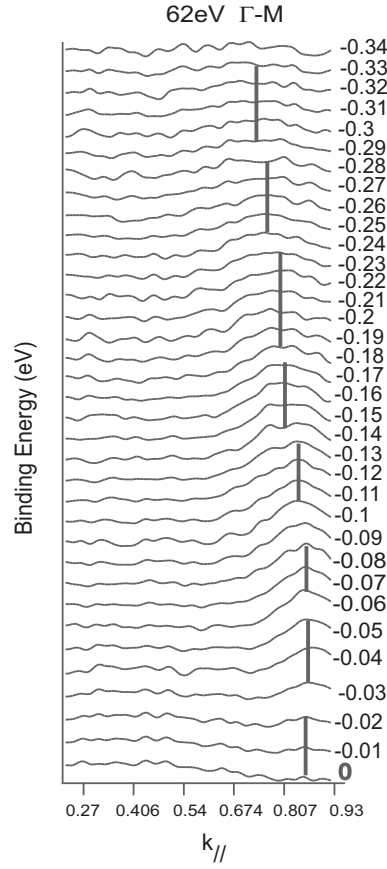
Figure 4.7: MDCs of a 12 UCs sample. The vertical lines evidence the staircase structure in the dispersion.

the probing surface for the given photon energy intersects the set of quantized constant $k_z^{(n)}$ planes in the reciprocal space. At each intersection, for a given in-plane direction (Γ-M in Fig. 4.8), the photon is probing a particular electronic state of the $k_z^{(n)}$ branch. However, due to the finite momentum resolution, electrons belonging to a given branch can be photoemitted in a finite angular interval around the corresponding allowed k_z value, highlighting a finite segment of the discrete $k_z^{(n)}$ branch. In Fig. 4.8, we show the band dispersion obtained at different photon energies together with the calculated discrete dispersion branches at constant $k_z^{(n)}$. The different quantum levels
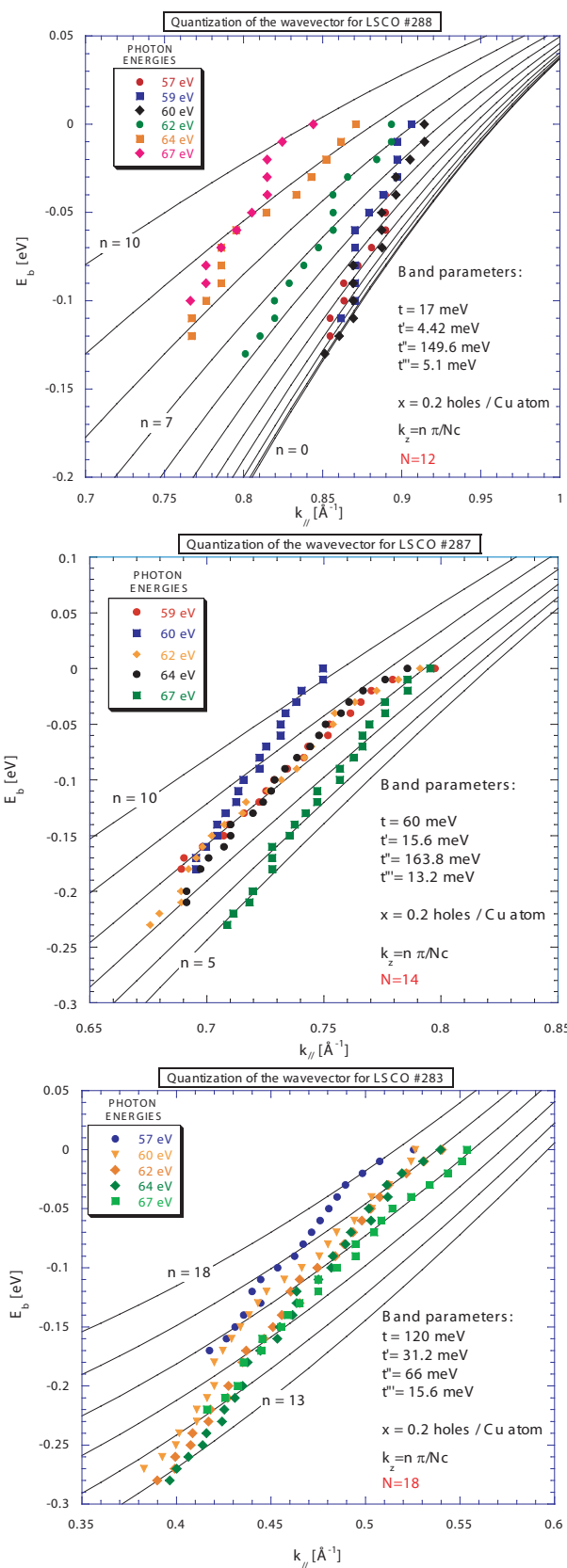
Figure 4.8: Dispersion along $\Gamma - M$ direction obtained at different photon energies and fits with the discrete 3DTB model for quantum levels indexed by $n = 0, 1, 2$ ... for three films with different thicknesses. N represents the number of UCs.

are depending on the thickness of the sample as it is shown in Fig. 4.8 for three samples of different thicknesses. To fit the dispersion we use a discrete version of the generic 3DTB model discussed in Ref. [20]:

$$E_b^{(n)}(\vec{k}) = (\mu - E_F) - 2t \left(\cos(k_x a) + \cos(k_y a) \right) + 4t' \cos(k_x a) \cos(k_y a)$$
$$-8t'' \cos\left(\frac{k_x a}{2} \right) \cos\left(\frac{k_y a}{2} \right) \cos\left(\frac{k_z^{(n)} c}{2} \right) + 2t''' \cos(k_z^{(n)} c), \quad (4.4)$$

where the coefficients affecting the in-plane terms are denoted as t and t', for the nearest neighbor and the second nearest neighbor respectively. t'' and t''' are the out-of-plane contribution (first and second neighbor respectively). $k_z^{(n)}$ is quantized and defined by the following expression:

$$k_z^{(n)} = \frac{n\pi}{Nc}, \quad (4.5)$$

where n is an integer corresponding to the quantum levels, N is the total number of UCs, and c denotes the film's c-axis.

By inserting the band parameters obtained from the fits in the continuous version of Eq. 4.4 we can reconstruct the 3D FS. In Fig. 4.9, we show the FS for the thinnest sample ($N = 12$ UCs). Our novel simple approach allowed us to extract the 3D band dispersion without resorting to the controversial NFEA.

4.3.2 Validity of the NFEA

We tried to fit the dispersion data using the NFEA for the electron in the excited state, with two adjustable parameters: the photoelectron effective mass and the crystal inner potential. We have already mentioned the fact that NFEA has difficulties to describe our observed dispersions since these
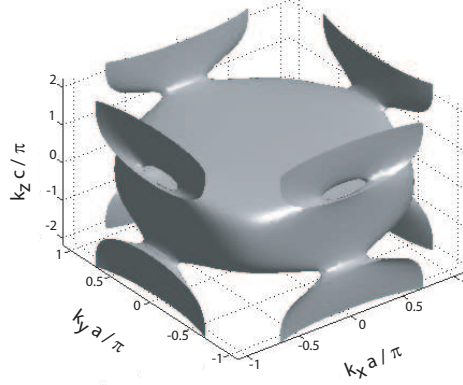
Figure 4.9: Reconstructed 3D Fermi surface using the band parameters from the Eq. 4.4: $t = 17$ meV, $t' = 4.42$ meV, $t'' = 149,6$ meV and $t''' = 5.1$ meV.

two adjustable parameters, describing the probing surface in the reciprocal space, strongly depend on the photon energy. The failure of the usual NFEA in trying to fit the experimental single photon energy data within the 3DTB approach, is due to the impossibility to retrieve the experimental probing path in reciprocal space. Indeed, adjusting the photoelectron effective mass and the inner potential, the projected path in the $E_b(k_{//})$-graph should cut the consecutive segments of the band dispersion close to their center. In practice, this path has a limiting slope which prevents such a cutting for reasonable values of the band parameters. In order to retrieve the experimental probing path, we need to increase the curvature of the "probing sphere". This can be achieved by considering a much lower effective mass along the in-plane direction. Thus we tried to solve the problem with a phenomenological anisotropic NFEA explained in the Appendix (section 6.4). The expression for the normal component k_z with the effective mass anisotropy becomes:

$$k_z = \sqrt{\frac{2m_c^*}{\hbar^2}(E_{PH} + |E_0| + E_b) - \mu k_{//}^2} - G_z. \qquad (4.6)$$

The reciprocal lattice vector G_z is defined as:

$$G_z \approx \sqrt{\frac{2m^*(E_{PH} + |E_0| + E_b)}{\hbar^2}}, \qquad (4.7)$$

where E_{PH} is the photon energy, E_0 is the inner potential and E_b is the binding energy. Including an anisotropy factor in the effective mass, the probing surface in momentum space for single photon energy ARPES experiments is correctly described. For example, considering the sample L288 of 12 UCs, by including an anisotropy factor $\mu = m_c^*/m_{ab}^* = 3.25$ for the 67 eV data, with an inner potential $|E_0| = 8.55$ eV (excluding the work function), we find the correct projection of the probing path. In order to illustrate our analysis, a numerical simulation of the photoemission intensity (see Fig. 4.10) is carried out within the anisotropic NFEA using the tight-binding (TB) parameters found with the discrete fit. We include the effective resolution by assuming a fixed Gaussian spread $\Sigma = 0.01\text{Å}^{-1}$ for the k_z vector:

$$I(k_{//}, E_b) = I_0 \frac{1}{\sqrt{2\pi\Sigma^2}} \sum_n \exp(-\frac{(k_z - k_z^{(n)})^2}{2\Sigma^2}). \qquad (4.8)$$

Eq. 4.8 simply represents the intensity contributions from the discrete dispersion branches at each given point $(k_{//}, E_b)$. The different quantized branches are probed by the broad distributed wavevector centered at the k_z value given by Eq. 4.6, the anisotropic NFEA. Consequently, the actual resolution of our experiment is a combination of the intrinsic instrumental resolution and the strength of the 3D dispersion that determines the separation between consecutive energy levels.
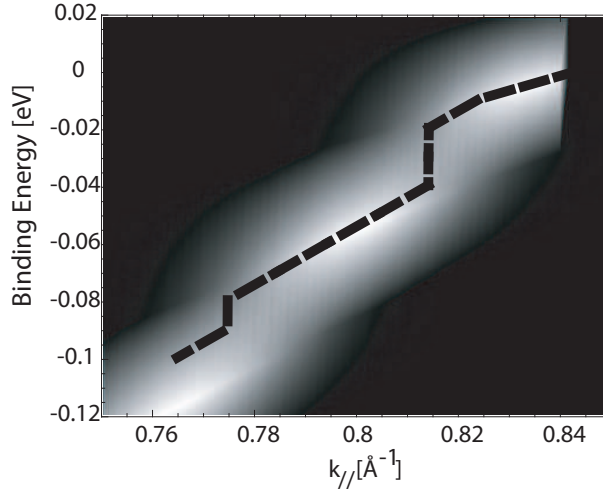
Figure 4.10: Simulation of ARPES experiment. The dotted line represents experimental data.

4.3.3 Band parameters evolution

The band dispersion is varying with the film thickness. The films show different band structures according with their number of UCs. Thick films of more than 40 UCs show a completely 2D dispersion. In Fig. 4.11 the 2D fit for the data collected along the $\Gamma - M$ direction of a sample of 58 UCs is shown. Notice that the data taken at different photon energies merge all on the same dispersion curve. The values of the parameters t and $r = t'/t$ are in good agreement with the ones previously obtained for relaxed LSCO [2].

Fig. 4.12 plots the ratio R between the sum of the out-of-plane hopping terms, $t'' + t'''$, and the sum of the in-plane hopping terms, $t + t'$, as a function of the total number of UCs N. This is a qualitative indicator pointing out the predominant dimensionality of the electronic band dispersion. Like for the behavior of the FWHM (Fig. 4.5) explained in section 4.2.1, the same critical thickness of $N^* = 18$ UCs is also encountered in this case. It denotes a crossover from 2D to 3D character of the band dispersion. Films thinner
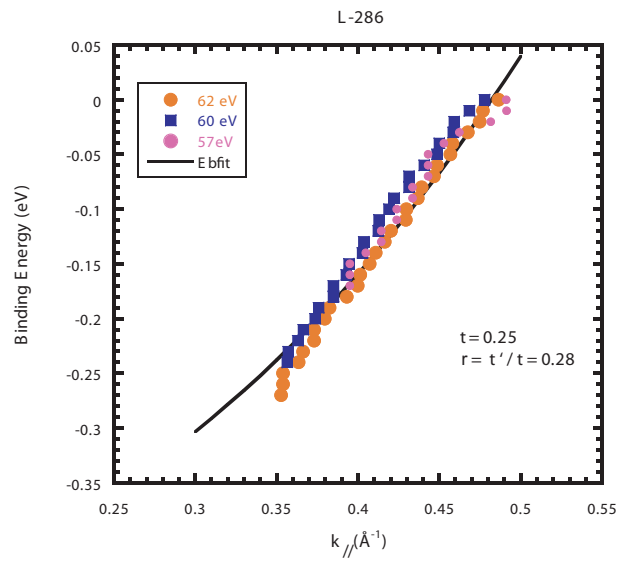
Figure 4.11: 2DTB fit for a film thicker than 30 UCs.
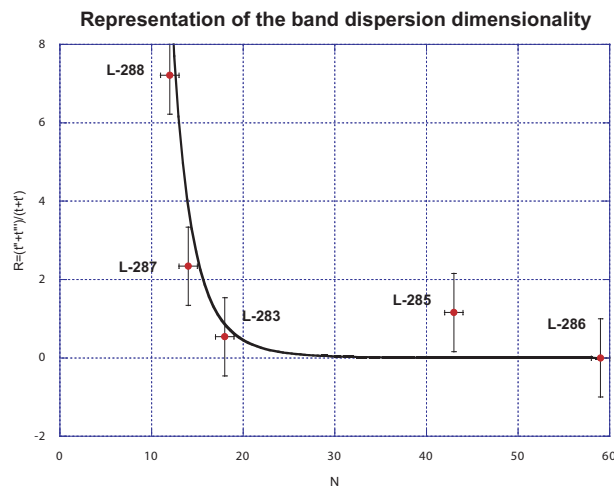
Figure 4.12: Ratio between the sum of the out-of-plane hopping terms and the sum of the in-plane hopping terms as a function of the total number of UCs. The black line is a guide for the eyes.

than 18 UCs have a strong increase in the out-of-plane terms, while films thicker than 18 UCs are rather 2D.

4.4   Films under tensile strain without interstitial oxygen

In order to discriminate between the effect of oxygen trapping and tensile strain, we adjusted the growing parameters in order to produce films without O_2 excess. In addition, we could measure directly the effect of the in-plane strain on the shrinking of the c-axis. The growing conditions were changed in such a way to avoid O_2 trapping during the deposition. This could be accomplished increasing the target-substrate distance or/and decreasing the laser power. Indeed, the oxygen trapping is favored when the target-substrate distance is reduced means the substrate is closer to the part of the PLD plume near the target, which is richer in atomic O.

We analyze the electronic properties of a series of films with different thicknesses: 10, 14, 16, 20, 22 UCs.
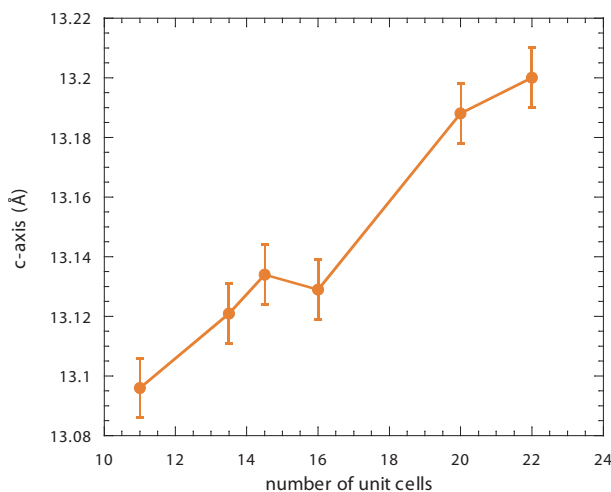
Figure 4.13: Plot of the c-axis as a function of the number of UCs for oxygen free samples.

We see that all the grown films are under tensile strain showing a shrinking

of the c-axis value. The c-axis measurements are reported in the graph in Fig. 4.13. From the value of the c-axis we can derive the out-of-plane strain and consequently the in-plane strain using the following relation:

$$\varepsilon_{//} = \frac{-2\nu}{1-\nu}\varepsilon_{\perp},$$
(4.9)

where ν represents the Poisson ratio and, in the case of LSCO, its numerical value amounts to 0.3 [45]. We can plot at this stage the in-plain strain as a function of the thickness (Fig. 4.14). It is possible to fit the strain profile using the formula in Eq. 4.2 obtained from the model referred in Ref. [47].
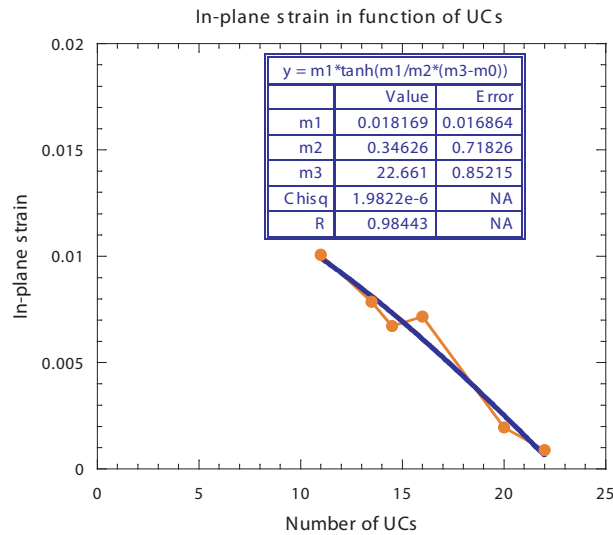
Figure 4.14: Plot of the in-plane strain $\varepsilon_{//}$ versus the number of UCs.

The plot of the FWHM as a function of the thickness (Fig. 4.15) shows a behavior that is similar to the one of samples with trapped O_2.
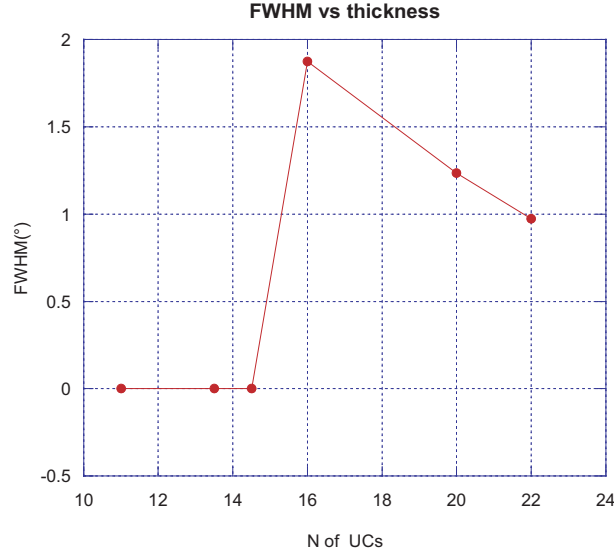
Figure 4.15: Plot of the broad contribution of the FWHM as a function of the number of UCs.

4.4.1 ARPES results

We report here the main ARPES results on films without trapped O_2. We observed, even in this case, wavevector quantization along k_z and we fitted the band dispersion using the formula in the Eq. 4.4. We show one example in Fig. 4.16 and the corresponding reconstructed FS is shown in the left panel of Fig. 4.17. In the right panel of Fig. 4.17 we show the cutting of the FS with the "probing surface" at 57 eV under two different perspective views. The upper part of the FS has been suppressed for the sake of clarity. The parameters $m^* = 1.16 \ m_e$, $E_0 = 8.7$ eV, $\mu = 5$, determining the good projection of the probing path in the NFEA are also specified in the figure. We can notice that their values are comparable to the ones obtained previously for samples with interstitial oxygen. Another sample (L300) deserves to be mentioned for its peculiar dispersion. We observe indeed a "reverse" dispersion, going from small k to higher k values, increasing the binding en-
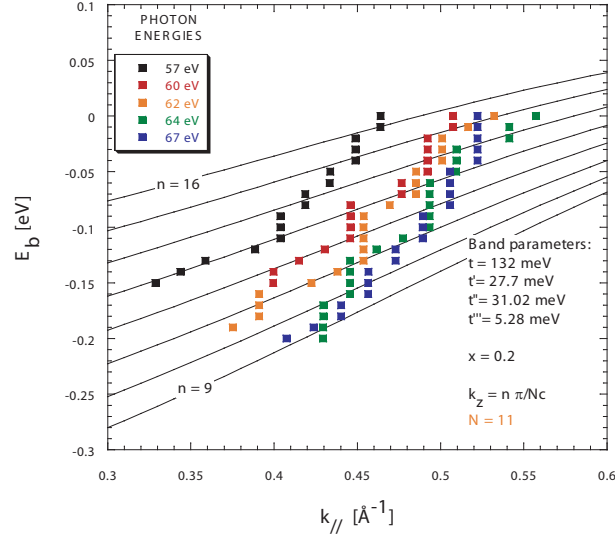
Figure 4.16: Dispersion along PHI=10° direction obtained at different photon energies and fits with the discrete 3DTB model for quantum levels indexed by n for a film with thickness of 11 UCs.

ergy. In Fig. 4.18 we show the dispersion along $\Gamma - X$: the clearer peak is in the 2nd Brillouin zone (BZ), however one can notice the presence of a second dispersion in the 1st BZ meaning a probing sphere entering in the 2nd BZ and coming out form the first one. Working with 3D dispersion in layered oxides we can encounter very exotic situations. The dispersion and the Fermi contours can display very tortuous shapes, varying from one photon energy to another, depending on the local shape of the FS at its intersection with the probing sphere.

We conclude that in-plane tensile strain affects marginally the overlap between the orbitals responsible for the in-plane hopping terms and triggers the out-of-plane dispersion, presumably due to a significant rearrangement of out-of-plane atomic orbitals. This effect is not surprisingly at all considering the huge c-axis contraction of the UC in samples free from interstitial oxygen. In general, 3D dispersion is enhanced as the distance between the Cu and
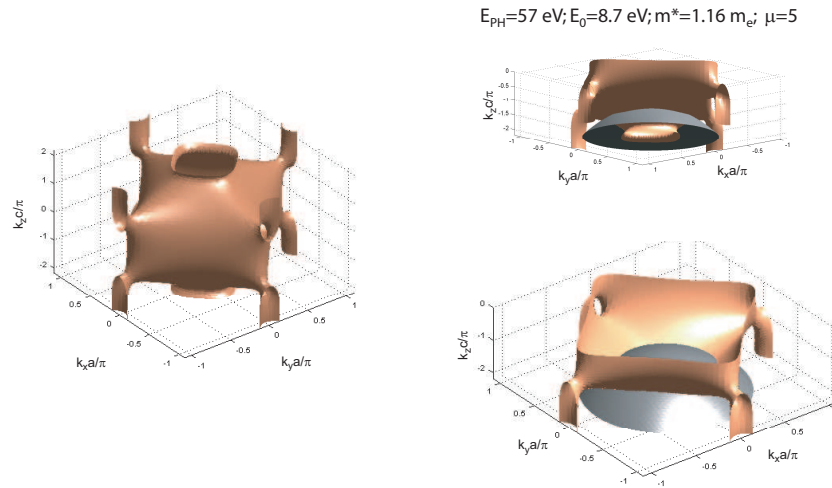
Figure 4.17: FS reconstructed using the parameters obtained in the fit in Fig. 4.16 showing the probing sphere cut.
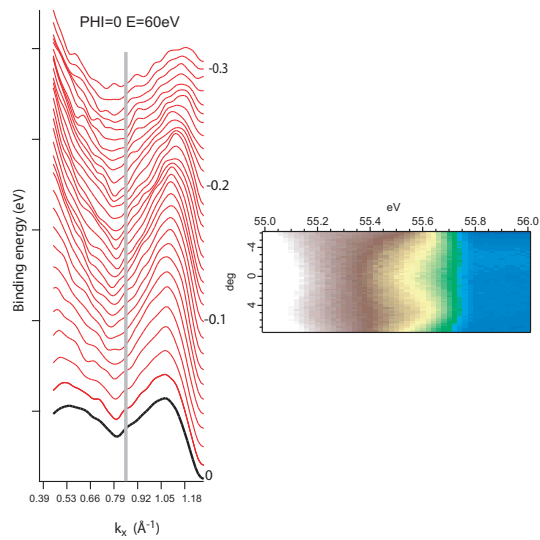
Figure 4.18: On the left, MDCs along $\Gamma - X$ direction of a sample of 14 UCs. The grey line represents the edge of the 1st BZ. On the right, the corresponding ARPES intensity map.

the apical oxygen is reduced.

4.4.2 Band parameters evolution: comparison with films with O_2.

We plot in Fig. 4.19 the parameters obtained from the discrete 3DTB fit as a function of the number of UCs as we did for the samples with interstitial oxygen (Fig. 4.12). Surprisingly, our 3D indicator (R), after showing a considerable value ($R \simeq 3$) at 22 UCs, comparable to thinner oxygenated samples, jumps down to a weaker 3-dimensionality of the order of 0.2, for very thin films. This result is in agreement with our previous experiment with O_2-free samples [20]. The expected shrinking of the c-axis of these films, in
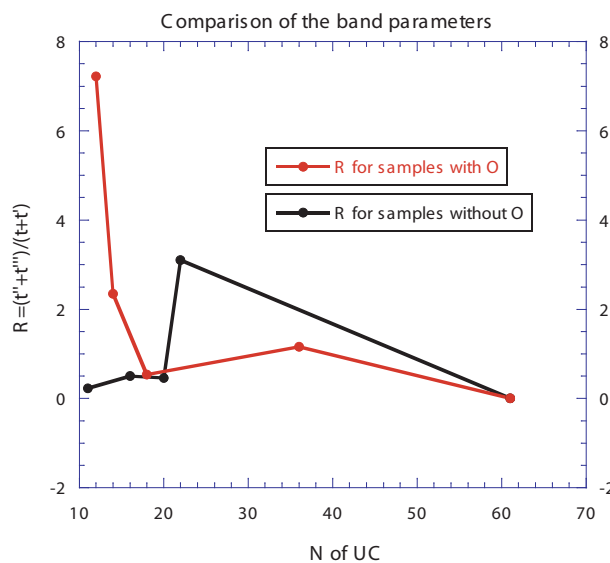
Figure 4.19: Comparison of the ratios R, between samples grown with and without interstitial oxygen.

agreement with the theory of elasticity, excludes the presence of interstitial oxygen. Then, it becomes clear that the dimensional crossover is triggered by the in-plane tensile strain. Therefore oxygen trapping is not essential for this

evolution of the electronic band structure with the film thickness. However the huge values of the out-of-plane hopping terms in the O_2-rich samples show that interstitial oxygen is amplifying the z-dispersion channel.

In conclusion, for O_2-free samples, the out-of-plane nearest neighbor hopping integral involves the La cations in the reservoir and relies on the hybridization of the apical oxygen p_z and the Cu $3d_{z^2-1}$ orbitals as already discussed in the Ref. [20]. From our point of view, the presence of interstitial oxygen, located in between the two La-O planes, modifies the local orbitals in such a way that it adds a new hopping channel or it amplifies the existing one. However we cannot exclude other mechanisms, since the distortion of the UC is considerable.

Chapter 5

Growth and electronic properties of $\mathrm{Bi_2Sr_{2-x}La_xCuO_6}$

In this chapter the main characteristics of the Bi-2201 compound doped with La are studied. All the Bi-2201 films were grown at the EPFL with "home-made" targets and all the ARPES measurements were performed at the EPFL.

5.1 Introduction

This compound is the lowest n-compound ($n = 1$) in the $\mathrm{Bi_2Sr_2Ca_{n-1}Cu_nO_{2n+4}}$ family. Its structure, shown in Fig. 5.1, is quite simple, as it contains only a single $\mathrm{CuO_2}$ plane. The substitution of $\mathrm{Sr^{2+}}$ by $\mathrm{La^{3+}}$ reduces the hole doping and reduces the out-of-plane disorder, thus increasing the critical temperature T_c [10, 41, 25]. Undoped samples are indeed in an overdoped regime. The hole concentration of Bi-2201 can be widely controlled, more than the parent Bi-2212: it can be easily varied from heavily overdoped conditions to underdoped ones. The T_c of this compound (about 30 K at optimal doping)
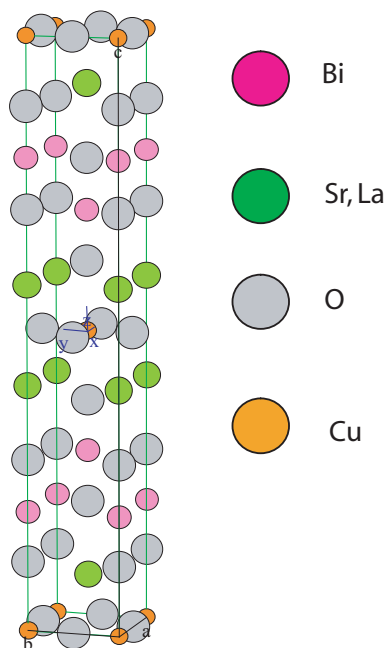
Figure 5.1: UC of Bi-2201.

is the lowest of the Bi-family. This is maybe the main reason why it is the less studied in comparison with the well-known parent compounds Bi-2212 and Bi-2223. However, NMR [63] and electrical resistivity experiments [4] estimate the pseudogap temperature in Bi-2201 to be similar to the one of Bi-2212, despite its smaller T_c. Therefore we should gain an important insight into the relationship between the pseudogap and the superconducting gap by directly performing ARPES measurements on Bi-2201.

5.2 The sample preparation

Stoichiometric $Bi_2Sr_{2-x}La_xCuO_6$ (x = 0, 0.2, 0.3) and nonstoichiometric $Bi_{2.2}Sr_{2-x}La_xCuO_6$ (x = 0.05, 0.1, 0.2, 0.3) targets are made by firing appropriate amounts of $SrCO_3$, La_2O_3, CuO, and Bi_2O_3 in an Al_2O_3 crucible.

The reaction mixtures were sintered in pellet form at 800 - 810 °C with frequent regrinding. The target composition was analyzed by powder diffraction, showing only the Bi-2201 phase. Thin films are deposited on (100) STO substrates at 3 Hz repetition rate. All the films have a thickness of about 4000 Å in order to have complete relaxation. The films are grown under different conditions; the oxygen pressure, the substrate-target distance, and the temperature of the substrate are varied. The post-annealing condition are also tuned as it will be explained in the next section.

5.3   The effect of the annealing in 30% La doped Bi-2201 samples

The post-annealing treatment seems to be crucial for the structural and superconducting properties of La-doped Bi-2201 samples [15]. We investigated in particular the 30% La doped thin films. The as-grown samples (no post-annealing treatment) are not superconducting above 4 K. Annealing in-situ or ex-situ in Ar or O_2 atmospheres for short periods of 1 hour at 700 °C can change the sample properties and improve the superconductivity.

5.3.1   X-ray analysis

The O_2 annealing appears to improve the structural quality of the films, meaning that the disorder present in the as-grown films is reduced. The $\theta - 2\theta$ analysis, shown in Fig. 5.2, indicates an enhanced crystal coherence along the c-axis: 00l peaks have not only higher intensities but also a better resolution of the Cu K_α doublet. The doublet is also shifted meaning a higher c-axis value.
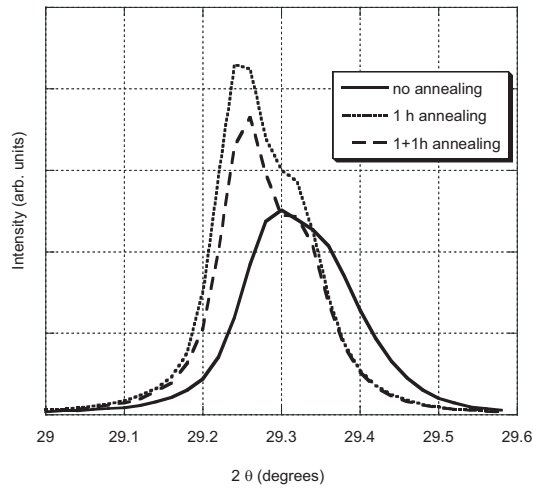
Figure 5.2: Evolution of the (008) Bragg reflection of a Bi-2201 films after annealing in oxygen.
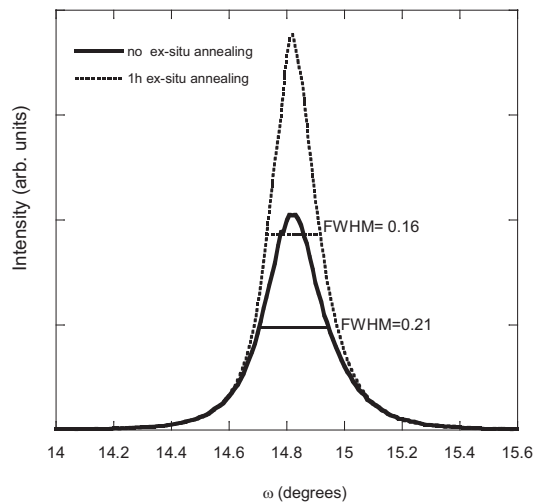
Figure 5.3: RC evolution with O_2 annealing. The values of FWHM are obtained using a Lorentzian fit.

We observed moreover that the ex-situ annealing in oxygen reduces the FWHM of the RC by 30%, which indicates an improved in-plane crystal coherence (Fig. 5.3). However, the extended repetition of this annealing procedure is detrimental to the quality of the films: after the third annealing we
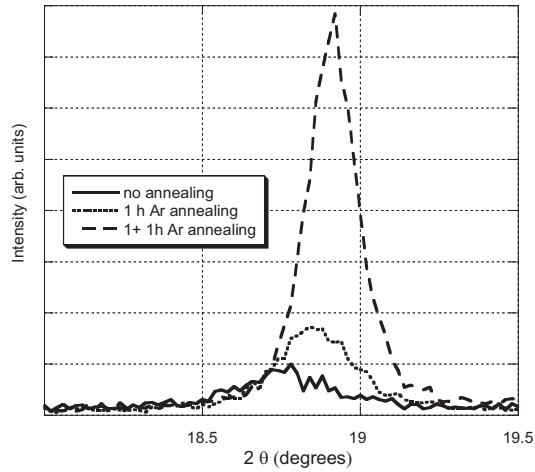
Figure 5.4: Variation of the extra phase peak with Ar exposure.

observe the nucleation of a new phase. This behavior is drastically enhanced by Ar annealing: films annealed in an Ar atmosphere show phase separation already after the first annealing. The amount of this extra phase is strongly increased with further Ar annealing as it is shown in Fig. 5.4. The peak of the extra phase is increasing consistently after repeated Ar exposure. In order to identify the impurity phase revealed by the presence of extra peaks in the $\theta - 2\theta$ diffractogram (indicated by arrows in the upper part of Fig. 5.5), we first tried to index those peaks using the tabulated XRD patterns of all possible compounds containing Bi, Sr, La, Cu and O. No matching was found for any of them or their mixtures. Furthermore, we noticed that these extra peaks can all be indexed as successive diffraction orders of a single lattice distance (9.5 Å). This implies the presence of a single orientation for the impurity phase, presumably due to the epitaxial growth within the Bi-2201 matrix. This epitaxial impurity must have a small in-plane lattice mismatch with respect to the matrix, and present a weak deviation from the global composition. On the other hand, the closest structures found in the
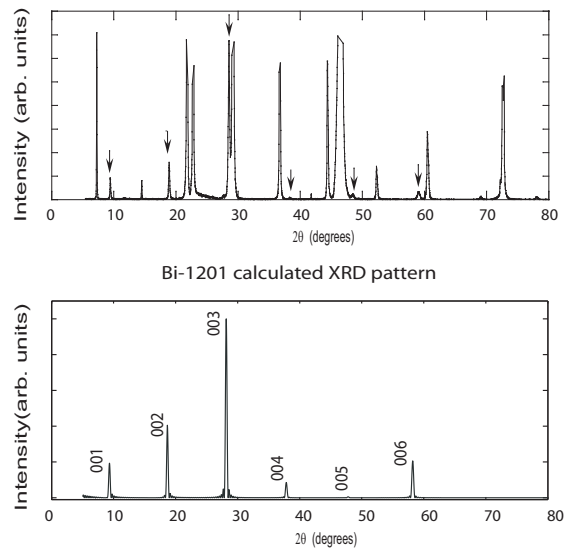
Figure 5.5: Comparison of the $\theta - 2\theta$ diffractograms (1201 peaks are indicated by arrows) and the calculated pattern for the Bi-1201 phase.
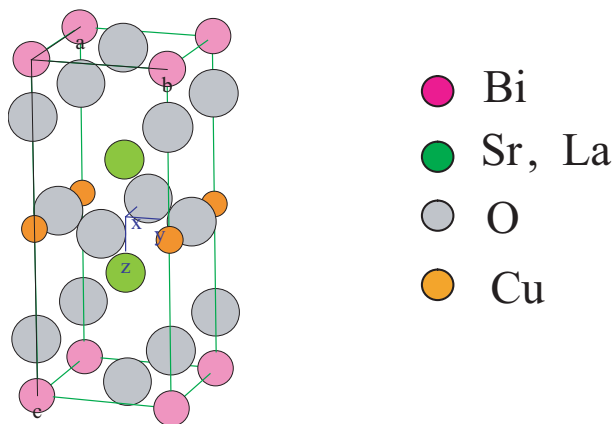
Figure 5.6: Bi-1201 UC structure.

literature with a c-axis of about 9.5 Å are $HgBa_2CuO_{4+\delta}$ and $TlBa_2CuO_{5-\delta}$, i.e. the Hg-1201 and Tl-1201 structures. By analogy we assumed that the impurity phase was $Bi(Sr, La)_2CuO_5$ (Bi-1201) [64, 3]. This is a Bi-deficient phase; the volatility of Bi is well-known, especially at high temperature [37]. The Bi deficiency is then created in the sample and consequently the forma-

Table 5.1:
Fractional coordinates of Bi-1201

	x	y	z
Bi	0	0	0
Sr(10%)-La(90%)	0.5	0.5	0.33
Cu	0	0	0.5
O(1)	0	0.5	0.5
O(2)	0	0	0.17
O(3)	0.5	0.5	0

tion of the Bi-1201 phase is accomplished. It is important to say in addition that the starting target was stoichiometric (no Bi deficiency). Atomic ratios of as-grown films were measured by Rutherford backscattering (RBS), and the results showed that the stoichiometry 2:2:0:1 of the target is transferred to the films. Using the standard diffraction theory, we calculated the intensity pattern of a Bi-1201 (00l) oriented crystal, varying the atomic relative positions and the La content (Fig. 5.5).

Table 5.1 indicates the relative atomic positions obtained in the XRD pattern simulation of Bi-1201, by fitting the measured pattern, and in Fig. 5.6 the UC of Bi-1201 is represented. Surprisingly, it turns out that the Sr site is mostly occupied by the La atoms. This can explain the lowering of the T_c in films which show the presence of the 1201 phase, as it will be clarified later on.

5.3.2   Photoemission: core level measurements

We performed photoemission core level spectroscopy measurements at the SRC, on the 6 m toroidal grating monochromator beamline. We measured two different kinds of Bi-2201 thin films: without post-annealing treatment and films annealed in oxygen at 700 °C in 1 atm of O_2 for 1 hour. We
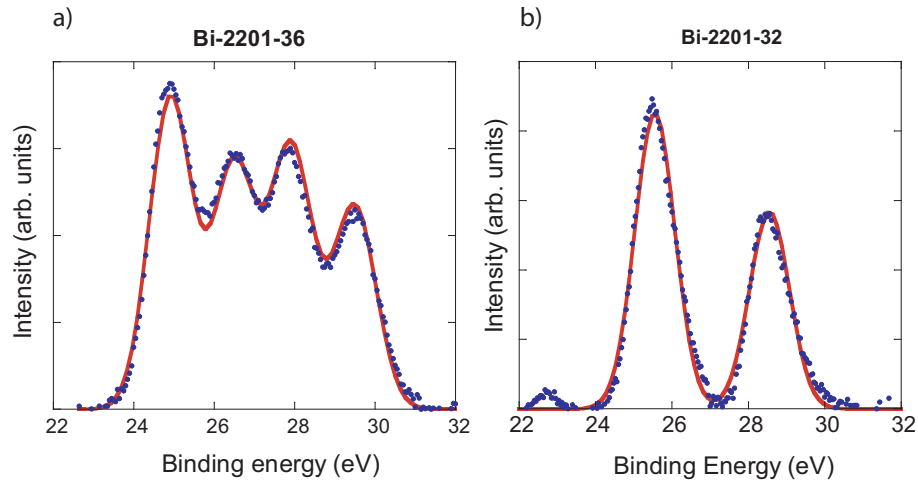
Figure 5.7: Bi-5d doublet for a) sample annealed for 1 h in oxygen and b) sample not annealed.
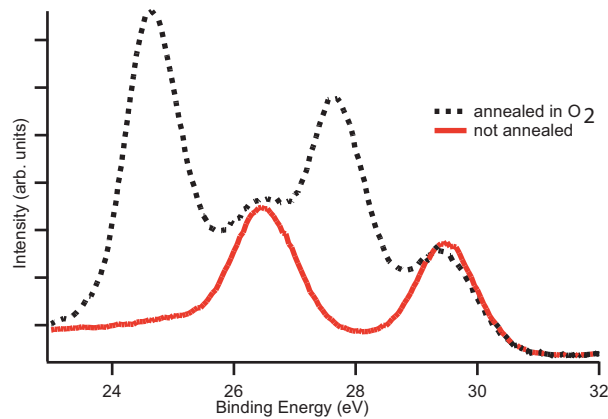
Figure 5.8: Bi-5d core levels acquired at $h\nu = 60$ eV.

analyzed in particular the Bi-5d doublets: $5d_{3/2}$ at about 25 eV and $5d_{5/2}$ at about 28 eV, accessible at relatively low photon energies (60 eV).

The photoelectrons were collected and analyzed by a cylindrical mirror analyzer (CMA). The axis of the analyzer was inclined at an angle of $45°$ with respect to the sample normal. We measured the Bi-5d doublet at a photon energy of 60 eV. This doublet seems to be the most affected by the

annealing. We believe that the Bi-O planes are the planes where the oxygen atoms can install interstitially and where their mobility is more pronounced. That is the reason why we observed different Bi doublet position for films annealed in oxygen (Fig. 5.7, 5.8). The new doublet at 25.2 and 28.2 eV is in good agreement with the values reported in literature for the Bi-2212 compound, while the doublet position for the as-grown sample indicates a higher oxidation state. In general, annealing in 1 atm of oxygen conserves the excess oxygen in the sample. Therefore, an effective reduction of Bi core levels after O_2 annealing implies an internal atomic rearrangement. The La^{+3} ions, present in the structure, can be responsible for the reduction of Bi. If La^{+3} cations, initially trapped in interstitial sites, migrate to the Sr sites during the annealing, they will add extra electrons in the Bi layer environment. This picture is in agreement with the fact, explained in the following section, that sample not annealed are not superconducting.

5.3.3   The T_c: AC susceptibility and resistivity measurements

We analyzed the evolution of the T_c with respect to the annealing treatment by measuring the film magnetization and the resistance as a function of the temperature. As we already said, the as-grown samples are not superconducting. However a short in-situ annealing of 30 minutes in 1 atm of O_2 at 700 °C is enough to induce superconductivity, which can be further improved by consequently ex-situ annealing.

We studied the evolution of the T_c with the annealing treatment by measuring the film magnetization as a function of the temperature by using an AC susceptometer. In Fig. 5.9 a) we plot the real part of the magnetization as a function of the temperature. We observe an increase in both the T_c

and the intensity of the diamagnetic signal after double annealing in oxygen. However, further annealing in oxygen deteriorates superconductivity, in accordance with the observed structural evolution. In case of Ar annealing of the as-grown samples, we can induce superconductivity as in the case of O_2 annealing, but superconductivity is lost after the second annealing. Nevertheless, superconductivity is fully restored by subsequent annealing in oxygen. Finally, the best results are obtained by combining both types of annealing as follows: a post-annealing in oxygen followed by an argon annealing (see Fig. 5.9b)). The T_c values measured by AC susceptibility on our films are significantly lower than the values published for equally doped thin films [36] measured by resistivity techniques. Resistivity measurements show systematically higher T_c values than AC susceptibility due to the sample inhomogeneity, especially in thin films. Indeed, we also have performed resistivity measurements on films which show best susceptibility transition and we found large transitions typical of inhomogeneous samples with $T_{c,onset}$ = 25 - 28 K, which is in good agreement with the value found in literature for analogous films. Fig. 5.10 shows the normalized resistance measurements of a film annealed in O_2 and of the same film annealed in Ar for 1 hour. The quality of the transition and the T_c are slightly better performing both types of annealing.

In conclusion, the picture emerging from the aforementioned results is that the annealing in O_2 favors La ordering within the structure, while Ar annealing removes the excess oxygen by bringing the sample to the desired hole-doping region: T_c is consequently enhanced. Further Ar annealing removes additional oxygen, making the sample unstable again with respect to the La-Sr substitution. Remarkably, this effect is reversible, since a new annealing in oxygen restores superconductivity. The charge redistribution,
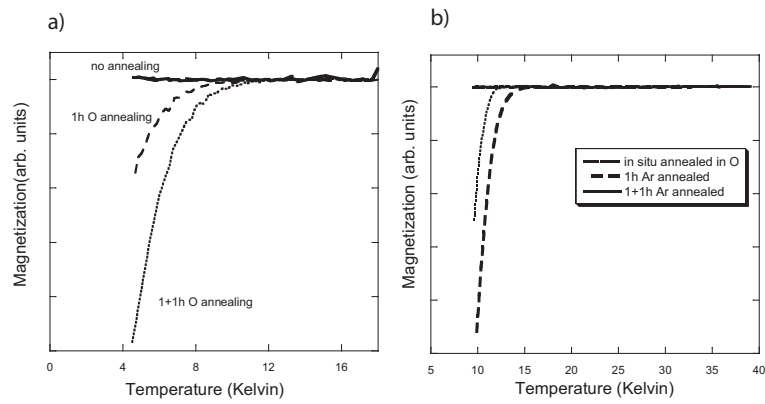
Figure 5.9: Real part of the magnetization of a) samples repeatedly annealed in O_2 and b) sample annealed in Ar.
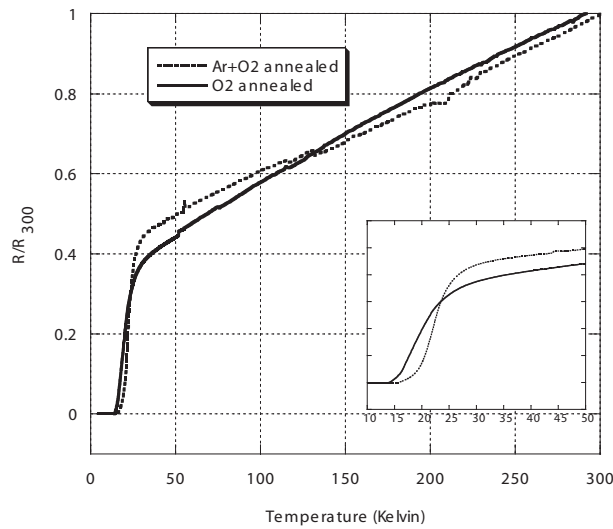
Figure 5.10: Normalized resistance versus temperature of a film annealed in O_2 before and after Ar annealing.

associated with the first O_2 annealing, is revealed in core-level measurements (XPS) as an effective reduction of the Bi, pointing out the role of competing La and Bi electronegativities. Another effect of further Ar annealing is the inducing of phase separation of the Bi-deficient homologous compound Bi-1201, presumably due to the high Bi volatility.

5.4 The intergrowth presence

The growing conditions are crucial in determining the final quality of the films. It is fundamental to investigate the structural properties of the samples in order to exclude the presence of subtle defects, harder to detect, like random intergrowth. For this reason, it is essential to perform a subtle X-ray investigation in order to enlighten these defects, as it will be explained in the next sections.

5.4.1 Random intergrowth model

Random intercalates are quite common in layer materials. Cuprates with a characteristic perovskite structure like BSCCO constitutes a good example of intergrowth formation. Namely these materials tend to form polytypes, since the formation enthalpy of homologous compounds differ only slightly from one another. Such intergrowth can be achieved if, for instance, $CaCu_2O_y$ layers of Bi-2212 or $Ca_2Cu_3O_y$ layers of Bi-2223 structures are substituted by CuO_y layers of the Bi-2201 structure [51]. In addition, as we already said in the chapter 2, PLD is an out-of-equilibrium process, which favors the irreversible formation of otherwise metastable intercalates. We surprisingly encountered a new type of intergrowth (IG) in Bi-2201 films, despite the absence of Ca. This polytype is the one we identified previously as a Bi-deficient phase, Bi-1201. The presence of La favors the Bi-1201 formation mostly as a c-axis oriented aggregates, like phase separation (PS). This appears as a "visible" defect, showing extra peaks in the XRD spectrum. IGs, on the contrary, are "hidden" defects that can be revealed only by a more subtle diffraction analysis. The presence of these polytypes of Bi-1201 evidences a global Bi deficiency in the films. Using PLD, an out-of-equilibrium technique, the sen-

sitivity to Bi loss is enhanced. PLD can be viewed as a repeated quenching process. Indeed, after each laser pulse of approximately 20 ns, the adiabatic expansion of the high-energy plasma supplies the growing film on the heated substrate with a colossal amount of kinetic energy, in addition to the latent heat liberated by the condensation process itself. The latter contributes to the surface mobility of the present species, and produces a short-time annealing of the underlying atomic layer. This external heating enhances the effective substrate temperature for about 1 μs, after which the film stays at the nominal temperature until the next laser pulse, i.e. 300 ms later. This can cause local composition fluctuation, namely Bi deficiency, producing a Bi-poor oriented polytype that can be trapped in the Bi-2201 matrix as a stacking fault. The unreacted Bi is easily removed by the continuous O_2 flow in the chamber during the deposition. The basic assumptions of our model are minimal, in the sense that we aim to investigate only two basic features of the intergrowth formation: the displacement distribution $P_t(z)$ of the UCs along the c-axis and the average in-plane two-point correlation function of the displacements $g(x) = < g_t(x) >$, where $g_t(x)$ is the correlation function on a given layer indexed by t. The minimal approach is justified by the fact that only the Fourier transforms of these two quantities have a direct impact on the standard XRD patterns of thin films.

The model is described in detail in Ref. [5]; the displacement distribution along z is explicitly described in the Appendix and here we investigate elaborately the in-plane disorder, i.e. the in-plane displacement distribution correlation function. We assume a layer-by-layer growth mechanism where 2D islands are formed and grown in the plane. Before the next layer is formed, complete coalescence is achieved. In order to investigate the displacement
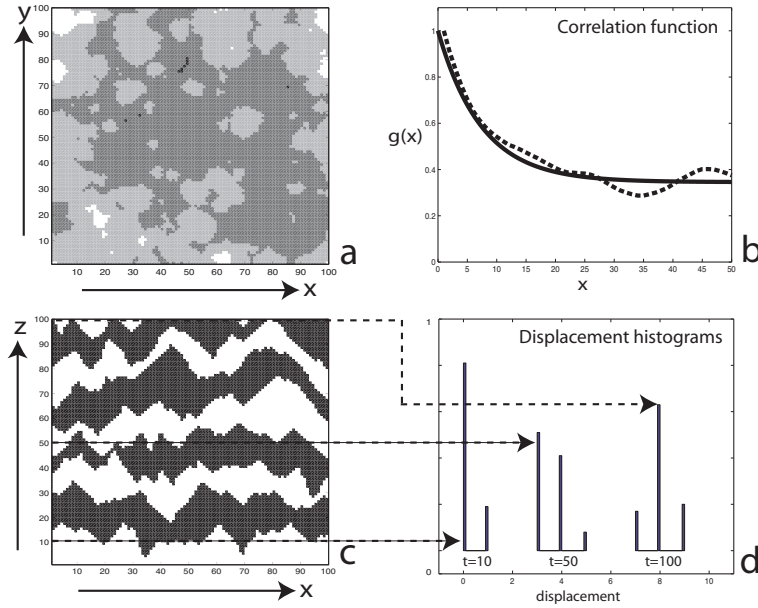
Figure 5.11: Numerical simulation: a) Top view of the last layer, b) in-plane correlation function and its fit (solid line) using Eq. 5.4, c) film cross section ((x, z)-plane), d) displacement histograms for layer numbers 10, 50 and 100.

distribution along the growth direction (z-axis), we use a mean-field (MF) approach. This is explained in the Appendix in chapter 6.

Although the layer-by-layer growth is a 2D process, within the MF approach we can map the system on an effective 1D system (row-by-row) by integrating over one in-plane degree of freedom. While the MF approach is well adapted for a description of the z-axis sequencing and correlations, it masks all information about the in-plane spatial correlations. In order to investigate the in-plane disorder, we implement a numerical simulation of the complete 2D model. Fig. 5.11 shows the numerical simulation of a film being 100 layer thick according to the model described in the Appendix. Fig. 5.11 a) is a map of equally displaced domains on a given layer (top view). Fig. 5.11 b) is the in-plane two-point correlation function averaged over the top layer. Fig. 5.11 c) is a vertical cross section of the film, in which

different displacement domains are successively colored in black and white. Histograms in Fig. 5.11 d) are computed at three different stages of film formation. One can already notice from Fig. 5.11 a) the in-plane clustering of equally displaced domains. The in-plane two-point correlation function $g(x)$ plotted in Fig. 5.11 b), shows a rapid exponential drop followed by a constant asymptotic behavior for larger distances.

Let us denote the short-range correlation function as $g_1(x)$: it is the probability for two cells, within a given layer and at a distance $|x|$ away from each other, to belong to the same displacement domain, i.e. with no steps in between. The general form for $g_1(x)$ reads as follows:

$$g_1(x) = e^{-\frac{|x|}{\xi}}. \tag{5.1}$$

Eq. 5.1 contains a characteristic decay distance, ξ, corresponding to the average domain linear size. This characteristic distance depends not only on the step concentration, denoted by S, but also on the in-plane step distribution characterizing the cluster's structure. While the value of ξ cannot be computed within the MF approach, a lower bound can be found, corresponding to the homogeneous step distribution situation ($U = 0$):

$$g_1(x) = (1 - S)^{\frac{|x|}{a}} = e^{-\frac{|x|}{\xi}} \implies \xi_{min} = \frac{a}{\ln(\frac{1}{1-S})}, \tag{5.2}$$

where a is the in-plane lattice constant.

The evaluation of the space-independent correlation g_0 is given by:

$$g_0 = \frac{1}{N} \sum_{t=1}^{N} \int_{tc_0}^{tc_1} [P_t(z)]^2 dz = \frac{1}{N} \sum_{t=1}^{N} \sum_{n=0}^{t} \left[\binom{t}{n} c^n (1 - c)^{t-n} \right]^2. \tag{5.3}$$

In Eq. 5.3, $[P_t(z)]^2$ is the probability of finding two cells, within the layer t, having the same z-axis position (i.e. containing the same number of intergrowth in their underlying columns) regardless of their particular mutual in-plane distance. The integration over $z \in [tc_0, tc_1]$ gives the total probability of finding two such cells for any possible displacement within the t layer. (c_0 and c_1 represent the lattice constant of the host and the guest lattice respectively.) g_0 is then obtained by averaging over the entire film (N layers) of the preceding quantity.

Finally, the total two-point in-plane correlation function for displacements is given by:

$$g(x) = g_1(x) + (1 - g_1(x))g_0 = g_0 + (1 - g_0)g_1(x) = g_0 + (1 - g_0)e^{-\frac{|x|}{\xi}}. \quad (5.4)$$

In conclusion, the exponential contribution to $g(x)$ is similar to the usual short-range correlation due to stacking faults in epitaxial films. The constant contribution is less usual and denotes a spatially independent (infinite-range) correlation. The expression of the correlation function explains the characteristic RC as it is shown in the next section.

5.4.2 X-ray diffraction anomalies

Analysis of XRD data in our films with the presence of IG shows different kind of defects. The most visible ones appear as extra peaks superimposed on the expected 2201 peaks, denoting a separated secondary phase already mentioned in the paragraph 5.2. However, in some cases secondary phases can be hidden and are therefore difficult to detect. Indeed, at a first glance, the $\theta - 2\theta$ analysis shows the presence of a (00l) oriented Bi-2201 phase. However, a more accurate analysis reveals non-monotonous deviations of the

Bragg peak position and anomalous intensity ratios of the peaks in the $\theta - 2\theta$ spectrum. The film containing intergrowth shows large oscillations in the c-axis parameter determined for each peak in the diffractogram (Fig. 5.13). In a film without intergrowth one should expect a normal linear dependence in a plot of the c-axis versus $\cos^2\theta / \sin\theta$. Moreover, if we compare the intensity ratios of a pure, single-phase sample with one with intergrowth, we observe radically different values (Fig. 5.12). We can also calculate the pattern for an intergrowth-free sample using tabulated fractional coordinates extracted from Ref. [54]. The more evident anomaly is nevertheless in the feature of the RC (Fig. 5.14). There are two contributions to the in-plane correlation function giving rise to the two components of the RC: one broader Lorentzian function associated with the standard in-plane correlation within finite-size coherent domains, and a very narrow one (FWHM equal to instrumental resolution) from the long-range contribution of equidisplaced domains, as it was explained in the previous section. Such features combined with oscillation of the FWHM of the peaks are unambiguous signatures of random intercalates.

The model described in Ref. [7] allows us to derive the concentration of IG and the difference in lattice constants between the guest and the host lattice. We used this model to fit the momentum deviation of the Bragg peaks as shown in Fig. 5.16. We identify two types of IG, both due to the intercalation of a Bi-1201 phase:

1. The c-axis of the guest phase is about 3.7 Å larger than the one of the host lattice (24.4 Å), hereafter "+3".

2. The c-axis of the guest phase is about 3.1 Å shorter than the host lattice, hereafter "-3".
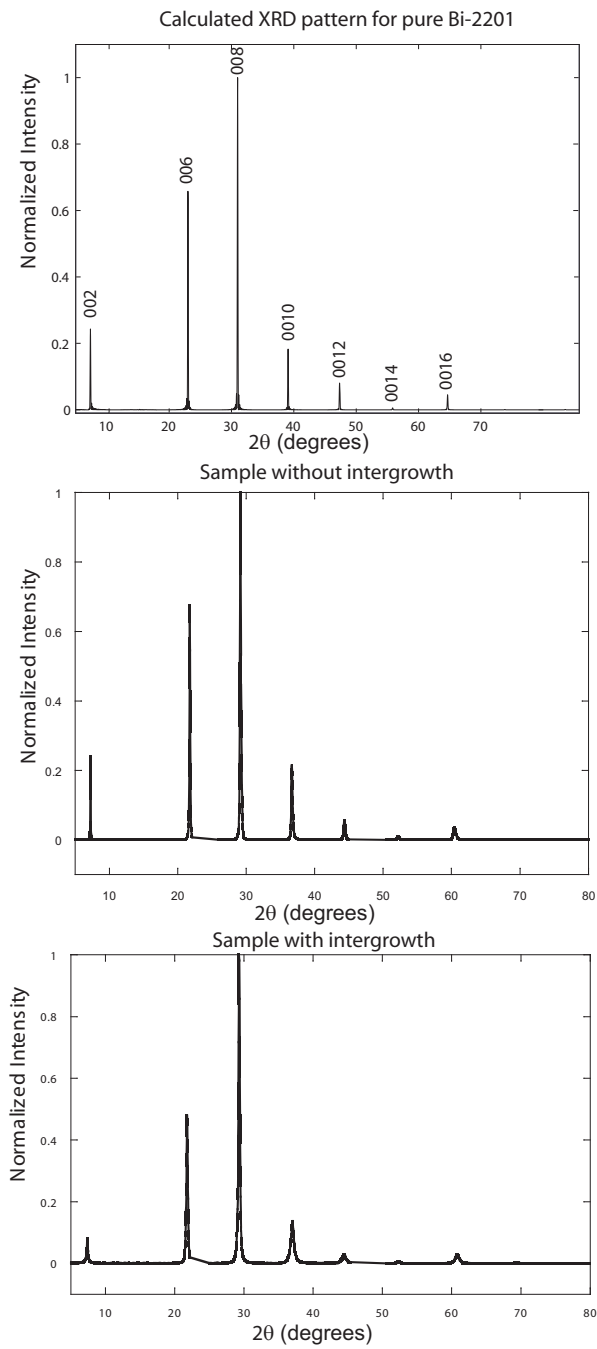
Figure 5.12: Diffraction pattern for a film with and without IG compared with a calculated XRD pattern for an undoped Bi-2201.
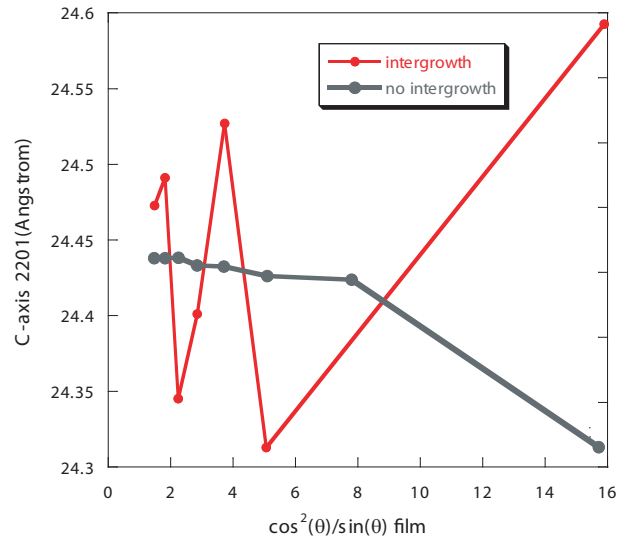
Figure 5.13: Comparison of the *c*-axis of a film with and without intergrowth. The *c*-axis oscillation is strongly pronounced for samples with IG.
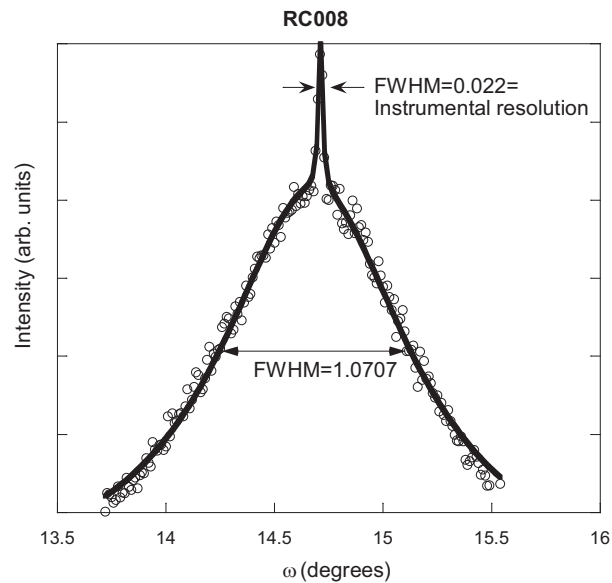
Figure 5.14: Typical RC of a film showing presence of IG. Two contributions are evidenced: a broader Lorentzian which corresponds to the exponential correlation within finite size coherent domains while the narrow peak comes from the space independent correlations.
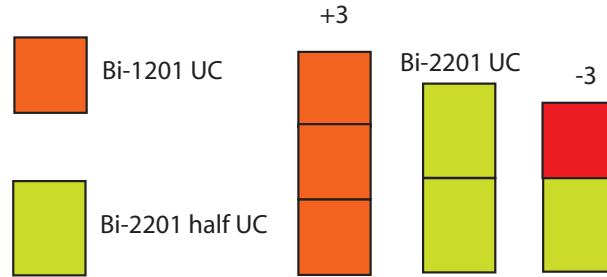
Figure 5.15: Schematic representation of the two kinds of IG discussed in the text: "+3" and "−3".

Namely, the c-axis of Bi-1201 is 9.45 Å. The presence of three consecutive UCs of this phase in the "+3" IG could explain the +3.7 Å difference in c-axis (Fig. 5.15). Similarly, "-3" IG, mainly observed in undoped samples, is formed by half a UC of Bi-2201 and the other half of one UC of Bi-1201 giving a total c-axis of 21.2 Å. The occurrence of IG depends on the La doping and on the growing conditions [16] as it will be explained in the next sections.

5.4.3 Undoped samples

The presence of Bi-1201 in the films, as IG or as a separated phase, denotes a global Bi deficiency. Since PLD is assumed to transfer the exact target stoichiometry to the vapor phase, the Bi loss must occur during the condensation process and/or during the post-annealing treatment.

In undoped samples we observe only the presence of "-3" IG and never the "+3" IG or phase separation. IG-free samples can be grown using small substrate-target distances (≤ 4 cm), low oxygen pressures, and high temperatures of the substrate. Post-annealing treatments of samples containing IG do not noticeably alter their as-grown structure.
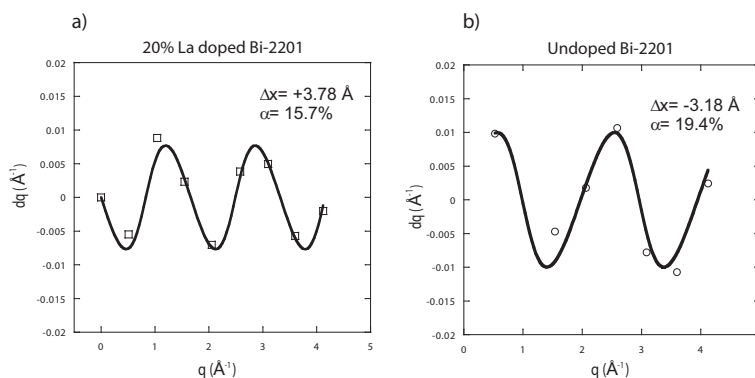
Figure 5.16: Momentum deviation for a) a 20% La-doped Bi-2201 film and b) an undoped one, fitted with the statistical model of Ref. [7].

5.4.4 La-doped samples

In contrast to what is observed for undoped samples, La-doped samples are highly sensitive to both growing conditions and post-annealing treatments. In general, under the same growing conditions, La-doped films contain more polytype defects and have a marked tendency to undergo phase separation in the form of oriented La-rich Bi-1201 aggregates, which seem to be the ultimate equilibrium configuration after annealing. In addition, in presence of La it is very difficult to achieve pure Bi-2201 single-phased films. The best conditions to obtain single-phased films are: low target-substrate distances, deposition temperatures of 610 - 620 °C, oxygen pressures $\leq$ 300 mTorr, post-annealing treatments in 1 atm of O_2 for maximum 1 hour. La^{3+} ions are essential to accomplish the charge balance in Bi-1201 [35], even favoring the formation of this phase, while they are largely unbalanced in the Bi-2201 structure. Furthermore, local chemical and elastic relaxation can be improved by La diffusion from Bi-2201 cells to neighboring Bi-1201 IG. The Bi-deficient polytype will then be more stable with La. Apart from the

local composition fluctuations, the nucleation of the Bi-deficient structure is now dominated by the charge balance mechanism related to the La presence. This explains why we observe Bi-1201 PS only in La-doped samples. During the annealing process, further rearrangements yield a phase-separated final configuration, where the Bi-1201 aggregates capture most of the La^{3+} ions. Such rearrangements need also some Bi mobility that seems to be triggered by the larger La diffusivity at the considered annealing temperatures. A last feature to be considered here, is the difference between the type of IG appearing in undoped and La-doped films. While the main defects in undoped films ("-3" IG) consist of diluted single Bi-1201 UCs, the so-called "+3" IG, formed by local piling-up of three consecutive Bi-1201 UCs, in the La-doped films, imply a higher density of defect nucleation during the growth as well as a good mobility of La^{3+} and Bi^{3+} ions within the host matrix. Thus, the mechanisms invoked for the evolution during the post-annealing are already active during the film formation and explain the PS observed in La heavily doped as-grown films. The absence of piling-up of just two Bi-1201 UCs is due to the higher cost in elastic energy of the resulting step in the Bi-2201 matrix: while the displacement step between a complete UC of Bi-2201 and a sequence "(half-2212)-(1201)" or "3×(1201)" are about -3 Å or +3 Å respectively, the difference with a sequence of "2×(1201)" would be of about -6 Å, a mismatch that makes this event statistically improbable.

5.4.5   Bi-compensated samples

We tried to compensate the Bi deficiency in the films, growing the films starting from a nonstoichiometric target. We use different La-doped targets ($x = 0.05, 0.1, 0.2, 0.3$) with Bi excess of 0.2 ($Bi_{2.2}Sr_{2-x}La_xCuO_6$). However, even reducing the La content to $x = 0.05$, XRD still reveals phase separation

of Bi-1201, underlying the fact that the Bi excess in the target is favoring rather than preventing the phase separation. Nevertheless, the excess Bi
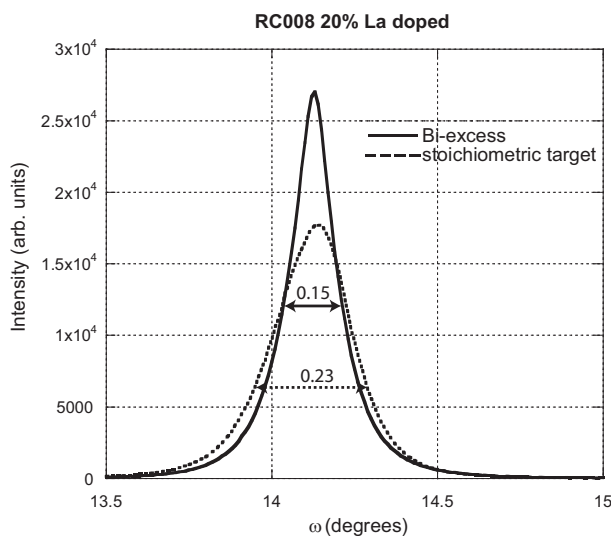
Figure 5.17: Comparison of the RCs around the (008) peak for a film produced by a stoichiometric and a Bi excess target.

contributes to improve the Bi-2201 phase: the in-plane crystallinity and the one along the c-axis are increased. In Fig. 5.17, the RC comparison shows that the FWHM is reduced by 53% in the Bi-compensated samples, implying an improved in-plane crystallinity. At the same time, $\theta - 2\theta$ XRD data show higher absolute intensities and the K_α doublet is well resolved denoting an improved structural coherence along the c-axis. Bi excess in the target reduces the disorder in Bi-2201 phase: comparatively, films made from a stoichiometric target contain more Bi deficiencies and consequently more defects than the ones made from Bi-compensated targets. Furthermore, a fraction of La^{3+} ions are released towards the Bi-1201 phase and, at the same time, the structure of Bi-2201 becomes more complete, i.e. narrower RC. As a consequence, we have a better Bi-2201 structure but a higher amount of Bi-1201 aggregates. Moreover, the resistivity measurements show that for

the same La doping, the T_c is lower for a Bi-compensated sample (Fig. 5.18).

5.4.6 Resistance measurements

The measurements of the critical temperature T_c for films evidencing the presence of IG enlighten the fact that it is not always manifest and easy to detect the presence of embedded polytypes. The measurement in Fig. 5.19 proves indeed that there is not a clear, observable difference between samples with and without IG. For this reason, it is fundamental to perform a refined structural analysis described in the previous sections in order to exclude the presence of IG in the samples.

Moreover, the resistivity measurements show that for the same La doping, the T_c is lower for a Bi-compensated sample (Fig. 5.18). This can be accounted for the higher amount of defects and for the fact that the effective La doping is lower than in a stoichiometric sample. While the presence of defects is detrimental from the crystal-structure point of view, it is favoring the inclusion of La^{3+} in the Bi-2201 phase more than for Bi-compensated samples with less defects.

30% La doped Bi-2201
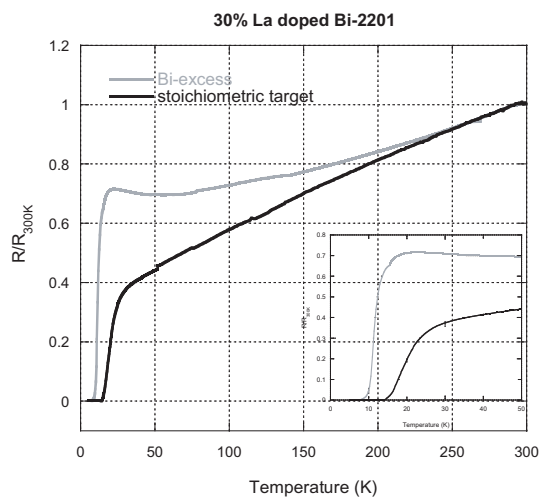
Figure 5.18: Comparison of the normalized resistance for stoichiometric and Bi-compensate 30% La-doped samples.
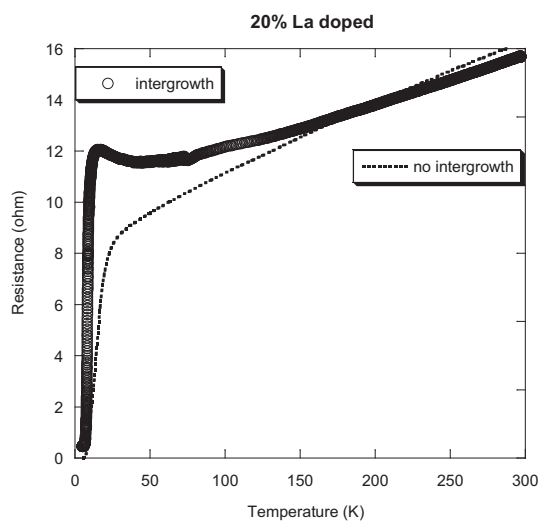
20% La doped

Figure 5.19: Comparison of the resistance measurements versus temperature of a 20% La-doped film showing the presence of random IG and a single-phased film.

5.5 In-situ ARPES measurements

After the optimization of the growth of La-doped Bi-2201 thin films, we are able to deposit pure single-phased films. This is an important step before

ARPES

Connection

PLD
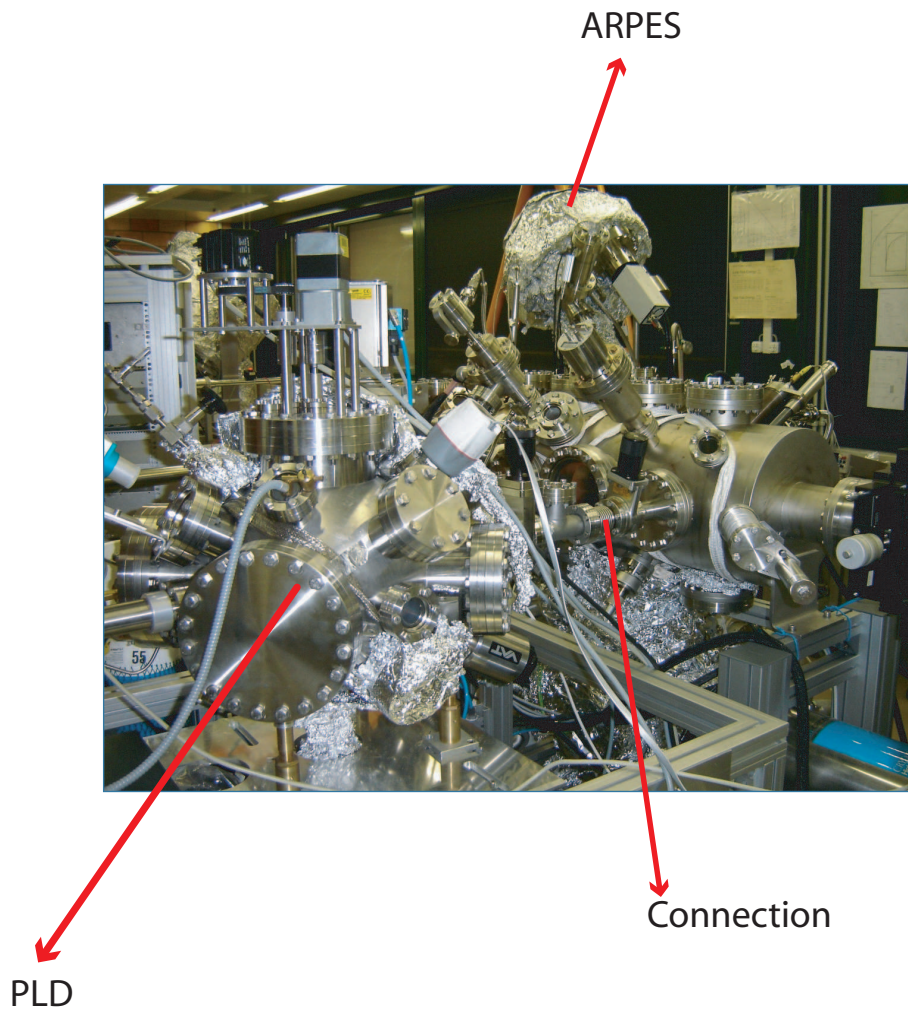
Figure 5.20: Picture of the PLD directly connected to the photoemission set-up.

performing any photoemission experiments, as the knowledge of the structural quality of the films is crucial for interpreting the photoemission data. Under these conditions we can perform photoemission analysis on our films. When we begun the collaboration with Prof. Grioni (IPN) on ARPES on thin films, we used to transfer samples in a static oxygen atmosphere of 1 atm and we suspected that the surface was contaminated during the transfer period. In order to improve the transfer procedure I adapted the laser ablation
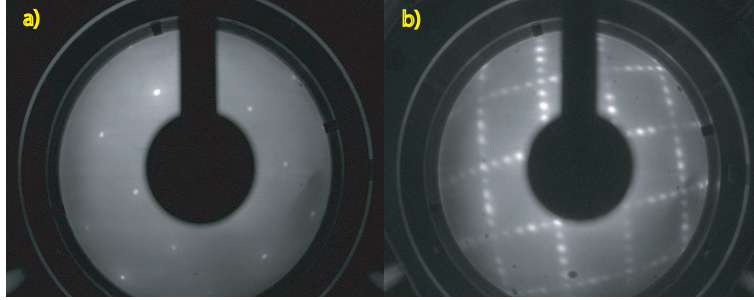
Figure 5.21: a) LEED image of a STO (100) substrate and b) LEED image of a La-doped Bi-2201 thin film grown on a STO (100) substrate.

system and moved it to the photoemission laboratory. The direct connection with the SCIENTA system solved definitely the problem of surface contamination due to the static oxygen atmosphere during the transfer procedure. As-grown samples are directly transferred into the analysis chamber to measure their band structure. The picture of the PLD system connected to the photoemission system is shown in Fig. 5.20.

We used a photon energy of 21.2 eV with a SCIENTA Phoibos hemispherical energy analyzer for the film studies. We have succeeded to measure the band dispersions of different La-doped Bi-2201 samples along the $\Gamma - M$ and the $\Gamma - Y$ direction in order to map the complete FS. It is important to mention that the life-time of a sample in the photoemission chamber was varying between 30 - 45 minutes. However, the surface quality can be fully restored after 1 hour annealing at 700 °C in 1 atm of O_2.

After the deposition, the films are transferred in the LEED chamber. A typical LEED image of a La-doped Bi-2201 thin film grown on a (100) STO substrate is shown in Fig. 5.21 b). We observe an ordered crystallographic structure induced by the substrate (see Fig. 5.21 a)) which presents a 5×1 modulation [48, 42] along both a- and b-axes. However, the twinning cannot be avoided due to the in-plane structure of the substrate. When Bi atoms

are partially replaced by Pb, the structural modulation on the Bi-O layer along the b-axis can be completely suppressed [13, 14, 26].
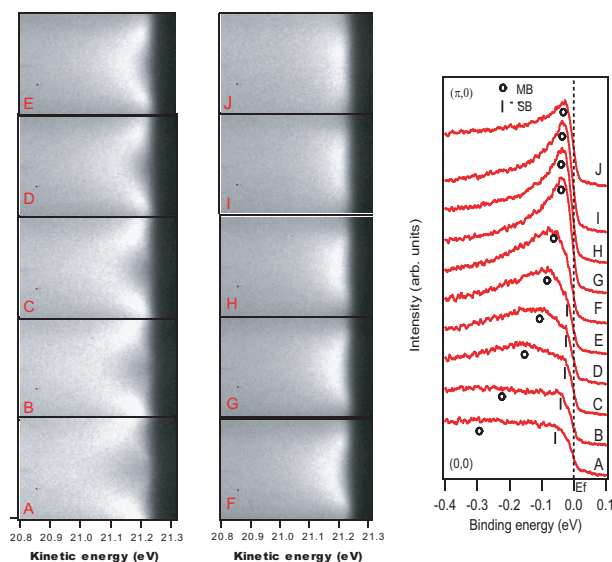
Figure 5.22: On the left: ARPES intensity images; on the right: the energy distribution curves along the $\Gamma - Y$ direction.

All the ARPES intensity maps are measured at 70 K. In Fig. 5.22 - 5.23 the band dispersions along the $\Gamma - M$ cut in the BZ are plotted. When approaching the $(\pi, 0)$ point, the band gradually becomes less dispersive and
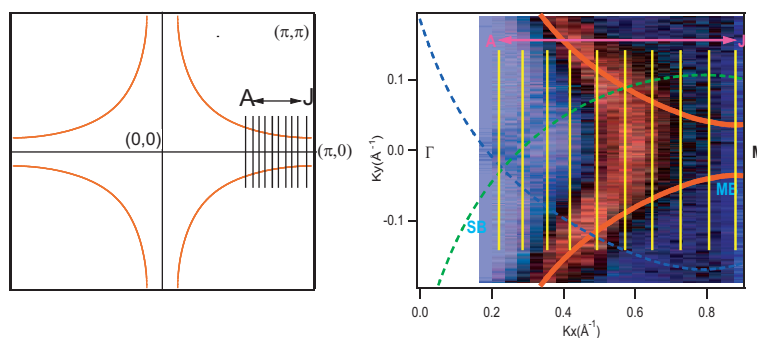
Figure 5.23: FS mapping along the $\Gamma - M$ cuts.
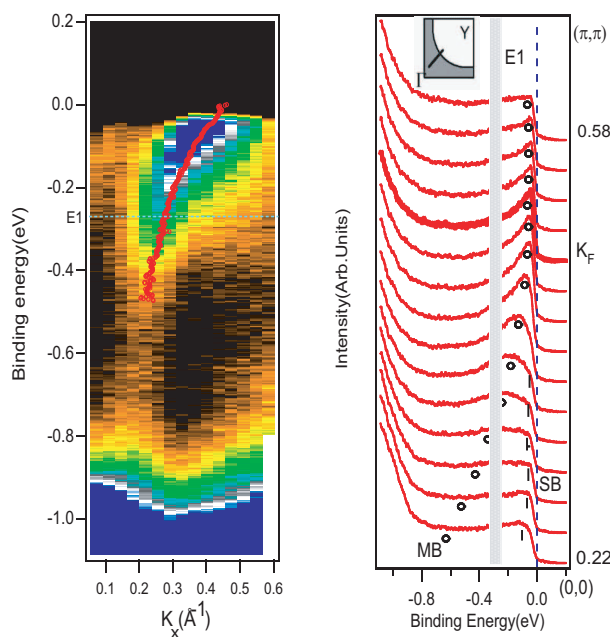
Figure 5.24: On the left: ARPES intensity images for a photon energy of 21.2 eV as a function of energy and momentum values obtained along various momentum cuts; on the right: the corresponding energy distribution curves along the $\Gamma - Y$ direction.
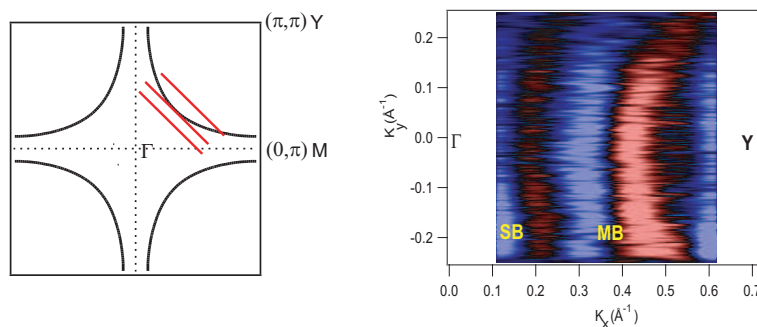
Figure 5.25: Momentum cuts along the $\Gamma - M$ direction and the Fermi surface reconstructed from the cuts.

finally almost flat around the M point. The band appears to be located below E_F at the $(\pi, 0)$ point which indicates a hole-like FS. In Fig. 5.23 the FS is mapped. We used a 2DTB fit for mapping the FS by using the

following formula:

$$E_k = t_0 - 2t_1(\cos k_x + \cos k_y) + 4t_2 \cos k_x \cos k_y. \qquad (5.5)$$

The solid line and the dashed line represent the main band (MB) and the diffraction replica band (SB) respectively, which are also calculated from the TB model.

The EDCs in the normal state along $(0, 0)$ to (π, π) are plotted in Fig. 5.25 - 5.24. We can notice in Fig. 5.24 that when the binding energy reaches the value $E_1 \approx 0.3$ eV, the dispersion suddenly undergoes a kink behavior [30, 58]. This high-energy kink [40] was also observed in other materials like LSCO [17], and poses new challenges for the physics of cuprates: this high-energy kink can be related to superconductivity and it can represent an important step towards the ultimate understanding of the high temperature superconductivity. Already the observation of a "low-energy kink" around 50 meV was read as a manifestation of electron-phonon coupling: phonon branches exist at this energy scale. Ellipsometry and Raman scattering techniques could also provide information on the role of phonons in high-T_c superconductivity [56]. These results gave a new impetus in the HTSC physics by renewing the importance of the electron-phonon interaction in the quasiparticle scattering and in the pairing mechanism in HTSC.

The high-energy kink occurs at an energy level that is almost one order of magnitude higher in energy (200 - 300 meV) than the low-energy kink, excluding in this way its phononic origin. Its interpretation is controversial and still under an actual debate. One possible interpretation suggests the hypothesis that this phenomenon can be related to spin fluctuations, which would actually be in the good energy range [58]. Other interpretation [61] considers that the remarkable giant kink structure observed provide a rare

chance to extract the full self-energy of a strongly correlated system, which reflect all correlation effects in the system. The resulting partial self-energy was argued to contain information on interactions between electrons and certain bosons. Still related to many-body interactions, the high energy kink may be related to the short range Coulomb interaction as in the Hubbard (or t-J) model [44].

Concluding remarks and Outlook

We have studied in detail the growth and structural and electronic properties of LSCO and Bi-2201 thin films. I have built a PLD system for the deposition of high T_c films at EPFL and have adapted it to perform direct in-situ ARPES measurements by using an in-house SCIENTA system.

What I have learnt, among other things, is that the growth mastery and structural characterization of thin films is a crucial step in order to elucidate the electronic properties measured by ARPES and other techniques.

We introduced a specific methodology to detect the presence of inter-growth of polytypes in thin films and we have developed a simple model to explain the random nucleation of intercalates during the deposition by PLD. We varied the growth conditions and the post-annealing treatment in order to optimize the quality of our samples and grow single-phase samples. We succeeded to perform in-situ ARPES measurements on Bi-2201 thin films: the Fermi surface could be completely mapped. Further experimental work is needed to clarify the presence of singular features like the high energy kink in Bi-2201 thin films. Moreover, performing ARPES measurements varying the temperature will eventually allow the study of the pseudogap that is a crucial aspect in these materials.

ARPES measurements on HTSC very thin films showed surprising effects of the in-plane strain on the electronic properties. We studied the effect of tensile strain on LSCO thin films: we produced samples with different thicknesses and different oxygen contents. Contrary to the 2D dispersion of both, bulk and compressive strained samples, thin tensile strained samples showed a 3D band dispersion. In addition, below 18 UCs, they exhibit a staircase structure indicating wavevector quantization along the direction parallel to the growth direction (z-axis). This has been exploited in order to extract the band parameters without resorting to the controversial NFEA. In addition, we showed that by including an effective mass anisotropy in the NFEA, the probing surface in momentum space for single photon energy ARPES experiments can be correctly described accounting for the observed staircase structure. The 3D band parameters obtained from the dispersion fit vary with the film thickness. In general we observed a dimensional crossover from a 2D to a 3D character, evidencing the presence of a critical film thickness. This regime change in the electronic band dispersion is most pronounced in samples with interstitial oxygen where the 3D character is strongly enhanced for films with less than 18 UCs. Furthermore, these films reveal a visible change in their structural properties at the same critical film thickness of 18 UCs. The obvious presence of a critical thickness revealing the same value in both the structural and the electronic film characteristics suggests the existence of an intimate nexus between these two.

By comparing O_2 trapped in films with O_2 free samples, we showed that the dimensional crossover is triggered by the in-plane tensile strain. Therefore the oxygen trapping is not essential for this evolution of the electronic structure with thickness. However, huge values of the out-of-plane hopping terms in O_2 rich samples show that interstitial oxygen amplifies the z-dispersion

channel.

We suggested that these experimental facts must be attributed to the interplay of the substrate-induced epitaxial strain and its gradual relaxation. The question arises now how these two features are correlated with superconducting properties. Further experiments can be performed in order to measure the T_c as a function of the thickness. A systematic comparison between the film thickness, the level of the epitaxial strain field and the electronic properties of the thin films would allow to elucidate the correlation between the strain and the critical temperature T_c as well as the role of a critical film thickness for which the structural and electronic properties change.

Last but not least, all of my work can be extended and adapted to related heteroepitaxial materials; most of them are relevant within a broad field of emerging nanoscience.

Chapter 6

Appendix

6.1 Elements of X-ray diffraction

6.1.1 The diffracted wave amplitude

Typical interatomic distances in solids are on the order of an angstrom (10^{-10} m). An electromagnetic probe of the microscopic structure of a solid must therefore have a wavelength at least this short, corresponding to an energy of the order $\hbar\omega = \frac{hc}{\lambda} = \frac{hc}{10^{-10}\text{m}} \approx 12.3 \times 10^3$ eV. Energies like this, on the order of several thousands of electron volts (keV), are characteristic X-ray energies.

X-ray scattering techniques are a family of non-destructive analytical techniques which reveal information about the crystallographic structure, chemical composition, and physical properties of materials and thin films. XRD in general represents a powerful tool for investigating structures at the interatomic length scale of condensed matter. XRD techniques are based on the elastic scattering of X-rays from structures that have long range order.

These techniques are based on the observation of the scattered intensity

of an X-ray beam hitting a sample as a function of scattering angle 2θ, measured with respect to the direction of the incident beam, that is inclined by an angle Ω to surface of the sample.
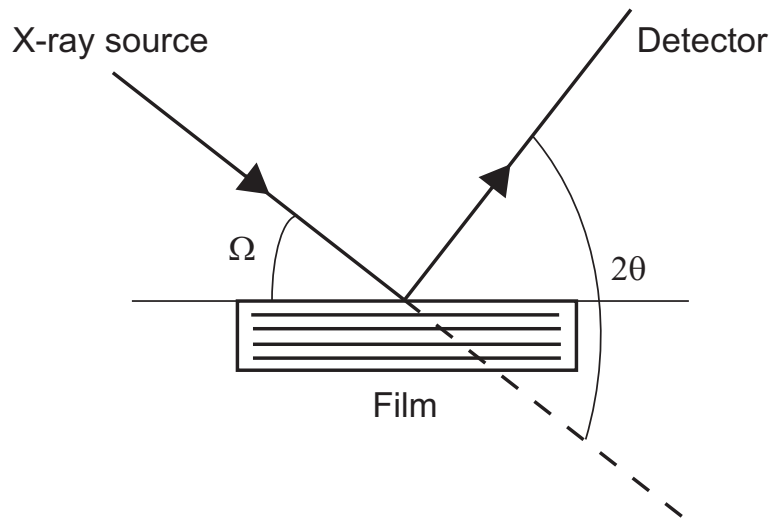
Figure 6.1: Sketch of the diffraction setup.

One of the widely-used experimental setups is the specular configuration, also called the *Bragg-Brentano* geometry. This setup consists in the test arrangement where the surface normal to the sample surface, or to the normal of the set of planes one would like to examine, is on the bisecting line of the angle formed by incident and the diffracted line. In these conditions the incident angle amounts to $\Omega = \theta$ in Fig. 6.1.

The calculation of the diffracted intensity $I(\theta)$ in specular geometry requires the evaluation of the diffracted amplitude $A(\theta)$. The latter represents the coherent sum of the contributions of every crystalline plane parallel to the surface of the structure:

$$A(\theta) = \sum_m \sum_p f_{(p)} \exp\left(i\Phi_{(p)}^{(m)}\right), \text{ with } \Phi_{(p)}^{(m)} = \frac{4\pi \sin(\theta)}{\lambda} z_{(p)}^{(m)}. \qquad (6.1)$$

$f_{(p)}$ and $z_{(p)}^{(m)}$ are respectively the structure factor and the position of the plane indexed by (p) within the UC indexed by (m), where $p,\, m \in \mathbb{N}$. λ represents the wave length of the incident beam.

If we are examining a periodic crystalline structure, as it is almost always the case, we can benefit from the periodicity of the lattice and express the position $z_{(p)}^{(m)}$ as follows:

$$z_{(p)}^{(m)} = mc + z_p, \qquad (6.2)$$

where c is the lattice parameter in the direction of the plane normal and z_p represents the position in the same direction within the UC. In the event of an angle θ being in Bragg condition, that is to say

$$2c\sin\left(\theta_B^{(n)}\right) = n\lambda, \qquad (6.3)$$

the expression for the phase in Eq. 6.1 is rewritten as

$$\Phi_{(p)}^{(m)}\left(\theta_B^{(n)}\right) = 2\pi nm + n\phi_p, \text{ where } \phi_p = 2\pi\frac{z_p}{c}, \qquad (6.4)$$

where $n \in \mathbb{N}$ denotes the diffraction order. The Bragg law is a consequence of the periodicity of the lattice. Notice that the law does not refer to the composition of the basis of atoms associated with every lattice point. However, the composition of the basis determines the relative intensity of the various orders of diffraction from a given set of parallel planes.

The amplitude for a Bragg angle can be expressed as:

$$A_B^{(n)} = M \sum_{p \in UC} f_p\left(\theta_B^{(n)}\right) \exp\left(in\phi_p\right) \equiv M F_{UC}\left(\theta_B^{(n)}\right). \qquad (6.5)$$

M counts the total number of UCs in the direction of the plane normal and F_{UC} represents the UC's structure factor. Thus F_{UC} is the Fourier transform of the density of diffracting matter within the UC, relative to the wave number $q_n = n\frac{2\pi}{c}$. Remark that in Eq. 6.5 the angular dependance has been included in the planar structure factors, reminding the angular dependance of the scattering cross sections of the individual atoms.

The result in Eq. 6.5 is generalized for any arbitrary diffraction angle by replacing the diffraction order n, that is an integer in Bragg condition, by its continuous analog

$$\tilde{n}(\theta) = \frac{2c \sin(\theta)}{\lambda}. \qquad (6.6)$$

In the same way one can express the total number of UCs in the out-of-plane direction as a function of the phase factors over the total crystal thickness, $\tilde{M}(\theta)$:

$$\tilde{M}(\theta) = \left|\sum_{m=1}^{M} \exp\left(2\pi i m \tilde{n}(\theta)\right)\right| = \left|\frac{\sin\left(\pi M \tilde{n}(\theta)\right)}{\sin\left(\pi \tilde{n}(\theta)\right)}\right|, \qquad (6.7)$$

which is an interference function that serves as a counter: it takes the maximal value M for every Bragg angle.[1]

The total diffracted intensity is proportional to the square of the diffracted amplitude. In the case of a massive sample and in the specular diffraction geometry, the absorption of the X-rays by the sample is not subject to an

---

[1]Eq. 6.7 is at the bottom of the finite size oscillations we will mention in section 6.1.3 in order to calculate the number of UCs of very thin films.

angular dependency. Therefore the geometry of the specular diffraction conditions just requires the introduction of the Lorentz polarization factor in order to describe the intensity of the diffracted beam on a rigid periodic crystal structure:

$$I_0 = \left| \tilde{M}(\theta) \right|^2 |F_{UC}(\theta)|^2 \frac{1 + \cos^2(2\theta)}{\sin(\theta)}. \tag{6.8}$$

We are about to describe how the distribution of X-rays scattered by a *rigid, periodic* array of ions reveals their locations within that structure. Actually the ions vibrate around their ideal equilibrium sites. This does however not affect the conclusions reached so far. Though in the early days of XRD it was not clear why such vibrations did not obliterate the pattern characteristic of a periodic structure. It turns out that the vibrations have two main consequences: the intensity in the characteristic peaks that reveal the crystal structure is diminished, but not eliminated; and a much weaker continuous background of radiation, the so-called diffuse background, is produced. As the temperature of the crystal is increased, the intensity of the Bragg-reflected beams decreases, but the angular width of the reflected line does not change. It is surprising that one can get a sharp X-ray reflection from atoms undergoing large amplitude random thermal motion, with instantaneous nearest-neighbor spacings differing by 10% at room temperature. The objection was made that the instantaneous positions of the atoms in a crystal at room temperature are far from a regular periodic array, because of the large thermal fluctuation. Therefore, the argument was brought forward that one should not expect a well-defined diffracted beam. But such a beam was found. The reason was given by Debye [2]. Consider the radiation

---

[2] "... I came to the conclusion that the sharpness of the interference lines would not suffer but that their intensity should diminish with increasing angle of scattering, the more so the higher the temperature." P. Debye.

amplitude scattered by a crystal: let the position of the atom nominally at $\mathbf{r}_j$ contain a term $\mathbf{u}(t)$ fluctuating in time: $\mathbf{r}(t) = \mathbf{r}_j + \mathbf{u}(t)$. We suppose each atom fluctuates independently about its own equilibrium position.[3] By re-considering Eq. 6.5 we state that the structure factors appear in the general form of $f_p \exp(i\mathbf{q} \cdot \mathbf{r}_p)$ in three dimensions. Hence the thermal average of the structure factor contains terms

$$f_p \exp(i\mathbf{q} \cdot \mathbf{r}_p) \left\langle \exp\left(i\mathbf{q} \cdot \mathbf{u}\right) \right\rangle, \tag{6.9}$$

where $\langle ... \rangle$ denotes the thermal average. Its series expansion is

$$\left\langle \exp\left(i\mathbf{q} \cdot \mathbf{u}\right) \right\rangle = 1 + i\langle \mathbf{q} \cdot \mathbf{u} \rangle - \frac{1}{2}\left\langle \exp\left(i\mathbf{q} \cdot \mathbf{u}\right)^2 \right\rangle + \cdots. \tag{6.10}$$

But $\langle \mathbf{q} \cdot \mathbf{u} \rangle = 0$ because $\mathbf{u}$ is a random thermal displacement and therefore completely uncorrelated with the direction of $\mathbf{q}$. In addition, we have

$$\left\langle (\mathbf{q} \cdot \mathbf{u})^2 \right\rangle = q^2 \langle u^2 \rangle \left\langle \cos^2(\theta) \right\rangle = \frac{1}{3}\langle u^2 \rangle q^2, \tag{6.11}$$

where the factor $\frac{1}{3}$ arises as the geometrical average of $\cos^2(\theta)$ over a sphere. The function

$$\exp\left(-\frac{1}{6}\langle u^2 \rangle q^2\right) = 1 - \frac{1}{6}\langle u^2 \rangle q^2 + \cdots \tag{6.12}$$

has the same series expansion as the one in Eq. 6.10 for the first two terms. For a harmonic oscillator all terms in the series (6.10) and (6.12) can be shown to be identical. Then the scattered intensity, which is the square of the amplitude, is

---

[3]This picture corresponds to the Einstein model of solids; it is not a very good model at low temperatures, but it works well at high temperatures.

$$I = I_0 \exp\left(-\frac{1}{3}\langle u^2 \rangle q^2\right), \tag{6.13}$$

where I_0 is the scattered intensity from the rigid lattice. The exponential factor is the **Debye-Waller factor**.

$\langle u^2 \rangle$ is considered as the mean square displacement of an atom from its nominal position on a rigid lattice. The thermal average potential energy $\langle U \rangle$ of a classical harmonic oscillator is in three dimensions is $\frac{3}{2}k_B T$, hence

$$\langle U \rangle = \frac{1}{2}M\omega^2 \langle u^2 \rangle = \frac{3}{2}k_B T, \tag{6.14}$$

where C is the force constant, M is the mass of an atom, and ω is the frequency of the oscillator, with $\omega^2 = \frac{C}{M}$. Thus the scattered intensity is given by

$$I(hkl) = I_0 \exp\left(-\frac{k_B T q^2}{M\omega^2}\right), \tag{6.15}$$

where hkl are the indices of the reciprocal lattice vector $\mathbf{q}$. This classical result is a good approximation at high temperatures.

For quantum oscillators $\langle u \rangle$ does not vanish even at $T = 0$ because of the zero-point motion. On the independent harmonic oscillator model the zero-point energy is $\frac{3}{2}\hbar\omega$, which is the energy of a 3D quantum harmonic oscillator in its ground state referred to the classical energy of the same oscillator at rest. Half of the oscillator energy is potential energy, so that in the ground state we have

$$\langle U \rangle = \frac{1}{2}M\omega^2 \langle u^2 \rangle = \frac{3}{4}\hbar\omega \implies \langle u^2 \rangle = \frac{3\hbar}{2M\omega}. \tag{6.16}$$

By analogy with Eq. 6.13 we can write

$$I(hkl) = I_0 \exp\left(-\frac{\hbar q^2}{2M\omega}\right) \qquad (6.17)$$

at absolute zero.

One sees from Eq. 6.15 that the intensity of the diffracted line decreases as the temperature is increased. Reflections of low q are affected less than reflections of high q. The expression for the intensity that has been established in Eq. 6.15 is that of the coherent diffraction, this means the elastic scattering, in the well defined Bragg conditions. The intensities lost from these directions is the inelastic scattering and appears as a diffuse background. In inelastic scattering processes the X-ray photon causes the excitation or de-excitation of a lattice vibration mode, and the photon changes direction and energy.

Amorphous solids and liquids have about the same density as crystalline solids, and are therefore also susceptible to probing with X-rays. However, the discrete, sharp peaks of scattered radiation characteristic of crystals are not found.

6.1.2   RC and in-plane crystal coherence

One can distinguish two particular kinds of defects in epitaxial crystal: uncorrelated defects such as orientational disorder of single crystalline domains, also called "mosaic texture", and correlated defects along the c-axis, the so-called "stacking faults". According to the occurrence of either of these structural defects in the film, the RC will be influenced in two different ways.

The mosaic texture consists of randomly oriented crystal domains around a mean position which is the c-axis of the epitaxial film, as illustrated in Fig. 6.2. In this case, the diffracted intensity is the incoherent sum of the
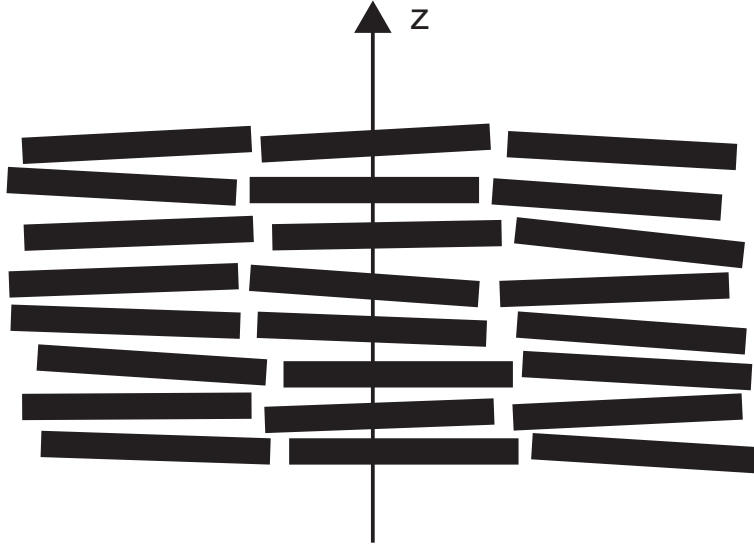
Figure 6.2: Mosaic structure. The crystalline domains are randomly oriented around the film's c-axis.

contribution of every individual crystalline domain. The RC will embody the angular distributions of the domains, resulting in a Gaussian line shape.

Stacking faults, however, involve random rigid spatial displacements of crystal domains along the c-axis, implying a rapid in-plane decorrelation of atomic positions, whereas the periodicity along the c-axis is conserved, as depicted in Fig. 6.3. The density distribution of UCs in a structure illustrated in Fig. 6.3 can be written as

$$\rho^{UC}(\mathbf{r}) = \rho_{//}(x,y) \sum_k \delta(z - kc), \qquad (6.18)$$

where c denotes the film's c-axis. The in-plane correlation radius, defined as $\frac{\xi}{2}$, characterizes the density-density correlation function, $G(x - x')$, given by

$$G(x - x') = \left\langle \rho_{//}(x)\rho_{//}(x') \right\rangle = \left(\rho_{//}^0\right)^2 \exp\left(-\frac{x - x'}{\frac{\xi}{2}}\right), \qquad (6.19)$$
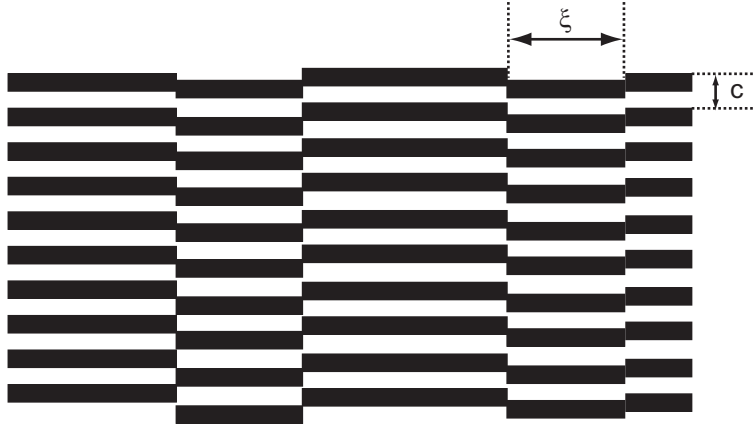
Figure 6.3: Stacking faults. The in-plane coherence of the crystal structure is diminished by the rigid vertical displacements of the crystalline domains. ξ denotes the in-plane coherence length.

where $\left(\rho_{//}^{0}\right)^{2} = \frac{1}{a}$ is the number of in-plane UCs per unit length. $G(x - x')$ is obtained by computing the probability of finding two UCs centered at the same vertical position z of a single domain at a relative lateral distance $|x - x'|$. We define $p = \exp\left(-\frac{a}{\frac{\xi}{2}}\right) \leq 1$ as the probability for a UC to be centered vertically at a given z value. Then, the probability that two UCs are located in the same columnar domain at the same z value amounts to $P \equiv p^{n}$, where $n = \frac{|x-x'|}{a}$ denotes the number of intermediate UCs in the horizontal plane. As a matter of fact all these intermediate UCs on that plane must exhibit the same z value. Hence, the probability of finding two UCs centered at the same z value in the same domain and at a relative lateral distance $|x - x'|$ is given by $P = p^{n} = \exp\left(-\frac{|x-x'|}{\frac{\xi}{2}}\right)$.

The diffracted intensity is formally written as

$$I(\mathbf{q}) = |F(\mathbf{q})|^{2}, \tag{6.20}$$

with the amplitude given by

$$F(\mathbf{q}) = \int \mathrm{d}^3 r \rho^{UC}(\mathbf{r}) f_{UC} \exp(i\mathbf{q} \cdot \mathbf{r}), \qquad (6.21)$$

where $f_{UC} = f_{UC}(\mathbf{q})$ represents the UC's structure factor. $\mathbf{q}$ is the momentum transfer vector, defined as $\mathbf{q} = \mathbf{q}_{ref} - \mathbf{q}_{in}$ and illustrated in figure 6.4. In
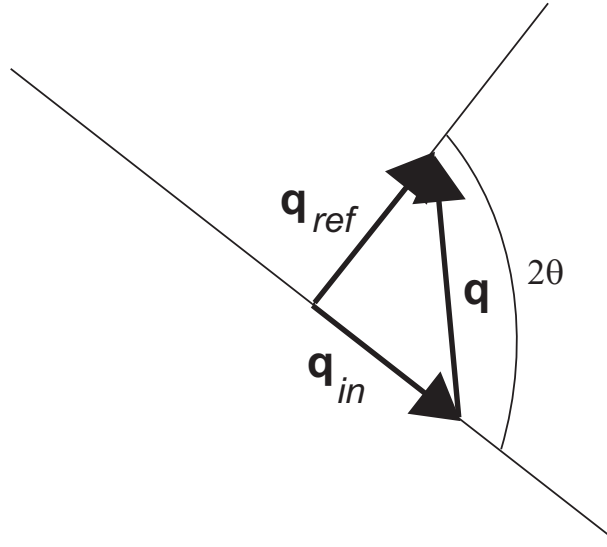
Figure 6.4: Sketch of the momentum transfer vector $\mathbf{q}$ being the vectorial difference of the "reflected" (ref) and incident (in) momentum vector.

the case of the RCs, $\mathbf{q}$ is not always parallel to the c-axis of the film, but can approximatively be expressed as $\mathbf{q}(\Omega) \approx q\hat{\mathbf{z}} + \delta q\hat{\mathbf{x}}$, where $q \equiv |\mathbf{q}| = \frac{4\pi \sin(\theta)}{\lambda}$ denotes the norm of the momentum transfer vector, δq is defined by $\delta q = q\delta\theta$ with $\delta\theta$ being the deviation of Ω with respect to the Bragg angle θ_B, $\hat{\mathbf{z}}$ designates the unit vector parallel to the film's c-axis, and $\hat{\mathbf{x}}$ represents the unit vector being parallel to the diffracting planes and normal to both the c-axis of the film and the Ω rotation axis.

Using the relation given in Eq. 6.18, the RC amplitude, presented in Eq.

6.21, can be written as:

$$F(\mathbf{q}) = \int_V \mathrm{d}^3 r f_{UC} \rho^{UC}(\mathbf{r}) \exp(i\mathbf{q} \cdot \mathbf{r})$$

$$= f_{UC} \int \int \mathrm{d}x \mathrm{d}y \rho_{//}(x,y) \exp(i\delta qx) \sum_k \exp(iqkc). \tag{6.22}$$

Integrating over the y variable and using the Bragg condition along the z-direction, given in Eq. 6.3, the previous Eq. 6.22 yields

$$F(\mathbf{q}) = f_{UC} N_y N_z \int \mathrm{d}x \rho_{//}(x) \exp(i\delta qx) = \frac{F(\mathbf{q}_B)}{N_x} \int \mathrm{d}x \rho_{//}(x) \exp(i\delta qx), \tag{6.23}$$

where N_x, N_y and N_z are the numbers of UCs along each spatial direction. The associated intensity, given in Eq. 6.20, can be rewritten as:

$$I(\mathbf{q}) = I(\mathbf{q}_B) \int \int \frac{\mathrm{d}x \mathrm{d}x'}{N_x^2} \rho_{//}(x) \rho_{//}(x') \exp\left(i\delta q(x-x')\right)$$

$$= I(\mathbf{q}_B) \int \mathrm{d}(x-x') \left\langle \rho_{//}(x) \rho_{//}(x') \right\rangle \exp\left(i\delta q(x-x')\right) \equiv I(\mathbf{q}_B) \tilde{G}(\delta q). \tag{6.24}$$

Hence the intensity is proportional to the Fourier transform $\tilde{G}(\delta q)$ of the density-density correlation function $G(x-x')$ and can be written as follows:

$$I(\mathbf{q}) = I(\mathbf{q}_B) \frac{1}{1 + \left(\delta q \frac{\xi}{2}\right)^2}. \tag{6.25}$$

By using $\delta q = q\delta\theta$, $q = \frac{4\pi \sin(\theta)}{\lambda}$, and the Bragg condition, given in Eq. 6.3, we can finally write:

$$I(\theta) = I(\theta_B^{(n)}) \frac{1}{1 + \left(\frac{4\pi \sin(\theta_B^{(n)})}{\lambda} \frac{\xi}{2} \delta\theta\right)^2} = I(\theta_B^{(n)}) \frac{1}{1 + \left(n\pi \frac{\xi}{c} \delta\theta\right)^2}, \tag{6.26}$$

where (n) denotes the diffraction order of the considered Bragg peak.

In conclusion, neglecting size effects and the finite instrumental resolution, the RC is a **Lorentzian** with a FWHM $\Delta\Omega$ inversely proportional to the in-plane coherence length ξ:

$$\frac{2\delta\theta}{\Delta\Omega} \equiv n\pi\frac{\xi}{c}\delta\theta \Rightarrow \xi = \frac{2c}{n\pi\Delta\Omega}. \qquad (6.27)$$

Remark that the in-plane coherence length is the double of the in-plane coherence radius defined at the beginning of the derivation.

6.1.3 Diffraction of crystals of very small size: the "Scherrer formula"

In the preceding sections we have assumed that the X-rays are reflected on a set of reticular planes constituting the film body. These reflections sum up in a constructive diffraction signal for a well defined angle, corresponding to a Bragg condition given by $2c\sin(\theta_B) = n\lambda$, or at least in an angular interval that is sufficiently small so that the observed broadening of the diffraction lines depends only on the experimental conditions, such as the extension of the incident beam, the size and the form of the sample. This occurrence is only verified if the volume of the diffracting film body is not too small. Basically the dimensions of the crystal must exceed a thousand times the wavelength of the incident beam, this means a few thousands of Å. Otherwise the diffraction lines undergo a broadening that is perceptible in the experiment. However this broadening can to be exploited in order to determine the size of submicroscopic crystals.

This size effect is analogous to a well-known phenomenon occurring in optical gratings. The position of the maximum of the diffracted signal only depends on the grating constant, whereas the the broadening of the spectral

lines is the smaller, the bigger the number of the grating is. In the case of X-rays, the deciding factor is the number of the intervening reticular crystal planes. In principle, the elementary calculation is identical to the determination of the resolution power of optical gratings.

Let us consider a film that is composed of N crystalline planes spaced by a distance c. Suppose that we are in the situation that a ray of wavelength λ hits the sample under the Bragg angle θ_B, so that $\lambda = 2c \sin(\theta_B)$. If A represents the diffracted amplitude arising from one single reticular plane, then to an incident beam corresponds a reflected one of amplitude NA, because the waves accruing from the different planes are exactly in phase. The resultant amplitude, denoted by F, can be written as the coherent sum of plane waves in the following way:

$$F = A \sum_{l=0}^{N-1} \exp(iqcl) = A \frac{1 - \exp(iqcN)}{1 - \exp(iqc)} = F_0 \frac{\sin\left(\frac{qcN}{2}\right)}{\sin\left(\frac{qc}{2}\right)}, \qquad (6.28)$$

where F_0 represents the corresponding coefficient. Therefore the arising intensity is of the following form:

$$I = I_0 \left[\frac{\sin\left(\frac{qcN}{2}\right)}{\sin\left(\frac{qc}{2}\right)} \right]^2. \qquad (6.29)$$

In the specular geometry, the momentum transfer vector q corresponding to the Bragg condition is given by $q_B = \frac{4\pi \sin(\theta_B)}{\lambda}$. At this stage let us consider a ray of an incident angle that is slightly different from the Bragg position, namely $\theta_B + \varepsilon$. In this case the optical retardation between two crystalline

planes amounts to

$$2c\sin\left(\theta_B + \varepsilon\right) = 2c\left(\sin(\theta_B)\cos(\varepsilon) + \cos(\theta_B)\sin(\varepsilon)\right)$$
$$\approx 2c\left(\sin(\theta_B) + \cos(\theta_B)\varepsilon\right) = n\lambda + 2c\varepsilon\cos(\theta_B), \tag{6.30}$$

where the integer n denotes the diffraction order. Similarly the momentum transfer vector is affected in the same way. We write $q = \frac{4\pi\sin(\theta_B + \varepsilon)}{\lambda}$, which yields us the expression for the reflected intensity in the direction $\theta_B + \varepsilon$, $I(\varepsilon)$:

$$I(\varepsilon) = I_0 \frac{\sin^2\left(N\frac{2\pi c\varepsilon\cos(\theta_B)}{\lambda}\right)}{\sin^2\left(\frac{2\pi c\varepsilon\cos(\theta_B)}{\lambda}\right)} = I_0 \frac{\sin^2\left(N\Phi\right)}{\sin^2\left(\Phi\right)}, \tag{6.31}$$

where we have defined $\Phi = \frac{2\pi c}{\lambda}\varepsilon\cos\left(\theta_B\right)$ and where we used $\sin^2\left(M\pi + x\right) = \sin^2\left(x\right), \forall M \in \mathbb{N}$.

In order to define the broadening of a diffraction line in a precise way, we determine in a first step the value of ε for which the intensity amounts to the half of the maximal intensity I_0. In other words we have to solve the following implicit equation

$$\frac{\sin^2\left(N\Phi\right)}{\sin^2\left(\Phi\right)} \approx N^2 \frac{\sin^2\left(N\Phi\right)}{\left(N\Phi\right)^2} = \frac{1}{2}. \tag{6.32}$$

The solution of this equation is given by $N\Phi = 0.444\pi$ and therefore we can write $\varepsilon_{I=\frac{1}{2}} = \frac{0.222\lambda}{Nc\cos(\theta_B)}$. A variation ε of the incident angle implies that the diffraction angle between the incidence and reflection directions varies by 2ε. Consequently the angular broadening at the half intensity, the so-called full width at half maximum (FWHM) $\Delta\Omega$, of the observed line amounts to $\Delta\Omega = 4\varepsilon$. Finally, if $t = Nc$ denotes the thickness of the crystal, we can write

$$\Delta\Omega = \frac{0.9\lambda}{t\cos\left(\theta_B\right)}, \tag{6.33}$$

which is known as the "Scherrer formula".

6.2 Basic model for crystalline growth of thin films

In the following we establish the mathematical expression for the strain profile as a function of the film thickness. This relation permits us to extract the density of misfit dislocations of the film. We will encounter the expression of the critical film thickness corresponding to total relaxation. This characteristic length is experimentally accessible by considering the XRD data.

6.2.1 Derivation of the basic model of crystalline growth

We present a minimal model of epitaxial crystal growth assuming that once a crystal layer has been deposited it is immediately "frozen" and the following will adapt on it. It is a matter of local equilibrium and therefore we have to minimize the increment of internal energy density from one layer to the following one. The increment of the internal energy density Δu is given by the following expression [52]:

$$\Delta u = \underbrace{\frac{Y}{1-\nu}\varepsilon^2}_{u_E} + \underbrace{\frac{2u_0}{c\xi}}_{u_D} . \tag{6.34}$$

Y is the Young's modulus, ν the Poisson's ratio, ε the strain, u_0 the energy per unit length of a misfit dislocation, c the c-axis of the film and $\frac{1}{\xi}$ is the density of misfit dislocations per unit length. The increment of internal energy is made up of two competitive components, the first contribution is the elastic energy, u_E, the second is due to misfit dislocations, represented by u_D. Therefore a local equilibrium consists in each step of growth in a compromise between maintaining the strain and relaxation by introducing

misfit dislocations. The density of dislocations $\frac{1}{\xi}$ is considered as a function of z, the position of the growing direction. Its inverse, the quantity ξ, is interpreted as the coherence length, the measure of the size of crystal domains that are separated by dislocation lines. Considered as a discrete function of

$$\xi$$
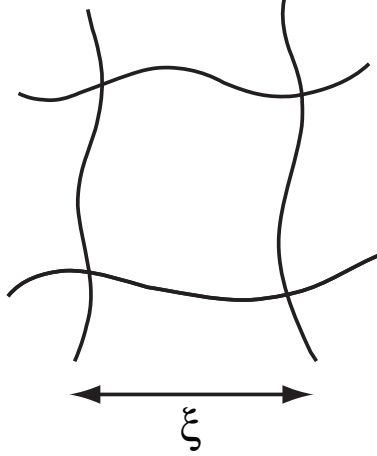
Figure 6.5: Sketch of the in-plane dislocation lines.

the number of UCs in growing direction, labelled by n, $\frac{1}{\xi}_n$ is written as follows:

$$\frac{1}{\xi}_n = \frac{1}{a_n} - \frac{1}{a_{n-1}} = -\frac{\Delta\varepsilon}{a_0(1 + \varepsilon_{n-1})(1 + \varepsilon_n)}, \tag{6.35}$$

where a_n is the in-plane lattice parameter of the nth crystal plane of the film and we defined $\Delta\varepsilon \equiv \varepsilon_n - \varepsilon_{n-1}$. Notice that a_0 represents the in-plane lattice constant of the film bulk in the completely relaxed state. Furthermore the strain ε is to be introduced by definition in Eq. 6.35 as $a_n = a_0(1 + \varepsilon_n)$. Note that we consider the case of a film being under tensile strain, which means that $\varepsilon \geq 0$. The lattice constant of the substrate on which the film is grown, is bigger than the one of the film in its completely relaxed state. In this sense, relaxation of the film means reducing the strain by introducing misfit dislocations that divide the crystal in different domains characterized

126

by ξ. Passing at the continuous limit, i.e. replacing the discrete parameter n, labelling the UC position in growing direction, by the continuous variable z, denoting the total thickness of the film, we can approximately write $\frac{\Delta\varepsilon}{c} \approx \frac{d\varepsilon}{dz} \equiv \varepsilon'$, where c represents the c-axis of the film. Simplification of the right side of Eq. 6.35 by just keeping the leading terms in the denominator yields $\frac{1}{\xi} = -\frac{c}{a_0}\varepsilon'$. Substitution of the preceding expression in Eq. 6.34 results in the following expression for the increment of the internal energy density:

$$\Delta u = \frac{Y}{1-\nu}\varepsilon^2 - \frac{2u_0}{a_0}\varepsilon'. \tag{6.36}$$

The idea is the following: we minimize the increment of internal energy density given by Eq. 6.36 with respect to the strain ε. Remarking that $\frac{\partial}{\partial\varepsilon} \equiv \frac{1}{\varepsilon'}\frac{d}{dz}$, we have to solve the following differential equation

$$\frac{d}{dz}[\varepsilon^2] = \lambda\frac{d^2\varepsilon}{dz^2}, \tag{6.37}$$

that describes the strain at a certain film thickness. The parameter λ has the dimension of length and is given by $\lambda = \frac{2u_0(1-\nu)}{Ya_0}$, it contains the elastic properties of the film. A first integration from $z = 0$ till $z = Z$, the total film thickness, one obtains $\varepsilon^2(Z) - \varepsilon^2(0) = \lambda(\varepsilon'(Z) - \varepsilon'(0))$. By defining $\varepsilon^2(0) - \lambda\varepsilon'(0) \equiv \tilde{\varepsilon}^2$, we get a differential equation of the form

$$-\frac{\tilde{\epsilon}}{\lambda}dz = \frac{d[\frac{\varepsilon}{\tilde{\varepsilon}}]}{1-[\frac{\varepsilon}{\tilde{\varepsilon}}]^2}. \tag{6.38}$$

Integration of the above equation from 0 to Z on the left side and from $\varepsilon(0)$ to $\varepsilon(Z) \equiv \varepsilon$ on the right side respectively, one obtains the expression of the

127

strain, ε, at the height Z in the film, namely

$$\varepsilon(Z) = \tilde{\varepsilon} \tanh\left(\frac{\tilde{\varepsilon}}{\lambda}(Z^* - Z)\right), \qquad (6.39)$$

where Z^* is given by

$$Z^* = \frac{\lambda}{\tilde{\varepsilon}} \operatorname{arctanh}\left(\frac{\varepsilon(0)}{\tilde{\varepsilon}}\right) \qquad (6.40)$$

and represents the critical thickness for which the strain becomes zero, i.e. for which total relaxation is attained.

The value of $\varepsilon(0)$, the initial strain, can already be estimated, under the assumption that the initial strain equals the maximal possible strain. Provided that the in-plane lattice constants of the substrate, a_S, and the one of the relaxed film material, $a_F \equiv a_0$, are known, we can write

$$a_S = a_0\left(1 + \varepsilon(0)\right). \qquad (6.41)$$

The qualitative sketch of the strain profile is shown in Fig. 6.6. Remark that the definition of $\tilde{\varepsilon}^2$ implies that $\tilde{\varepsilon}^2 > \varepsilon^2(0)$, because the physics demands that the variation of the strain is decreasing with the thickness of the film, until the total relaxation is attained, which is characterized by the critical film thickness Z^* so that $\varepsilon(Z^*) = 0$. At a first step, before solving the differential Eq. 6.37, we already had to postulate implicitly that ε' is different from zero everywhere along the strain profile, including at the peculiar film height $Z = 0$. Furthermore it is plausible that the tensile strain relaxes and there is no cause for assumption that the strain could be increased during the epitaxial film growth process. A reinforcement of the tensile strain would be completely contrary to the minimal energy principle. In this sense the variation of the strain in function of the film height is always negative, this
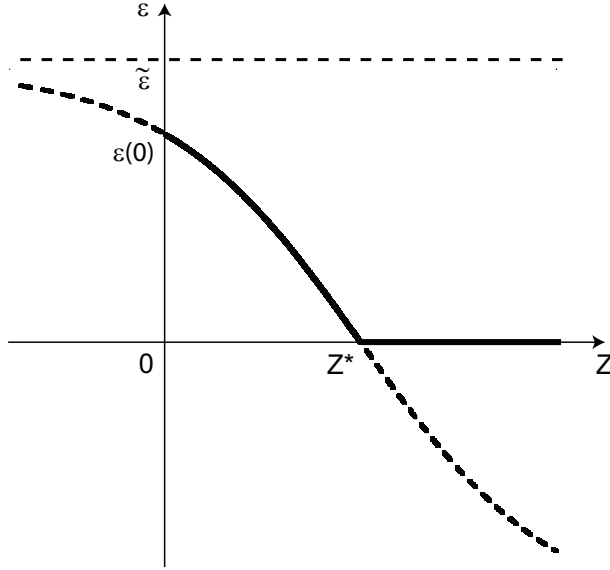
Figure 6.6: Strain profile as a function of the film thickness.

means $\varepsilon' < 0$, for every Z, especially for $Z = 0$.[4] In the film layers grown on top of the critical thicknesses Z^* no strain will be present, this means $\varepsilon(Z) = 0$ for $Z \geq Z^*$. The next step consists in the evaluation of the density of dislocations, $\frac{1}{\xi}(Z)$, considered as a function of the film height Z. We have already stated that $\frac{1}{\xi}(Z)$ is closely connected to the variation of the strain profile in the following way:

$$\frac{1}{\xi}(Z) = -\frac{c}{a_0}\varepsilon' = \frac{c\tilde{\varepsilon}^2}{a_0\lambda}\frac{1}{\cosh^2\left(\frac{\tilde{\varepsilon}}{\lambda}(Z^* - Z)\right)}. \qquad (6.42)$$

The qualitative behavior of the density of dislocations is depicted in Fig. 6.7. Our model predicts an initial value of the density of misfit disloca-

---

[4]By relating the experimental data to this model of crystalline growth, it can be shown that $|\varepsilon(0)|$ is a vanishingly small quantity. In regard to mathematical consistency, we must suppose that $\varepsilon(z)$ is different from zero everywhere, especially at $z = 0$. But for the sake of simplicity, $\tilde{\varepsilon} \approx \varepsilon(0)$ proves to be a good approximation.

129
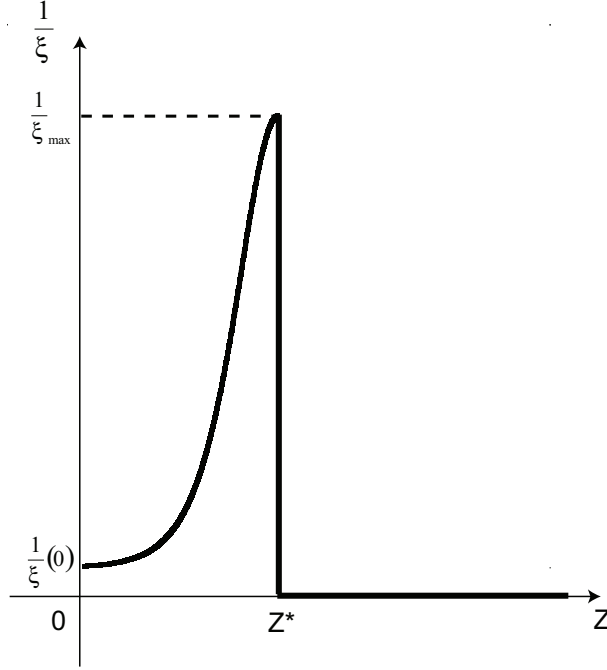
Figure 6.7: Profile of the density of misfit dislocations, due to strain relaxation, as a function of the film height. Once total relaxation is reached at Z^*, no further defaults have to be introduced by reason of the relaxation mechanism. However, a film of higher thickness actually still reveals a residual density of misfit dislocations, in fact at any film height, originating from the relaxation process.

tions, $\frac{1}{\xi}(0)$, that is slightly superior to zero: $\frac{1}{\xi}(0) = \frac{c}{a_0} \frac{\bar{\varepsilon}^2}{\lambda} \left(1 - \left(\frac{\varepsilon(0)}{\bar{\varepsilon}} \right)^2 \right)$. The model anticipates that even the very first deposited film layer reveals a finite, but teeny, density of misfit dislocations. As the film thickness reaches the value Z^*, complete relaxation will be attained. Energetically there is no need anymore to introduce additional lines of misfit dislocations, therefore the density of dislocations attains its maximal value at $Z = Z^*$, namely $\frac{1}{\xi}_{max} \equiv \frac{1}{\xi}(Z^*) = \frac{c\bar{\varepsilon}^2}{a_0\lambda}$. The regime beyond the critical film thickness Z^* is not to be explored by our strain based approach. The mechanism of growth is governed by driving forces other than the interaction of strain maintenance and relaxation by introduction of structural misfit dislocations, the

130

disappearance of the strain vitiates the transference of this model onto the beyond-strain regime.

6.2.2   Local equilibrium versus global equilibrium

We postulated that the strain-relaxation interaction is a matter of *local* equilibrium. We minimized at every step of epitaxial growth the increment of the internal energy Δu and we are conscious of the fact that our picture describes a growth process of quenched film layers. Why should this mechanism not rather concern considerations on *global* equilibrium? The expression for the integral internal energy is established in the following way:

$$U = L_X L_Y \int_0^Z \Delta u(z)\mathrm{d}z,$$

with the same expression of $\Delta u(z)$ as given in Eq. 6.34 and 6.36 respectively. In the idealization of a perfect orthorhombic crystalline film structure, with the in-plane dimensions L_X and L_Y, we immediately replaced the volume integral over $\mathrm{d}V$ by the 1D correspondence over $L_X L_Y \mathrm{d}z$, assuming that $\Delta u = \Delta u(z)$ does not feature any in-plane dependance. Minimization, or more generally extremalization, of the functional U would be tantamount to solving the Euler-Lagrange equation of the integrand Δu, given by

$$\frac{\mathrm{d}}{\mathrm{d}z}\left(\frac{\partial(\Delta u)}{\partial \varepsilon'}\right) - \frac{\partial(\Delta u)}{\partial \varepsilon} = 0.$$

Straightforward execution of the calculation rule in the above equation reveals the trivial solution $\varepsilon = 0$, $\forall z$ as the minimizing strain profile. In general parlance, the state of a global equilibrium demands ab initio an immediate strain relaxation in the film material. This mathematical result, however, contradicts the experimental observations. Substrate-induced

strain is present in thin films and it is downright the aim of producing these materials. On this note, this circumstance reinforces our picture of an out-of-equilibrium epitaxial crystal growth, which can be described as a process governed by a gradual creation of a local equilibrium with respect to the increment of the internal energy density Δu. Furthermore the minimization of the increment of the internal energy density implies an additional feature: the increase in internal energy is the same at every step of epitaxial growth. This insight results immediately from a first integration of the differential Eq. 6.37, leading directly to an expression of the following kind:

$$\frac{Y}{1-\nu}\varepsilon^2 - \frac{2u_0}{a_0}\varepsilon' = \frac{Y}{1-\nu}\varepsilon^2(0) - \frac{2u_0}{a_0}\varepsilon'(0),$$

for which reason we can write more compactly

$$\Delta u(z) = \text{constant}.$$

In other words, at every step of epitaxial film growth, the increment of internal energy reveals the same value, provided that we are in the case of strain-relaxation regime. We interpret this statement in the following way: at every step of epitaxial film growth, the same amount of internal energy has to be added. The uniformity of the increment of the internal energy guarantees that the epitaxial film growth occurs constantly in the same way, this means that crystalline growth is incessantly governed by the principle of the interplay between the maintenance of the strain and strain relaxation. There is no reason to change the growing mechanism abruptly, subject to the condition that the total film thickness in question, Z, is less than the critical film thickness Z^*. The strain and its relaxation by introduction of misfit dislocations balance each other, until the strain is completely relaxed,

132

which occurs at the critical film thickness Z^*. Again, a configuration of the emergence of a negative strain is not physically meaningful, therefore this model does not include the beyond-strain regime. In a certain sense, adding up constantly the same energetic amount per unit volume equals globally a minimization of the total energy content.

6.3 Model for random intergrowth

We propose a simple model for the nucleation of the random intercalates during the PLD growth. This model predicts a very particular spatial distribution of defects: a Markovian-like sequence of displacements along the growth direction (c-axis), as well as a two components in-plane correlation function, characteristic of self-organized intercalates. The other basic assumptions of the models are:

i) The global stoichiometry of the vapor phase is the one of the desired host-phase.

ii) The random nucleation of guest unit cells (GUC) is induced by local composition fluctuations in the top layer under formation and is favored by the reduced in-plane mobility of certain species and the small difference between the formation enthalpies.

iii) The GUC nucleation depends on two parameters: the formation enthalpy difference $V = E_G - E_H$ and the energy per step, U. We assume that the in-plane footprint of the guest and the host are the same, allowing for a perfect epitaxial growth along the c-axis. The step (see Fig. 6.8), defined as a lateral mismatch induced by a finite relative displacement between in-plane adjacent UC, implies a local strain-field with its corresponding elastic energy cost.

iv) The GUC nucleation rate on a given site obeys local thermodynamic equilibrium.

In order to derive a mean-field-like rate equation for the steps, we have to examine different events that may occur during the construction of a given layer, and their corresponding Boltzmann probabilities. The nucleation of a
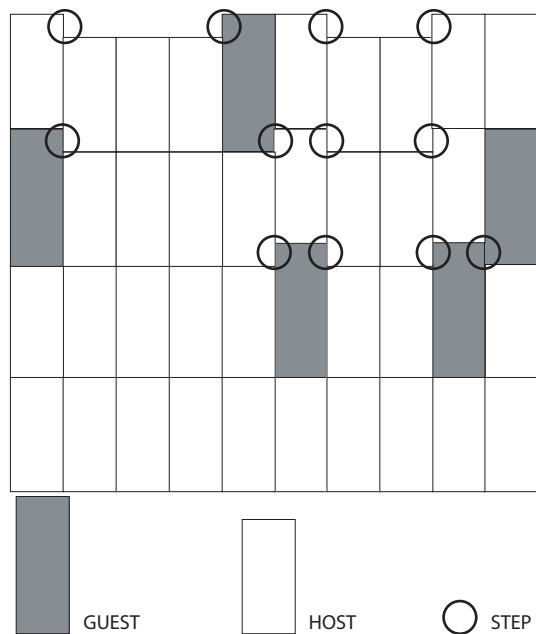
Figure 6.8: Schematic film cross section; formation of steps by random nucleation of GUC.
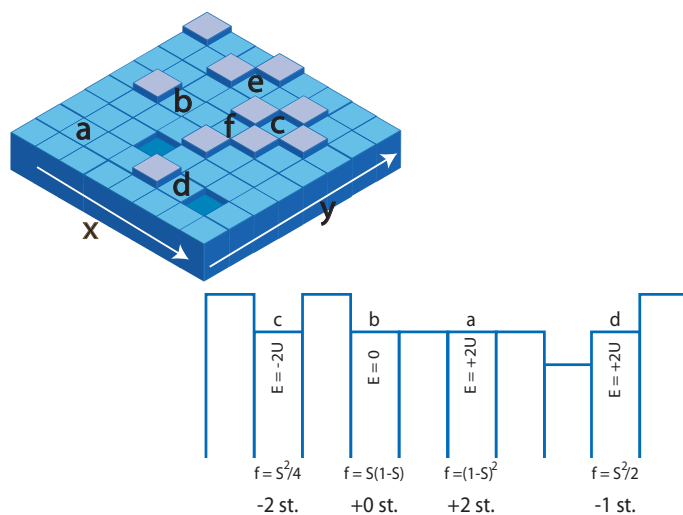
Figure 6.9: Different site environments in 2D and their 1D restriction with the corresponding fractions f, energy costs E, and step number variations.

GUC on top of the former layer depends on the neighboring environment of the considered site, as schematically depicted in Fig. 6.9. Starting with a 2D model (the upper part of Fig. 6.9), and provided the next-neighboring sites are filled with the majority phase, host unit cells (HUCs), if the site belongs to a plateau (type **a**) the nucleation of a GUC will incorporate four additional steps to the system. The corresponding energy cost is $\Delta E = V + 4U$. For a site of type **b**, only two additional steps are incorporated, thus the energy cost is $\Delta E = V + 2U$, etc.. To reduce the 2D layer model to 1D, we have to average over all the possible configurations along the transversal direction (say y). As a result, configurations like **b**, **e** and **f** in the 2D layer are averaged to obtain the **b** configuration in the 1D row (lower part of Fig. 6.9) with an extra formation energy, corresponding to the weighted average of the elastic energy contributions from the corresponding transversal configurations. Assigning to them zero probability, we exclude from the analysis all the events that imply energy costs larger than $4U$. This assumption is justified by the fact that the high energy costs of such events makes their contribution statistically negligible. The fraction of each of the four types of sites, retained for the intergrowth nucleation, can be written in terms of the total 1D-density of steps S within the given row:

$$f_{PLATEAU} = (1 - S)^2, \tag{6.43}$$

$$f_{STEP} = (1 - S)S, \tag{6.44}$$

$$f_{VALLEY} = \frac{1}{4}S^2, \tag{6.45}$$

$$f_{STAIR} = \frac{1}{2}S^2. \tag{6.46}$$

Eq. 6.43 is the probability of finding two consecutive step-free sites. The
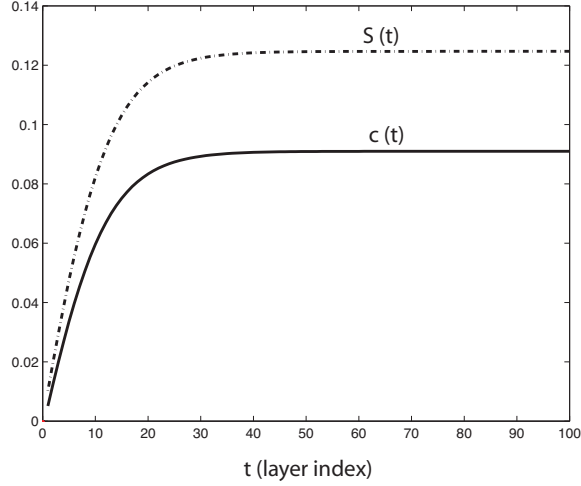
Figure 6.10: Evolution of layer step density $S(t)$ and GUC density $c(t)$ with film thickness.

total density of single steps being $2(1-S)S$, in Eq. 6.44 we have excluded two types of sites (upper terraces) among the four possible situations close to a single step. The factors $\frac{1}{4}$ in Eq. 6.45 and $\frac{1}{2}$ in Eq. 6.46 account for the exclusion of one undesired type of site among the four possible double-step sites (probability S^2), retaining only the valley and staircase configurations. Within the 1D reduced system, the formation enthalpy difference V is renormalized as follows:

$$\widetilde{V} = V + 2U[(1-S)^2 + \frac{1}{4}S^2] \tag{6.47}$$

The rate equation can now be constructed for the effective row-by-row growth: If the site belongs to a plateau (**a**), the nucleation of a GUC will incorporate two additional steps to the system. Conversely, if the site is already on the low displacement terrace of a single step (**b**), there will be no additional steps but just a shift of the existing one. If the site belongs to a valley (**c**), i.e. to low displacement terrace between two consecutive steps, the GUC nucleation will remove two steps from the system. Finally, if the site belongs to

137

a staircase configuration (**d**), the GUC nucleation will remove one step, but the remaining step will be double sized (elastic energy = 4U).

The local equilibrium condition (iv) is implemented by using the Boltzmann factors u and $\widetilde{v}$ corresponding to the energies U and $\widetilde{V}$, respectively :

$$u = \exp(-U/k_BT) \quad ; \quad \widetilde{v} = \exp(-\widetilde{V}/k_BT) \tag{6.48}$$

Therefore, with the correct normalization, the thermal probabilities for intergrowth nucleation at different sites are:

$$p_0 = \frac{\widetilde{v}u^2}{1 + \widetilde{v}u^2}, \quad p_1 = \frac{\widetilde{v}}{1 + \widetilde{v}}, \quad p_2 = \frac{\widetilde{v}}{\widetilde{v} + u^2}, \quad p_3 = p_0, \tag{6.49}$$

where the sub-indices 0, 1, 2 and 3 stand for plateau, single step, valley and staircase, respectively. Only events 0, 2 and 3 induce variations on S, while event 1 does not alter the number of steps. The balance in a given row yields the sought rate equation:

$$\frac{dS}{dt} = 2[p_0(1 - S)^2 - \frac{1}{4}(p_2 + p_3)S^2] \tag{6.50}$$

In Eq. 6.50, the "time" variable t has to be interpreted as an integer layer index. The expression for the general solution of the above differential equation reads as follows:

$$S = S_0 + S_1 \tanh[\nu(t - t_0)] \tag{6.51}$$

By differentiating Eq. 6.51, the parameters S_0, S_1 and ν can be found by comparison with Eq. 6.50:

$$S_0 = \frac{4u^2}{3u^2 - \frac{1+\widetilde{v}u^2}{\widetilde{v}+u^2}}; \quad S_1 = \pm\frac{2u\sqrt{u^2 + \frac{1+\widetilde{v}u^2}{\widetilde{v}+u^2}}}{3u^2 - \frac{1+\widetilde{v}u^2}{\widetilde{v}+u^2}}; \quad \nu = \mp\frac{\widetilde{v}u\sqrt{u^2 + \frac{1+\widetilde{v}u^2}{\widetilde{v}+u^2}}}{1 + \widetilde{v}u^2}.$$

$$(6.52)$$

The first layer grows on a step-free substrate. The parameter t_0 is then defined by this initial condition:

$$S(1) = 2p_0 \implies t_0 = 1 - \frac{1}{\nu}\tanh^{-1}[\frac{2p_0 - S_0}{S_1}] \qquad (6.53)$$

The concentration c of GUC within a given layer depends on the distribution of steps in the preceding layer:

$$c(t+1) = p_0(1 - S)^2 + \frac{1}{4}(p_2 + 2p_3)S^2 + p_1 S(1 - S) \qquad (6.54)$$

The existence of a steady-state regime follows directly from the Eq. 6.50:

$$\frac{dS}{dt} = 0 \iff S = \frac{2u\sqrt{\frac{\widetilde{v}+u^2}{1+2u^2\widetilde{v}+u^4}}}{1 + 2u\sqrt{\frac{\widetilde{v}+u^2}{1+2u^2\widetilde{v}+u^4}}} \equiv \overline{S}. \qquad (6.55)$$

Accordingly, by inserting $\overline{S}$ into Eq. 6.54 we obtain the asymptotical GUC concentration:

$$\overline{c} = 2p_0(1 - \overline{S})^2 + p_1\overline{S}(1 - \overline{S}) + \frac{1}{4}p_0\overline{S}^2. \qquad (6.56)$$

The extension of the transient is governed by the parameter ν through a characteristic length (number of layers) $\tau = \frac{1}{\nu}$. The lowest value τ can attain (rapid approach to the steady state) is $\tau_{min} = |\frac{1+v}{\sqrt{2}v}|$, and it corresponds to the extreme situation where the (elastic) energy per step is $U = 0$. In this

139

limit, the dynamics is only determined by the difference in the formation enthalpy V. In the other extreme, when $U \gg |V|$ (large step-energy), in the initial stage of the growth $\widetilde{V} \sim 2U$ and τ scales with $1/u^2 \gg 1$. In any case, for intermediate situations (say $\frac{U}{k_B T} \approx \frac{|V|}{k_B T} \sim 1$), τ will be of the order of a few tens of layers. The latter is illustrated in Fig. 6.10, where we plotted $S(t)$ and $c(t)$ according to Eq. 6.50-6.54.

6.4 Justification of the anisotropic NFEA

The NFEA is usually employed in normal emission ($k_{//} = 0$) and the band dispersion is mapped along the normal direction by changing the photon energy [33]. The dispersion of the photoelectron in the excited state is then well described by the free-electron parabola (FEP), provided for an adjustment of its effective mass and the inner potential. The use of a huge effective mass anisotropy within the free-electron approximation for the final state of the emitted electron could seem contradictory with the idea of a free-electron dispersion. In fact, considering a geometry far from normal emission (but still in the 1st in-plane BZ), the local photoelectron dispersion along $k_{//}$ is less well described by the bare free-electron parabola, since the band structure in the excited band contains the contribution of many parabolic branches [8] as illustrated in Fig. 6.11.

The k-axes in Fig. 6.11 are rescaled into dimensionless values in order to plot them in the same graph. The black parabola indicated in the graph represents the local parabolic fit in the 1st BZ in order to illustrate the anisotropy free electron approach. The idea of the anisotropic NFEA is that the ejected photoelectron reaches the final state at E_f by a direct transition with the addition of a reciprocal lattice vector G_z (along the normal) to its conserved local value in the initial band. Since the final state belongs also to the band structure of the periodic lattice, the local dispersion is better described by fitting the actual multi-folded dispersion in the repeated zone scheme, with an elliptic paraboloid. In Fig. 6.12 we draw the cuts with $E = E_f$ of the contributing paraboloid branches in the considered BZ. The leading surfaces (maximum energy) in the excited band define a sort of basket (see Fig. 6.13) that we can approximate locally with an elliptic paraboloid
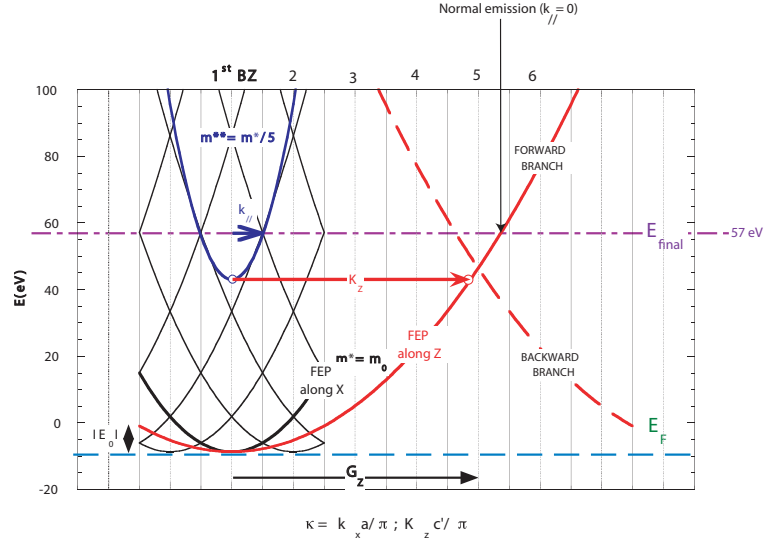
Figure 6.11: Schematic representation of the band structure of LSCO. The black parabolas correspond to the dispersion in k_x-direction, whereas the red ones indicate the dispersion in the k_z-direction.

centered in the considered BZ:

$$E_f = \frac{\hbar^2}{2m_c^*}[(G_\perp^2 + k_\perp^2) + \mu k_{//}^2] = \frac{\hbar^2}{2m_c^*}(K_\perp^2 + \mu k_{//}^2). \qquad (6.57)$$

The expression for the normal component k_z with the effective mass anisotropy becomes:

$$k_z = \sqrt{\frac{2m_c^*}{\hbar^2}(E_{PH} + |E_0| + E_b) - \mu k_{//}^2} - G_z. \qquad (6.58)$$

The reciprocal lattice vector G_z is defined as:

$$G_z \approx \sqrt{\frac{2m^*(E_{PH} + |E_0|)}{\hbar^2}}. \qquad (6.59)$$

E_{PH} is the photon energy, E_0 is the inner potential and E_b is the binding
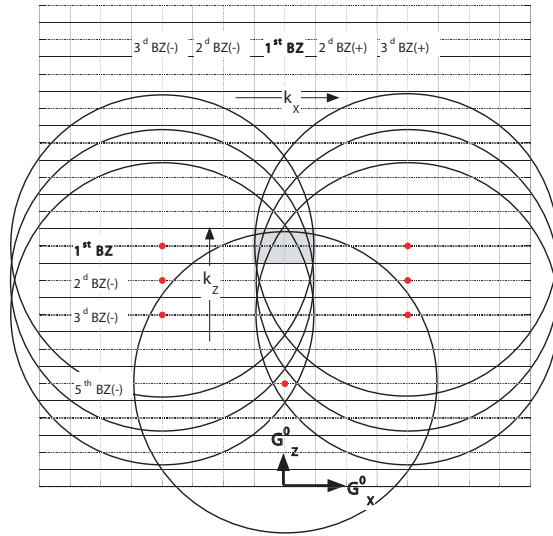
Figure 6.12: Representation in the $(k_x - k_z)$-plane of the contributing paraboloid branches in the considered BZ, indicated by a grey rectangle.

energy. The anisotropy factor μ has no special physical meaning for the free
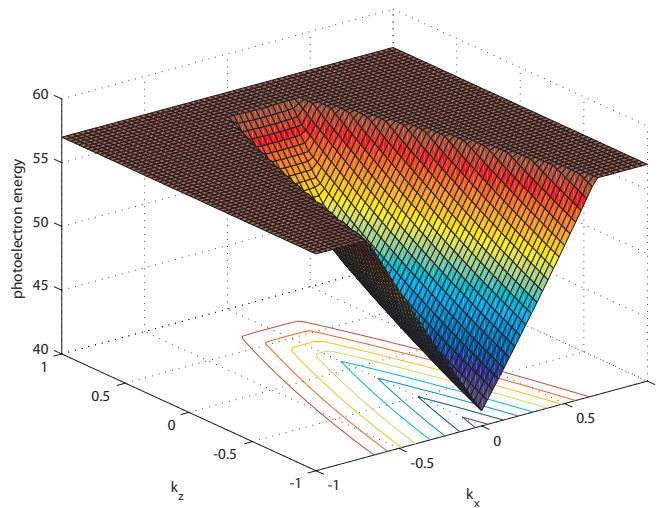
Figure 6.13: Local structure of the excited band close to the E_f.

electron in our context, it just describes the local band curvature along the

143

k_x-direction in the excited band. With this unusual curvature, the probing path in $E_b(k_{//})$ can be retrieved.

Bibliography

[1] M. Abrecht. *Photoemission studies of thin films grown by pulsed laser deposition; epitaxial strain effects on the electronic structure of high temperature superconductors.* PhD Thesis, 2003.

[2] M. Abrecht, D. Ariosa, D. Cloetta, S. Mitrovic, M. Oneillon, X. X. Xi, G. Margaritondo, and D. Pavuna. *Phys. Rev. Lett.*, (91):057002, 2003.

[3] S. M. Allemeh and K. H. Sandhage. *J. Am. Ceram. Soc.*, (78):2513, 1995.

[4] Y. Ando, S. Komiya, K. Segawa, S. Ono, and Y. Kurita. *Phys. Rev. Lett.*, (93):267001, 2004.

[5] D. Ariosa, C. Cancellieri, P. H. Lin, and D. Pavuna. *Phys. Rev. B*, (75):184505, 2007.

[6] D. Ariosa, C. Cancellieri, P.-H. Lin, and D. Pavuna. *Appl. Phys. Lett.*, (92):092506, 2008.

[7] D. Ariosa, V. N. Tsaneva, and Z. H. Barber. *IEEE Trans Appl. Supercond.*, (15):2993, 2005.

[8] N. W. Ashcroft and N. D. Mermin. *Solid State Physics.* Thomson Learning, Inc, 1976.

[9] J. Bardeen, L. N. Cooper, and J. R. Schrieffer. *Phys. Rev.*, (108):1175, 1957.

[10] W. Bauhofer, Hj. Mattausch, R. K. Kremer, P. Murugaraj, and A. Simon. *Phys. Rev. B*, (39):7244, 1989.

[11] J. G. Bednorz and K. A. Muller. *Z. Phys.*, (64):189, 1986.

[12] C. N. Berglund and W. E. Spicer. *Phys. Rev. A*, (136):1030 and 1040, 1964.

[13] P. V. Bogdanov, A. Lanzara, X. J. Zhou, S. A. Kellar, D. L. Feng, E. D. Lu, H. Eisaki, J. Shimoyama, K. Kishio, Z. Hussain, and Z.-X. Shen. *Phys. Rev. B*, (64):180505, 2001.

[14] S. V. Borisenko, M. S. Golden, S. Legner, T. Pichler, C. Dürr, M. Knupfer, and J. Fink. *Phys. Rev. Lett.*, (84):4453, 2000.

[15] C. Cancellieri, P.-H. Lin, D. Ariosa, and D. Pavuna. *J. of Phys. Condensed matter*, (19):246214, 2007.

[16] C. Cancellieri, P.-H. Lin, D. Ariosa, and D. Pavuna. *Phys. Rev. B*, (76):174520, 2007.

[17] J. Chang, S. Pailhs, M. Shi, M. Må nsson, T. Claesson, O. Tjernberg, J. Voigt, V. Perez, L. Patthey, N. Momono, M. Oda, M. Ido, A. Schnyder, C. Mudry, and J. Mesot. *Phys. Rev. B*, (75):224508, 2007.

[18] D.-X. Chen, A. Sanchez, T Puig, L. M. Martinez, and J. S. Muñoz. *Physica C*, (168):652, 1990.

[19] D. Cloetta. *Properties of $La_{2-x}Sr_xCuO_4$ under epitaxial strain: photoemission on ultra thin films grown by pulsed laser deposition.* PhD Thèse N. 3333, 2005.

[20] D. Cloetta, D. Ariosa, C. Cancellieri, M. Abrecht, S. Mitrovic, and D. Pavuna. *Phys. Rev. B*, (74):014519, 2006.

[21] M. Couach, A. F. Khoder, and F. Monnier. *Cryogenics*, (25):695, 1985.

[22] B. S. Daever and W. M. Fairbank. *Phys. Rev. Lett.*, (7):51, 1961.

[23] D. Dijkkamp, T. Venkatesan, X. D. Wu, S. A. Shaheen, N. Jisrawi, Y. H. Min-Lee, W. L. McLean, and M. Croft. *Appl. Phys. Lett.*, (51):619, 1987.

[24] B. Chrisey Douglas and Graham K. Hubler. *Pulsed Laser Deposition of Thin Films.* Wiley, 1994.

[25] H. Eisaki, N. Kaneko, D. L. Feng, A. Damascelli, P. K. Mang, K. M. Shen, Z.-X. Shen, and M. Greven. *Phys. Rev. B*, (69):064512, 2004.

[26] D. L. Feng, N. P. Armitage, D. H. Lu, A. Damascelli, J. P. Hu, P. Bogdanov, A. Lanzara, F. Ronning, Eisaki H. Shen, K. M., C. Kim, and Z.-X. Shen. *Phys. Rev. Lett.*, (86):5550, 2001.

[27] A. Gauzzi and P. Pavuna. *J. of Supercond.*, (9):23, 1995.

[28] A. Gauzzi and P. Pavuna. *Appl. Phys. Lett.*, (66):1836, 1995.

[29] F. Gömöri. *Superc. Sci. Technol.*, (10):523, 1997.

[30] J. Graf, G.-H. Gweon, K. McElroy, S. Y. Zhou, C. Jozwiak, E. Rotenberg, A. Bill, T. Sasagawa, H. Eisaki, Tagagi H. Uchida, S., D.-H. Lee, and A. Lanzara. *Phys. Rev. Lett.*, (98):067004, 2007.

[31] T. Haugan, P. N. Barnes, L. Brunke, I. Maartense, and J. Murphy. *Physica C*, (397):47, 2003.

[32] B. Hinnemann, H. Hinrichsen, and D. E. Wolf. *Phys. Rev. Lett.*, (87):135701–1, 2001.

[33] S. Hüfner. *Photoelectron Spectroscopy*. Springer, 2003.

[34] S. Hüfner. *Very high resolution Photoelectron Spectroscopy (Lecture Notes in Physics)*. Springer, 2007.

[35] S. Karimoto and M. Naito. *Jpn. J. Appl. Phys.*, (38):L283, 1999.

[36] Z. Z. Li, H. Raffy, S. Bals, G. van Tendeloo, and S. Megret. *Phys. Rev. B*, (71):1745032, 2005.

[37] C. Y. Lien, H. C. I. Kao, D. C. Ling, H. H. Lu, J. M. Chen, and J. M. Lee. *Chin. J. Phys.*, (43):629, 2005.

[38] J. P. Locquet, J. Perret, J. Fomperyrine, E. Mächler, J. W. Seo, and G. Van Tendeloo. *Nature*, (394):453, 1998.

[39] J. P. Locquet, J. Perret, J. W. Seo, and J. Fompeyrine. *Proc. SPIE Int. Soc. Opt. Eng.*, (3481):248, 1998.

[40] A. Macridin, M. Jarrel, T. Maier, and D. J. Scalapino. *Phys. Rev. Lett.*, (99):237001, 2007.

[41] A. Maeda, M. Hase, I. Tsukada, K. Noda, S. Takabayashi, and K. Uchinokura. *Phys. Rev. B*, (41):6418, 1990.

[42] A. Mans, I. Santoso, Y. Huang, W. K. Siu, S. Tavaddod, V. Arpiainen, M. Lindroos, H. Berger, V. N. Strocov, M. Shi, L. Patthey, and M. S. Golden. *Phys. Rev. Lett.*, (96):107007, 2006.

[43] I. Matsuda, T. Tanikawa, S. Hasegawa, H. W. Yeom, K. Tono, and T. Ohta. *e-J Surf. Sci. Nanotechnol.*, (2):169, 2004.

[44] W. Meevasana, X. J. Zhou, S. Sahrakorpi, W. S. Lee, W. L. Yang, K. Tanaka, N. Mannella, T. Yoshida, D. H. Lu, Y. L. Chen, R. H. He, Hsin Lin, S. Komiya, Y. Ando, F. Zhou, W. X. Ti, J. W. Xiong, Z. X. Zhao, T. Sasagawa, T. Kakeshita, K. Fujita, S. Uchida, H. Eisaki, A. Fujimori, Z. Hussain, R. S. Markiewicz, A. Bansil, N. Nagaosa, J. Zaanen, T. P. Devereaux, and Z.-X. Shen. *Phys. Rev. B*, (75):174506, 2007.

[45] F. Nakamura, T. Goko, J. Hori, Y. Uno, N. Nikugawa, and T. Fujita. *Phys. Rev. B*, (61):107, 2000.

[46] Ch. Niedermayer, C. Bernhard, T. Blasius, A. Golnik, A. Moodenbaugh, and J. I. Budnick. *Phys. Rev. Lett.*, (80):3843, 1998.

[47] D. Oezer. *Basic Model of Epitaxial Growth of $La_{2-x}Sr_xCuO_{4+\delta}$ Thin Films under Tensile Strain: Structure and Related Electronic Properties.* Master Thesis, 2008.

[48] S. H. Pan, E. W. Hudson, J. Ma, and J. C. Davis. *Appl. Phys. Lett.*, (73):58, 1998.

[49] A.-B. Posadas, M. Lippmaa, F. J. Walker, M. Dawber, C. H. Ahn, and J.-M. Triscone. *Topics in Applied Physics*, (105):219, 2007.

[50] H. Sato, A. Tsukada, M. Naito, and A. Matsuda. *Physica C*, (341-348):1767, 2000.

[51] J. M. Tarascon, W. R. McKinnon, P. Barboux, D. M. Hwang, B. G. Bagley, L. H. Greene, G. W. Hull, Y LePage, N. Stoffel, and M. Giroud. *Phys. Rev. B*, (38):8885, 1988.

[52] S. Timoshenko. *Théorie de l'Elasticité*. Librairie polytechnique Ch. Béranger, 1936.

[53] T. Timusk and B. Statt. *Rep. Prog. Phys.*, (62):61, 1999.

[54] C. C. Torardi, M. A. Subramanian, J. C. Calabrese, J. Gopalakrishnam, E. M. McCarron, K. J. Morrissey, T. R. Askew, R. B. Flippen, U. Chowdhry, and A. W. Sleight. *Phys. Rev. B*, (38):225, 1988.

[55] S. Tosto. *J. Phys. D: Appl. Phys.*, (36):1254, 2003.

[56] A. Trajnerowicz, A. Golnik, C. Bernhard, L. Machtoub, C. Ulrich, J. L. Tallon, and M. Cardona. *Phys. Rev. B*, (74):104513, 2006.

[57] C. C. Tsuei and J. R. Kirtley. *Rev. Mod. Phys.*, (72):969, 2000.

[58] T. Valla, T. E. Kidd, W.-G. Yin, G. D. Gu, P. D.1 Johnson, Z.-H. Pan, and A. V. Fedorov. *Phys. Rev. Lett.*, (98):167003, 2007.

[59] R. Anthony West. *Basic solid state chemistry*. Wiley, 1999.

[60] R. Wördenweber. *Supercond. Sci. Technol.*, (12):R86, 1999.

[61] B. P. Xie, K. Yang, D. W. Shen, J. F. Zhao, H.W. Ou, J. Wei, S.Y. Gu, M. Arita, S. Qiao, H. Namatame, M. Taniguchi, N. Kaneko, H. Eisaki, K. D. Tsuei, C. M. Cheng, I. Vobornik, J. Fujii, G. Rossi, Z. Q. Yang, and D. L. Feng. *Phys. Rev. Lett.*, (98):147001, 2007.

[62] J. Zaanen, G. A. Sawatzky, and J. W. Allen. *Phys. Rev. Lett.*, (55):418, 1985.

[63] G.-Q. Zheng, P. L. Kuhns, A. P. Reyes, B. Liang, and C. T. Lin. *Phys. Rev. Lett.*, (94):047006, 2005.

[64] W. Zhou. *J. of Superconductivity and Novel Magnetism*, (9):311, 1996.

Acknowledgments

I would like to thank my thesis advisor Davor Pavuna to have been always positive, helpful, funny, with me; he was always able to find a solution to any kind of problem (really any kind!).

I deeply thank Daniel Ariosa to have followed me step by step, without losing patience and always with a lot of funny humor.. I learnt a lot from him. I was really impressed by his polyhedric knowledge. I will miss a lot working with him. Thank you Daniel!

I am extremely grateful to Prof. Marco Grioni; his knowledge about ARPES is almost infinite....it was a real pleasure to work with him and his group.

I specially thank Henry Jotterand for his precious help at the beginning of my work in constructing the PLD system.

I enjoyed a lot to work at the SRC and I appreciated the support from all the staff especially from Hartmut Höchst.

Thank you to all my friends at EPFL, they all deserve to be mentioned: Guido, for all what he did for me, Johanna, who was always there for me, Joy, we worked a lot together and we had also great time as friends, and then Camilo, Vincent and Silvia, Aurore, Marco, Nick, German, Daniel (Gutierrez), Tony. All the workshop team at IPMC deserve also to be acknowledged in particular my friend Guglielmo (and his wife Vanessa) for his constant

help in solving my problems with the system. I also thank the secretaries of IPMC: Monique and Christine, always nice and helpful.

I thank David, for his help, his kindness, his support, his care, his infinite patience during my last period of the doctorate.

Grazie to my family (mamma e papà) and in particular to my sister Cinzia for their everyday support: even if I am far I am with you all the time.

Curriculum Vitae

CANCELLIERI CLAUDIA

EPFL-Swiss Federal Institute of Technology

Laboratoire de physique des rayons X

Institut de physique de la matiére complexe

(Bâtiment PH), Station 3, 1015 Lausanne, Switzerland

PHONE: +41 21 6935422   FAX: +41 21 6934666

EMAIL: claudia.cancellieri@epfl.ch

Personal information and address

Family name: Cancellieri

Name: Claudia

Date of birth: 20 December 1979

Place of Birth: Milan, Italy

Nationality: Italian

Education and professional experience

2004-2008 Doctoral Thesis in Physics at the Ecole Polytechnique Fédérale de Lausanne (EPFL), title: "The growth by laser ablation and electronic properties of thin cuprate films: $Bi_2Sr_{2-x}La_xCuO_6$ and $La_{2-x}Sr_xCuO_4$". Research on thin films of superconducting materials. Construction

and optimization of a new Pulsed Laser Deposition (PLD) system for thin films growing linked to a photoemission chamber for in-situ Angle Resolve Photoemission Spectroscopy (ARPES) electronic analysis. Study of structural, electronic and superconducting properties of $La_{2-x}Sr_2CuO_4$ thin films under epitaxial strain. Growth and analysis of La doped Bi-2201 thin films with different doping. Part of the photoemission analysis was performed at the Synchrotron Radiation Center in Madison, Wisconsin, U.S.A., in collaboration with the University of Wisconsin.

April 2003- February 2004 Diploma thesis work (Master Science) at the ENEA Research center in Frascati, Rome, Italy. Title of the thesis work: *Deposition and characterization of Ca doped $YBa_2Cu_3O_{7-\delta}$ epitaxial thin films.* The work focused on the effect of oxygen on the superconducting and structural properties of the films changed by the post annealing treatment. Laurea diploma obtained in February 2004 with a grade of 110/110 cum laude.

1998- February 2004 University degree in Physics at the "Università degli Studi di Milano", Milan, Italy, with a major in solid state physics and superconductivity.

Professional skills

Teaching experience Teaching assistant in basic physics course for chemistry students at EPFL. Laboratory supervision of 4th year undergraduate physics students. Supervision of final year students: Ludovic

Howald and Guy Dubuis (2006). Supervision of the Diploma work ("Travail de Master") of physics student, David Oezer, Feb. 15, 2008: "Basic Model of Epitaxial Growth of $La_{2-x}Sr_xCuO_{4+\delta}$ Thin Films under Tensile Strain: Structure and Related Electronic Properties".

Scientific Skills Research on high temperature superconducting thin films: Extensive experience in thin films heteroepitaxial growth by pulsed laser deposition and various characterization methods: X-ray diffraction, core levels and angle resolved photoemission spectroscopy (ARPES), AC-susceptibility, resistivity and transport measurements.

Language skills

Italian : mother tongue
English : fluent
French : fluent

Conferences and Schools

- 11-16 September 2006: MaNEP Summer school on *Probing the physics of low dimensional systems*, Saas Fee, Switzerland.

- 27-29 March 2006: International Symposium in Honor of J.G. Bednorz and K.A. Müller, *20 years after the discovery of High Tc superconductors*, Zurich, Switzerland.

- 26-28 September 2005: Workshop on Materials with novel electronic

properties, Les Diablerets, Switzerland. Poster presentation: *Growth and analysis of strained superconducting cuprates for in-situ photoemission studies.*

- 14-21 August 2005: PSI (Paul Scherrer Institute) Summer School, Zuoz, Switzerland. Poster presentation: *New Pulsed Laser Deposition system for in situ photoemission studies of High T_c superconducting thin films.*

- 3-8 October 2004: ASC Conference, Poster presentation: *Deposition and characterization of Ca doped $YBa_2Cu_3O_{7-\delta}$ epitaxial thin films.*

- 6-11 September 2004: MaNEP Summer School, Physics of Materials with Novel electronic properties, Saas-Fee, Switzerland.

- 6-10 January 2003: SCENET (European Superconducting Network) Winter School in Superconductivity, IRC in Superconductivity (Interdisciplinary Research Centre), Cambridge, UK.

Publications

- **C. Cancellieri**, A. Augieri, V. Boffa, G. Celentano, L. Ciontea, F. Fabbri, V. Galluzzi, U. Gambardella, G. Grassano, T. Petrisor, R. Tebano, *Deposition and characterization of $Y_{1-x}Ca_xBa_2Cu_3O_{7-\delta}$ epitaxial thin films*, IEEE Transactions on Applied Superconductivity **15**, Issue 2, Part 3 (2005), 3038.

- D. Cloetta, D. Ariosa, M. Abrecht, **C. Cancellieri**, S. Mitrovic, M. Papagno, D. Pavuna, *Systematic Studies of $La_{2-x}Sr_xCuO_4$ in Direct*

Synchrotron Light: On the role of Compressive against Tensile Strain, Proc. SPIE Int. Soc. Opt. Eng. **5932**, 10 (2005).

- D. Cloetta, D. Ariosa, **C. Cancellieri**, M. Abrecht, S. Mitrovic, D. Pavuna, *Three-dimensional dispersion induced by extreme tensile strain in $La_{2-x}Sr_xCuO_4$ films*, Phys. Rev. B **74**, 014519 (2006).

- D. Ariosa, **C. Cancellieri**, P.-H. Lin, D. Pavuna, *Self-ordering of random intercalates in thin films of cuprates superconductors: Growth model and x-ray diffraction diagnosis.* Phys. Rev. B **75**, 184505 (2007).

- **C. Cancellieri**, P.-H. Lin, D. Ariosa, D. Pavuna, *Dopant rearrangement and superconductivity in $Bi_2Sr_{2-x}La_xCuO_6$ thin films under annealing*, J. of Physics Condensed matter **19** 246214 (2007).

- **C. Cancellieri**, P.-H. Lin, D. Ariosa, D. Pavuna, *Embedded polytypes in $Bi_2Sr_{2-x}La_xCuO_6$ thin films grown by laser ablation*, Phys. Rev. B **76**, 174520 (2007).

- D. Ariosa, **C. Cancellieri**, P.-H. Lin, D. Pavuna, *Fermi surface determination from wavevector quantization in LaSrCuO films*, Appl. Phys. Lett. **92**, 092506 (2008).

Two more publications pending.